



**SYNTHESIS AND DEVELOPMENT OF REFRACTORY HIGH ENTROPY
ALLOYS**

AYBERK AYRENK

SEPTEMBER 2020

SYNTHESIS AND DEVELOPMENT OF REFRACTORY HIGH ENTROPY
ALLOYS

A THESIS SUBMITTED TO
THE GRADUATE SCHOOL OF NATURAL AND APPLIED
SCIENCES OF
ÇANKAYA UNIVERSITY

BY
AYBERK AYRENK


IN PARTIAL FULFILLMENT OF THE REQUIREMENTS FOR THE
DEGREE OF
MASTER OF SCIENCE
IN
MICRO AND NANOTECHNOLOGY

SEPTEMBER 2020

STATEMENT OF NON-PLAGIARISM PAGE

I hereby declare that all information in this document has been obtained and presented in accordance with academic rules and ethical conduct. I also declare that, as required by these rules and conduct, I have fully cited and referenced all material and results that are not original to this work.

Name, Last Name: Ayberk Ayrenk

Signature: 

Date: 04.10.2020

ABSTRACT

SYNTHESIS AND DEVELOPMENT OF REFRACTORY HIGH ENTROPY ALLOYS

AYRENK, Ayberk
M.Sc., Micro and Nanotechnology
Supervisor: Assist. Prof. Dr. İlkey Kalay

SEPTEMBER 2020, 85 pages

High entropy alloys (HEAs) serve as a new metallic alloy system for high-temperature applications in aerospace, nuclear, and chemical process industries due to their attractive properties. This thesis focuses on the synthesis and development of refractory HEAs, and the investigation of their phase stability, the evolution of microstructure, high-temperature behavior, mechanical properties of nonequiatomic Al-Co-Cr-Fe-(Ni-Nb-Ti), and equiatomic Al-Hf-Mo-Nb-Ta-Ti-V alloy systems under as-cast and isothermally annealed conditions. The alloys were predetermined based on the calculated thermodynamic data. The alloys were then produced by vacuum arc melter using high purity elements. The high entropy alloy systems were investigated using X-ray diffraction (XRD), in-situ X-ray diffraction (XRD), optic microscope (OM), scanning electron microscope (SEM), hardness, compression, and tension tests.

The analysis reveals the dependency of mechanical properties and phase formation on Nb and Ti concentration of the Al-Co-Cr-Fe-(Ni-Nb-Ti) alloy systems. The Vickers microhardness tests reveal an increase in hardness with the addition of Nb and Ti. The ductile type of fracture was seen for as-cast $\text{Al}_8\text{Co}_{30}\text{Cr}_{18}\text{Fe}_9\text{Ni}_{31}\text{Nb}_4$ and

$\text{Al}_8\text{Co}_{30}\text{Cr}_{18}\text{Fe}_9\text{Ni}_{31}\text{Ti}_4$ alloys. The highest toughness value, highest ultimate tensile strength of 844 MPa and highest compressive fracture strain of 29.76% were observed for $\text{Al}_8\text{Co}_{30}\text{Cr}_{18}\text{Fe}_9\text{Ni}_{31}\text{Ti}_4$ alloy, which has tetraenaite FeNi intermetallic phase distributed in the dendritic matrix.

The Al-Hf-Mo-Nb-Ta-Ti-V alloy systems with B2/BCC dual-phase structure indicate good phase stability upon heating. The structure analysis reveals that these systems can be good candidates for refractory HEAs for high-temperature applications.

Keywords: High Entropy Alloy, Refractory, Heat Treatment, Mechanical Properties.



ÖZ

REFRAKTER YÜKSEK ENTROPİLİ ALAŞIMLARIN SENTEZİ VE GELİŞTİRİLMESİ

AYRENK, Ayberk
Yüksek Lisans, Mikro ve Nanoteknoloji
Tez Yöneticisi: Dr. Öğr. Üyesi İlkay Kalay

EYLÜL 2020, 85 sayfa

Yüksek entropili alaşımlar (YEA'lar), uzay ve havacılık, nükleer ve kimyasal proses endüstrilerinde yüksek sıcaklıklı uygulamalarda, ilgi çeken özelliklerinden ötürü yeni metalik alaşım sistemleri olarak görev görmektedir. Bu tez, refrakter yüksek entropili alaşımların sentezi ve geliştirilmesine, eşatomik olmayan Al-Co-Cr-Fe-(Ni-Nb-Ti) ve eşatomik Al-Hf-Mo-Nb-Ta-Ti-V alaşım sistemlerinin döküm ve izotermal tavlama koşulları altındaki faz kararlılıkları, mikroyapı değişimleri, yüksek sıcaklıklardaki davranışları ve mekanik özelliklerinin incelenmesine odaklanmaktadır. Alaşımlar önceden hesaplanan termodinamik verilere göre belirlendi. Alaşımlar yüksek saflıkta elementler kullanılarak vakumlu ark eritici ile üretildi. Yüksek entropili alaşım sistemleri X-ışını kırınımı (XRD), yerinde X-ışını kırınımı, optik mikroskop, geçişli electron mikroskobu, sertlik, basma ve çekme testleri ile incelenmiştir.

Analizler, Al-Co-Cr-Fe-(Ni-Nb-Ti) alaşım sistemlerinde Nb ve Ti elementleri konstanrasyonlarına bağlı faz oluşumlarını ve mekanik özellik değişimlerini ortaya koymuştur. Vickers mikrosertlik testleri, Nb ve Ti eklemesiyle alaşımların sertliklerinde artış göstermektedir. Basma testlerinde döküm $Al_8Co_{30}Cr_{18}Fe_9Ni_{31}Nb_4$ ve $Al_8Co_{30}Cr_{18}Fe_9Ni_{31}Ti_4$ alaşımları sünek tipi kırılma tipi göstermiştir. Çekme

testlerinde en yüksek tokluk deęeri, dendrit matrisinde tetraenite FeNi fazının daęılım gösterdięi döküm $Al_8Co_{30}Cr_{18}Fe_9Ni_{31}Ti_4$ alařımı için, 844 MPa ile en yüksek çekme mukavemeti ve %29.76 ile en yüksek basınç kırılma gerilimi ile gözlemlenmiřtir.

B2/BCC çoklu fazına sahip Al-Hf-Mo-Nb-Ta-Ti-V alařım sistemleri yüksek sıcaklıklarda kararlı bir faz yapısı ortaya koymuřtur. Mikroyapı analizleri göstermektedir ki bu alařımlar yüksek sıcaklıklı uygulamalar için iyi refrakter YEA adaylarıdır.

Anahtar kelimeler: Yüksek Entropili Alařım, Refrakter, Isıl İşlem, Mekanik Özellikler.





To My Precious Family

ACKNOWLEDGMENTS

Firstly, I would sincerely like to thank my supervisor Assist. Prof. Dr. İlkey Kalay for her guidance, encouragement, support, and patience throughout my undergraduate and graduate study. I am heartily grateful for all of her valuable contributions to this study with endless tolerance.

I warmly thank Dr. Gökhan Polat. I am much obliged to him for helping me, and being patient with me during the thesis study. His excellent working discipline, undefinable efforts, immense knowledge, and great advice helped me with everything in this thesis.

I want to express my heartfelt thanks to Dr. Ezgi Bütev Öcal during this process. Beyond her valuable teachings and suggestions, her friendly motivations and supports helped me to keep on track and continue to work even though in the times when I thought I could not finish my thesis. I am very thankful and indebted to her.

I would like to thank my previous and current laboratory mates Ertuğrul Büyükhergül and Hüseyin Basri Çerçi for their great assists and suggestions during the period of study.

I especially thank Arda Öcal, Halil İbrahim Andiç, and Kadir Can Erkmek for their great friendships as the lecturers. I am very grateful for their positive attitude, support, and advice during the thesis period.

Last but not least, I owe my deepest gratitude to my beloved family, Ayfer, Birol, and Koray Ayrenk. I will always be grateful and indebted for their encouragement, endless supports, greatest motivations, and unconditional love and respect throughout my entire life. My sincere thanks go to my mother and father to endure and be patient against my angry and aggressive behaviors during the whole thesis process. I am so glad to have them.

TABLE OF CONTENTS

STATEMENT OF NON-PLAGIARISM PAGE	iii
ABSTRACT	iv
ÖZ	vi
ACKNOWLEDGMENTS	ix
1. INTRODUCTION	1
1.1. High Entropy Alloys	1
1.2. Origin of High Entropy Alloys.....	2
1.3. Literature Review of High Entropy Alloys	3
1.4. Basic Concept of High Entropy Alloys.....	4
1.5. Four Core Effects	5
1.5.1. High Entropy Effect	6
1.5.2. Severe Lattice Distortion.....	7
1.5.3. Sluggish Diffusion Effect.....	9
1.5.4. The Cocktail Effect	10
1.6. Phase Formation in High Entropy Alloys	10
1.6.1. Parametric Approaches in Phase Selection	10
1.6.2. Phase Formation in High Entropy Alloys	14
1.6.2.1. Solid Solution Phases.....	15
1.6.2.1.1. Phase Formation in Equiatomic High Entropy Alloys	15
1.6.2.1.1.1. BCC Phase Formation	15
1.6.2.1.1.2. FCC Phase Formation.....	16
1.6.2.1.1.3. Multiphase FCC+BCC Structure.....	18
1.6.2.1.2. Solid Solution Formation in Nonequiatomic HEAs.....	21
1.6.2.1.2.1. The Effect of Al on HEAs	22
1.6.2.1.2.2. Effect of Transition Metals.....	24
1.6.2.2. Intermetallic Phases	27
1.6.2.2.1. Laves Phase.....	27

1.6.2.2.2. Sigma Phase (σ)	28
1.6.2.2.3. B2 Phase.....	28
1.6.2.2.4. L1 ₂ Phase.....	28
1.7. Refractory High Entropy Alloys	29
1.7.1. Mechanical Properties of Refractory High Entropy Alloys.....	29
1.7.2. Oxidation Behavior of Refractory High Entropy Alloys	31
1.7.3. Application Areas of Refractory High Entropy Alloys.....	33
1.8. Thesis Organization.....	34
2. EXPERIMENTAL PROCEDURE.....	35
2.1. Alloy Production	35
2.2. Heat Treatment of Alloys.....	36
2.3. Characterization.....	37
2.3.1. X-Ray Diffraction Analysis	37
2.3.2. Optical and Scanning Electron Microscopy (SEM) Analysis.....	38
2.4. Mechanical Tests.....	39
3. RESULTS AND DISCUSSION	42
3.1. Thermodynamic Calculations of High Entropy Alloys.....	42
3.2. Characterization of As-Cast High Entropy Alloys.....	43
3.2.1. X-Ray Diffraction Analysis	43
3.2.2. Microstructure Analysis	46
3.3. Characterization of Isothermally Heat-Treated High Entropy Alloys	49
3.3.1. RA01 (Al ₈ Co ₃₀ Cr ₁₈ Fe ₉ Ni ₃₁ Nb ₄) Alloy	49
3.3.2. RA08 (Al ₈ Co ₃₀ Cr ₁₈ Fe ₉ Ni ₂₅ Nb ₅ Ti ₅) Alloy	51
3.3.3. RA10 (AlCoCrFeNiNbTi) Alloy	53
3.3.4. RA14 (Al ₈ Co ₃₀ Cr ₁₈ Fe ₉ Ni ₃₁ Ti ₄) Alloy	55
3.4. Characterization of Mechanical Properties of High Entropy Alloys.....	57
3.4.1. Hardness Measurements.....	57
3.4.2. Compression Tests	59
3.4.3. Tensile Test Results of RA01 and RA14 High Entropy Alloys.....	63
3.5. Characterization of High Entropy Alloys for High-Temperature Applications..	65
3.5.1. In situ XRD Analysis of Refractory High Entropy Alloys	67
3.5.2. Microstructure Analysis of RA20 and RA23 High Entropy Alloys	70

3.5.3. Hardness Measurements of Alloys.....	72
4. CONCLUSIONS AND FUTURE PREDICTIONS	73
4.1. Conclusions	73
4.2. Future Recommendations.....	74
REFERENCES.....	76



LIST OF FIGURES

Figure 1. 1. The schematic density distribution of equiatomic and non-equiatomic HEAs studies compared to traditional alloys [4].	2
Figure 1. 2. The schematic plot of ΔS_{mix} for a ternary alloy system. Red region, which is limited with 8.4 and up to 9.15 J/mol.K represents high entropy, while blue regions are indicating conventional alloys [12].	5
Figure 1. 3. Two-dimensional schematic image of dislocation movements in the whole solute matrix of a high entropy alloy with five principle elements. Figure shows the change in solid solution from (a) dilute to (b) complex and concentrated structure by overcoming the periodic Peierls-Nabarro energy barrier field [27].	8
Figure 1. 4. (a) BCC and (b) FCC crystal structures of a HEA composed of 5 elements [28].	8
Figure 1. 5. Normalized activation energy values of Cr, Mn, Fe, Co, Ni in different alloy matrices [30].	9
Figure 1. 6. X-Ray Diffraction occurred by atomic scattering [44].	14
Figure 1. 7. Engineering stress and strain graph for CoCrFeMnNi at different temperatures [11].	18
Figure 1. 8. XRD patterns of equiatomic AlCoCrFeNi HEA and nonequiatomic $\text{Al}_x\text{CoCrFeNi}$ HEA powders after 20h ball milling process [51].	19
Figure 1. 9. XRD patterns of ball milled (a) AlCoFeNi, (b) AlCoFeNiMo, (c) AlCoFeNiTi, (d) AlCoFeNiMoTi HEAs at different times [40].	20
Figure 1. 10. XRD patterns of sintered HEAs at different temperatures [40].	20
Figure 1. 11. Microhardness results of HEAs at different processing [40].	21
Figure 1. 12. XRD patterns of as-cast Al-Co-Cr-Cu-Fe-Ni based HEAs [49].	22
Figure 1. 13. XRD patterns of $\text{Al}_x\text{FeCoNiCrMn}$ based HEA with different concentrations of Al element [16].	23
Figure 1. 14. (a) Engineering stress-strain curve, (b) tensile strength, yield strength, and elongation, and (c) Vickers hardness values of as-cast $\text{Al}_x\text{FeCoNiCrMn}$	

concerning different Al concentrations [16]. The hardness graph of HEAs are separated as region I (single FCC alloys with $x < 8$), region II (mixed FCC+BCC phase alloys with $8 \leq x < 16$), and region III (available FCC alloys with $x > 16$)..... 24

Figure 1. 15. XRD patterns of $(\text{AlCoCrFeNi})_{100-x}\text{Co}_x$ HEAs ($x=0, 4, 8, 12, 16$) [52]. 25

Figure 1. 16. XRD patterns of $(\text{CrMnFeCo})_{1-x}\text{Ni}_x$ HEA with increasing Ni content [50]. 26

Figure 1. 17. (a) XRD patterns of Fe_xCoNiCu HEAs and their (b) FCC and BCC peak positions with degrees between 42° and 46° angles [54]. 26

Figure 1. 18. Compressive engineering stress-strain curves of (a) $\text{Nb}_{25}\text{Mo}_{25}\text{Ta}_{25}\text{W}_{25}$ and (b) $\text{V}_{20}\text{Nb}_{20}\text{Mo}_{20}\text{Ta}_{20}\text{W}_{20}$ alloys at elevated temperatures [68]..... 30

Figure 1. 19. The temperature dependence of yield strength of $\text{Nb}_{25}\text{Mo}_{25}\text{Ta}_{25}\text{W}_{25}$ and $\text{V}_{20}\text{Nb}_{20}\text{Mo}_{20}\text{Ta}_{20}\text{W}_{20}$ RHEAs and two superalloys; Inconel 718 and Haynes 230 [68]. 31

Figure 1. 20. (a) XRD patterns of RHEAs oxidized at 1273 K for 10h and (b) isothermal oxidation curves RHEAs at 1273 K [72]. 32

Figure 1. 21. Cut section of a gas turbine engine [74]. 33

Figure 2. 1. (a) Edmund Bühler MAM 1 vacuum-arc-melting device, (b) copper plate, and (c) copper mold used for vacuum suction casting 36

Figure 2. 2. (a) Protherm PLF Series Chamber Furnace and (b) inside the furnace. 37

Figure 2. 3. (a) D8 Advance Bruker X-ray Diffractometer, and (b) X-ray tube, detector, and specimen holders. 38

Figure 2. 4. SPEX SamplePrep 8000M Mixer/Mill ball milling device. 38

Figure 2. 5. (a) Nikon Eclipse LV150N optic microscope, and (b) FEI Nova NanoSEM 430 scanning electron microscope. 39

Figure 2. 6. INNOVATEST Nexus 7500TM Universal hardness tester..... 40

Figure 2. 7. Buehler IsoMet 5000 Linear Precision Saw device..... 41

Figure 2. 8. (a) Instron 5582 mechanical testing machine with (b) compression apparatus holding 3 mm specimen, and (c) tensile apparatus holding 4 mm specimen. 41

Figure 3. 1. XRD patterns of as-cast HEAs. 45

Figure 3. 2. SEM images of as-cast (a) RA01 (1000x), (b) RA01 (2000x), (c) RA02 (1000x), (d) RA02 (2000x), (e) RA08 (1000x), (f) RA08 (2000x), (g) RA10 (1000x), (h) RA10 (2000x), (i) RA14 (1000x), and (j) RA14 (2000x)	47
Figure 3. 3. EDS maps according to elemental distributions of (a) RA01, (b) RA02, (c) RA08, (d) RA14 HEAs.....	49
Figure 3. 4. XRD patterns of as-cast RA01 alloy, isothermally annealed RA01 alloy at 1073 K for 24 hours and isothermally annealed RA01 alloy at 1273 K for 24 hours.	50
Figure 3. 5. OM images of (a, b) as-cast RA01 alloy, (c, d) isothermally annealed RA01 alloy at 1073 K for 24 hours, and (e, f) isothermally annealed RA01 alloy at 1273 K for 24 hours at different magnifications.....	51
Figure 3. 6. XRD patterns for RA08 HEA isothermally annealed at 1073 K (800 °C) and 1273 K (1000 °C) for 24 hours.....	52
Figure 3. 7. OM images of (a, b) as-cast RA08 alloy, (c, d) isothermally annealed RA08 alloy at 1073 K for 24 hours, and (e, f) isothermally annealed RA08 alloy at 1273 K for 24 hours at different magnifications.....	53
Figure 3. 8. XRD patterns for RA10 HEA isothermally annealed at 1073 K (800 °C) and 1273 K (1000 °C) for 24 hours.....	54
Figure 3. 9. OM images of (a, b) as-cast RA10 alloy, (c, d) isothermally annealed RA10 alloy at 1073 K for 24 hours, and (e, f) isothermally annealed RA10 alloy at 1273 K for 24 hours at different magnifications.....	55
Figure 3. 10. XRD patterns of as-cast RA14 alloy, isothermally annealed RA14 alloy at 1073 K (800 °C) and 1273 K (1000 °C) for 24 hours.....	56
Figure 3. 11. OM images of (a, b) as-cast RA14 alloy, (c, d) isothermally annealed RA14 alloy at 1073 K for 24 hours, and (e, f) isothermally annealed RA14 alloy at 1273 K for 24 hours at different magnifications.....	57
Figure 3. 12. Vickers hardness graph presenting hardness values with their standard deviations of both as-cast and heat-treated alloys at 1073 K and 1273 K.	59
Figure 3. 13. The 3 mm diameter and 5 mm length compression test specimens of RA01, RA08, and RA14 alloys, which were prepared due to standards (top) and the barreled and fragmented specimens after compression tests (below).....	60
Figure 3. 14. Compressive stress-strain curves of RA01, RA08, and RA14 HEAs.	61

Figure 3. 15. SEM micrographs of the fractured surface of RA08 alloy after compression test.....	62
Figure 3. 16. Tensile test results of (a) RA01 and RA14 HEAs, and (b) Aluminum 3105 alloy.....	63
Figure 3. 17. SEM images of fractured surfaces of (a, b) RA01 and (c, d) RA14 alloys after tensile test.	65
Figure 3. 18. In situ XRD patterns of RA20 alloy.	68
Figure 3. 19. XRD pattern of RA20 alloy after quenching to room temperature.	68
Figure 3. 20. In situ XRD pattern of RA23 alloy.....	69
Figure 3. 21. XRD pattern of RA23 alloy after quenching to room temperature.	70
Figure 3. 22. Optical microscopy images of as-cast (a – b) RA20 and (c – d) RA23 alloys.	71
Figure 3. 23. Vickers hardness graph presenting hardness values of as-cast RA20 and RA23 with their standard deviations.....	72

LIST OF TABLES

Table 1. 1. ΔH_{mix} and ΔS_{mix} of elemental, compound, intermetallic, and solid solution phases for n-element HEAs.....	7
Table 1. 2. Atomic radii and electronegativity values of elements in AlCoCrFeNi HEA.	16
Table 1. 3. The atomic radii and electronegativity values of constituent elements of CoCrFeMnNi HEA.	17
Table 1. 4. Thermodynamic data of Ti-Zr-Ni based HEAs [56].	27
Table 1. 5. Yield strength values of RHEAs at different heat treatment conditions [71]	31
Table 2. 1. Nominal compositions Al-Co-Cr-Fe-Ni (Nb-Ti) based alloys.....	35
Table 2. 2. Nominal compositions of Al-Hf-Mo-Nb-Ta-Ti (V) based alloys.	35
Table 3. 1. Thermodynamical data of alloys.	43
Table 3. 2. Atomic radii of constituent elements of the alloys.....	43
Table 3. 3. ΔH_{mix} values of elements in $\text{kJ}\cdot\text{mol}^{-1}$ [77].	45
Table 3. 4. EDS analysis of alloys in at.%.	48
Table 3. 5. EDS analysis of dendritic (D) and interdendritic (ID) regions of alloys in at.%.	48
Table 3. 6. Compressive properties of RA01, RA08, RA14 HEAs.	61
Table 3. 7. Comparison of compressive properties of HEAs with CoCrFeNi-based alloys.	63
Table 3. 8. Values yield strength (σ_y), ultimate tensile strength (σ_{UTS}), and strain values at break (ϵ_{comp}) for RA01 and RA14 HEAs.	64
Table 3. 9. Crystal structures, densities (ρ), and melting points (T_m) of RA20, RA23 alloys, and other alloy systems published in recent years.....	66
Table 3. 10. Thermodynamical parameters of RA20 and RA23 alloys.	67
Table 3. 11. Atomic radius values in nm of each element in RHEAs.	67
Table 3. 12. ΔH_{mix} values of constituent elements of RA20 and RA23 alloys [76]. ..	70

Table 3. 13. Overall, dendritic (D), and interdendritic (ID) EDS results of RHEAs in at.%. 72



LIST OF ABBREVIATIONS

HEA	High Entropy Alloy
MPEA	Multi-principal Element Alloy
RHEA	Refractory High Entropy Alloy
FCC	Face Centered Cubic
BCC	Body Centered Cubic
HCP	Hexagonal Close Packed
HV	Hardness Vickers
MPa	Mega Pascal
GPa	Giga Pascal
XRD	X-ray Diffraction
OM	Optical Microscopy
SEM	Scanning Electron Microscopy
HT	Heat Treatment

CHAPTER I

INTRODUCTION

1.1. High Entropy Alloys

Since the first alloying process was accidentally found with copper and arsenic discovery in the Bronze Age [1-2], new requirements in industrial areas result in many discoveries and developments in materials science upon history. Due to the increasing demand, especially in aerospace and defense industries, much effort has been given to develop new metallic alloys with better mechanical, thermal, and chemical properties. Regarding their remarkable and unique properties such as high strength and hardness, excellent corrosion and oxidation resistance, superior high-temperature mechanical properties, magnetic properties, and impressive thermal stability, HEAs have attracted much attention. Since their discovery, much effort has been given to understand the concept of HEAs, and numerous types of HEA systems were discovered with impressive properties. HEAs serve as new metallic alloy systems for high-temperature applications in aerospace, nuclear, and chemical process industries due to their attractive properties. Multiphase, refractory, lightweight, amorphous, intermetallic contained, and magnetic HEAs are the examples of these types.

As a new generation multi-principal alloy system, HEAs are random solid solutions consist of five or more principal elements with variable compositions between 5 or 35 atomic percentages. According to Yeh et al. [3], HEAs are defined as equiatomic multi-component alloy systems composed of 5 or more principal metallic elements. Furthermore, Pradeep et al. [3-4] reported the exceptional phase stability and tensile properties of nonequiatomic single-phase $\text{Fe}_{40}\text{Mn}_{27}\text{Ni}_{26}\text{Co}_5\text{Cr}_2$ and $\text{Fe}_{37}\text{Mn}_{45}\text{Co}_9\text{Cr}_9$ HEAs. This study expanded the definition of HEAs and now it is known that HEAs may have equiatomic, nearly-equiatomic, or nonequiatomic proportions. HEAs may have the constituent elements with nonequiatomic compositions between 5 or 35 at.% and may have minor elements besides the principal ones to enhance the mechanical, thermal, and chemical properties [2, 5-8]. The schematic density distribution of

equiatomic and non-equiatomc HEA studies compared to traditional alloys is shown in Figure 1.1. The increase in the number of nonequiatomc HEAs studies compared to the equiatomic HEAs and conventional alloys is significant.

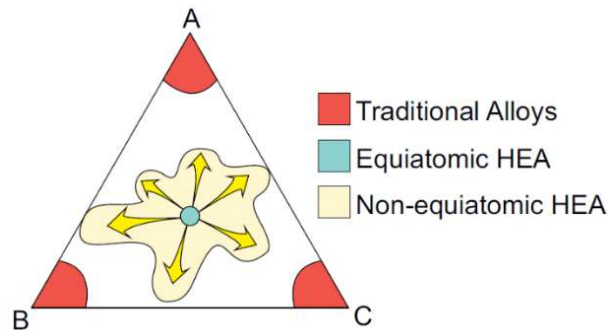


Figure 1. 1. The schematic density distribution of equiatomic and non-equiatomc HEAs studies compared to traditional alloys [4].

1.2. Origin of High Entropy Alloys

The high entropy alloy term was initially proposed by Cantor, 1979, and Yeh, 1996. However, their reports on HEAs gained interest in 2004 [2]. Cantor reported the equiatomic MPEAs consisting of 20 different components with 5 atomic percent (at.%). Among these alloys, $\text{Fe}_{20}\text{Co}_{20}\text{Cr}_{20}\text{Mn}_{20}\text{Ni}_{20}$ (in at.%) showed a single primary FCC phase formation. The formation of a single FCC phase means that all these elements in the system are mixed into one solution [2], [9]. Since they first define this system, Cantor's group studied on this system widely. The first paper was entitled "Microstructural development in equiatomic multi-component alloys" was published in 2004 by Cantor et al. [2, 6, 9-10]. Jien-Wei Yeh's started working on MPEAs in 1995. He believed that high mixing entropy might have an effect on the reduction of phase number [6]. By this manner, Yeh and his student K. H. Huang prepared 40 equiatomic as-cast and fully annealed alloys, including five to nine components for investigation and analysis of HEAs in 1996. The study showed that the higher number of constituent elements in the alloys results in the higher hardness of the alloy. However, they observed a small decrease in hardness at nine-component alloys. Also, they thought that additive elements and low free energy due to high mixing entropy have an excellent effect on corrosion resistance according to their study. Yeh published his first two papers on HEAs. His paper entitled "Nanostructured high entropy alloys with multi-principal elements - novel alloy design concepts and outcomes" [7] became

a milestone for developments of next generation high entropy materials with exclusive mechanical and thermal properties [2], [6]. Since their first reported by Cantor and Yeh, many research and developments on high entropy alloys have attracted much attention.

1.3. Literature Review of High Entropy Alloys

Since their discovery by Cantor and et al. [9] and Yeh and et al. [10], much effort has been given to understand and develop these new alloy systems with enhanced mechanical, physical, and chemical properties. Cantor et al. [9] reported FeCrMnNiCo alloy, known as “Cantor alloy”, the first multi-component alloy consisting of five transition elements. Gludovatz et al. [11] showed that Cantor alloy with single FCC structure has a superior tensile strength of 1280 MPa and yield strength of 759 MPa, when the temperature decreases from room temperature (298 K) to cryogenic temperature (77 K). HEAs are mainly composed of metallic transition elements, such as Co, Cr, Cu, Fe, Mn, and Ni elements. These elements have similar atomic sizes, electronegativities, and electron valencies with each other [12-13]. Al is a widely used metallic element, as well due to its functional behavior on oxidation and wear resistance. The addition of Al to the HEA systems increases the possibility of BCC phase formation, thus results in the enhancement of the hardness of the alloy [14-18]. Considerable studies based on ‘Cantor alloy’ showed that the addition of some refractory elements and/or Al significantly affects the phase formation, microstructure, and mechanical and thermal properties of HEA systems. The refractory elements from transition groups in the periodic table such as Mo, Nb, Ti, Ta, W, V, Hf, Zr, and even Cr, are mainly used in addition to Al to modify HEAs to improve mechanical properties and oxidation and wear behavior at extremely high temperatures [19]. Senkov et al. [20] developed the refractory high entropy alloys, RHEAs, with promising excessive high-temperature properties for high-temperature applications.

HEAs may have equiatomic, nearly-equiatomic, or nonequiatomic proportions. The non-equiatomic systems attracted much attention with their remarkable mechanical properties. It was reported that, Fe and Nb are the potential stabilizers of the primary brittle intermetallic C14-Laves phase with hexagonal crystal structure [2], [21]. nonequiatomic Al-Co-Cr-Fe-Nb-Ni HEA systems [22-23]. Furthermore, Nb is an excellent promoter for the intermetallic Ni₃Al phase and responsible for precipitate

formation in Al-Co-Cr-Fe-Nb-Ni HEA, while Co and Fe being destabilizers for Ni₃Al. It was reported that the increase in Nb concentration results in the increase in size and volume fractions of precipitates, and thus the increase in the hardness of HEA. On the other hand, lowering the Fe content destabilizes the Laves phase and decreases the hardness of the alloy due to the tendency of Fe to form a BCC and Nb-rich phase formation in this HEA system [20]. Moreover, the secondary C14 phase formation alongside the primary C14 was reported in HEAs with 9 at.% Fe and 18 at.% Fe concentrations at 1073 K and 11173 K homogenization steps, respectively [22]. It was mentioned that Nb destabilizes the secondary C14 phase in HEA.

1.4. Basic Concept of High Entropy Alloys

Even though the high configurational entropy has been considered for the formation of simple amorphous or crystalline solutions instead of complex microstructures [2], phase structure is another important criterion of HEAs. Phase formation directly depends on elemental compositions of alloys [24], and can be explained by the Gibbs Phase Rule using the following equation [2], [6]:

$$P + F = C + 1 \quad (1.1)$$

where F and C are the degrees of freedom and number of components, respectively. The Gibbs Phase Rule explains that the number of phases (P) in a condensed system cannot be higher than C + 1 in equilibrium. However, HEAs show less number of phases than expected, which can be explained by the low diffusivity of HEAs [6, 10, 25]. “High entropy” brought a new motivation for HEAs with a definition based on the magnitude of configurational entropy of mixing, S_{conf.} or S_{mix}, which is calculated by the following Boltzmann equation [2]:

$$\Delta S_{conf.} = k \ln w \quad (1.2)$$

where k is Boltzmann’s constant, and w is the number of configurations for being mixed or shared of available energy between atomic particles in the system. The change in configurational entropy per mole for an n-component alloy system with x_i atomic fraction can be calculated using the following relationship:

$$\Delta S_{conf.} = -R \sum_{i=1}^N x_i \ln x_i \quad (1.3)$$

Combining the equations (1.2) and (1.3), the magnitude of configurational entropy for an equiatomic alloy in its liquid or solid solution state can be calculated by the following equation:

$$\Delta S_{conf.} = -k \ln w = -R \left(\frac{1}{n} \ln \frac{1}{n} + \frac{1}{n} \ln \frac{1}{n} + \dots + \frac{1}{n} \ln \frac{1}{n} \right) = R \ln n \quad (1.4)$$

where R is the gas constant. Based on the above relationship, it is clear that the change in configurational entropy depends on the component number. It was reported that when the value of $\Delta S_{conf.} < 0.69R$, the alloy will be low entropy, when $0.69R < \Delta S_{conf.} < 1.61R$, the alloy will be medium entropy, and when $\Delta S_{conf.} > 1.61R$, the alloy will be high entropy alloy [2], [6]. Figure 2.2 shows the schematic plot of ΔS_{mix} for a ternary alloy system based on the classification of the high entropy region [25].

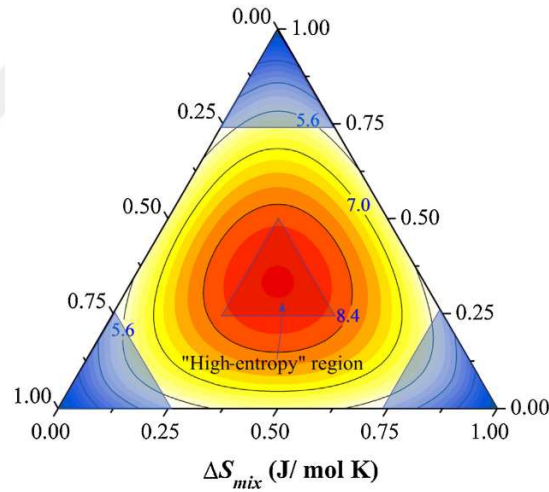


Figure 1. 2. The schematic plot of ΔS_{mix} for a ternary alloy system. Red region, which is limited with 8.4 and up to 9.15 J/mol.K represents high entropy, while blue regions are indicating conventional alloys [12].

1.5. Four Core Effects

The formation of HEAs is mainly determined by the core effects. These effects are high entropy, severe lattice distortion, sluggish diffusion, and cocktail effects. High entropy effect as a main concept of HEAs explains thermodynamic relationships.

Severe lattice distortion affects the kinetic properties throughout phase transformations. Sluggish diffusion effect is the explanation for the affection of low diffusion rates to mechanical and chemical properties. Finally, the cocktail effect, which is a separate characterization for HEAs, has an overall impact on the properties of composition, structure, and microstructure [5,8, 10, 26].

1.5.1. High Entropy Effect

High entropy effect explains the stable phase formation and simpler microstructure observation in HEAs compared to intermetallic alloys composed of 5 or more principle metallic elements. Solid solution phases are different from elemental phases based on one metallic element, and intermetallic compounds such as Ni_2Ti , Al_3Co , etc. Those phases are based on one solvent and solute metallic elements [8]. Solid solutions can be either random solid solutions that may have the crystal structures of face-centered cubic (FCC), body-centered cubic (BCC), hexagonal close-packed (HCP), or ordered solid solutions that are composed of intermetallic compounds [6].

Solid solution phase formation is speculated to result in single or a few phases in HEAs, which is lower than predicted in other multi-component alloys. This prediction is explained due to high mixing entropy that allows to increase the solubility of elements and prevent phase separation throughout solid solutions and intermetallic compounds [10].

Mixing enthalpy (ΔH_{mix}) and mixing entropy (ΔS_{mix}) are the primary considerations to explain the high entropy effect. ΔS_{mix} of a system accelerates the solid solution formation contrary to negative or positive ΔH_{mix} , which helps accelerate elemental or compound phase formation [2], [6]. In an equilibrium state, when the lattice strain energy between atoms is neglected, elemental phases have small-negative ΔH_{mix} and small ΔS_{mix} , intermediate phases have less large-negative ΔH_{mix} , but medium ΔS_{mix} , and solid solution phases have medium-negative ΔH_{mix} and high ΔS_{mix} [6]. The comparison of ΔH_{mix} and ΔS_{mix} for different phase structures are listed in Table 1.1.

Table 1. 1. ΔH_{mix} and ΔS_{mix} of elemental, compound, intermetallic, and solid solution phases for n-element HEAs.

Comparative Phases	ΔH_{mix} (kJ.mol ⁻¹)	ΔS_{mix} (J.K ⁻¹ .mol ⁻¹)
Elemental Phases	~0	~0
Intermetallic Phases	Less large-negative	Medium
Solid Solution Phases	Medium-negative	High

1.5.2. Severe Lattice Distortion

Severe lattice distortion effect gives information about the direct impact of crystal structure and atomic size difference to explain lattice distortion, which is based on dislocation motions in a whole solute matrix of high entropy alloy. The matrix of HEAs is composed of different sizes of different elemental solute atoms that spread throughout the matrix and surround each other. Because of these dislocation motions occurring due to size differences between atoms, the whole solute matrix suffers severe lattice dislocation [6, 27]. The change of the entire solute matrix due to dislocation motion is shown in a two-dimensional schematic image in Figure 1.3 [27], and the atomic order of BCC and FCC crystal structures in a solid solution of a HEA consisting five principle elements is exhibited in Figure 1.4 [28]. This effect was confirmed by the study of Yeh et al. [28]. According to this effect, lattice distortion increases strain energy, reduces thermal deviation between atoms, increases the hardness and strength of alloy after heat treatment processes, and directly affects the excellence of crystal structure [2, 27-28].

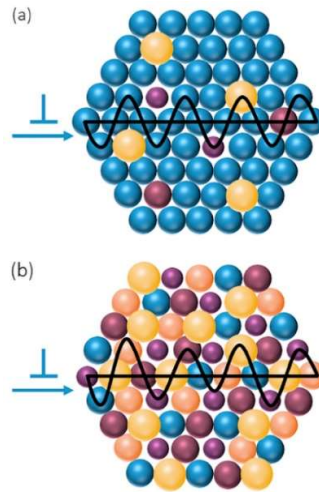


Figure 1.3. Two-dimensional schematic image of dislocation movements in the whole solute matrix of a high entropy alloy with five principle elements. Figure shows the change in solid solution from (a) dilute to (b) complex and concentrated structure by overcoming the periodic Peierls-Nabarro energy barrier field [27].

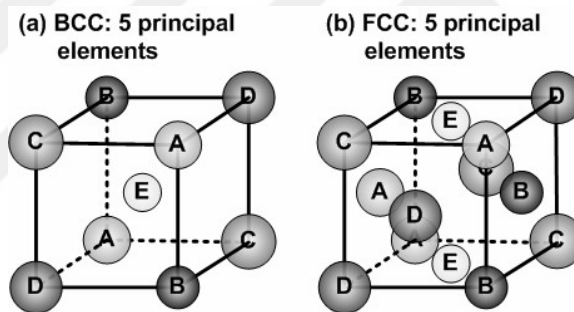


Figure 1.4. (a) BCC and (b) FCC crystal structures of a HEA composed of 5 elements [28].

Atomic size difference is the main reason for the lattice strain energy between distorted atoms, and that is the particular factor for the severe lattice distortion, also phase formation in HEAs. According to Tsai et al. [29], large-sized atoms in atomic structure cause high lattice strain energy, destabilization in structure, intermetallic phase formation, and smaller diffraction peak intensity during the XRD process [5, 6, 28]. Therefore, smaller atomic size difference in a HEA is preferred for a more stable solid solution phase formation, smaller strain energy, higher intensity of diffraction peaks in XRD, and lower thermal dependency in mechanical properties.

1.5.3. Sluggish Diffusion Effect

Sluggish diffusion effect lowers the diffusion rate, so the diffusion becomes slower in HEAs compared to other conventional alloys. Tsai et al. reported that sluggishness in diffusion is related to the number of composed elements in HEAs, not to compositions of elements [30]. It was proved in Figure 1.5 that Co, Cr, Fe, Mn, Ni independently have higher values of normalized activation energy Q/T_m , where Q is activation energy and T_m is the melting point of the solute matrix, which means they have lower diffusion rates in matrix of CoCrFeMnNi high entropy alloy than other conventional alloys matrices [2, 6, 30].

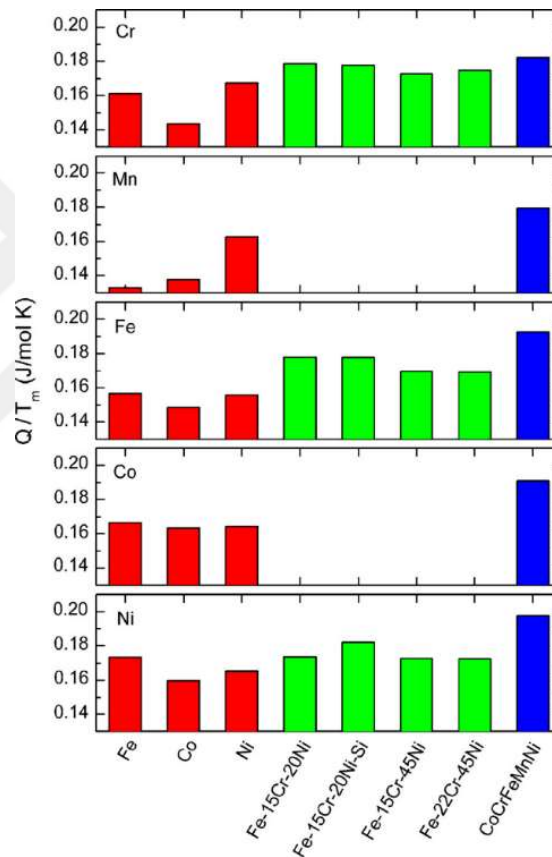


Figure 1. 5. Normalized activation energy values of Cr, Mn, Fe, Co, Ni in different alloy matrices [30].

Sluggish diffusion effect is the answer for extreme strength values at elevated temperatures [31], formation of nanostructures [5], more stable random solid solution phase, and a slower rate of crystallization [32] in HEAs. Therefore, it has positive effects on slower grain growth rate and higher creep resistance [2, 6].

1.5.4. The Cocktail Effect

The cocktail term refers to the mixture of metallic elements in the metallic alloys. It was first reported by S. Ranganathan [33] to describe the formation of HEAs, bulk metallic glasses, superplastic and superelastic alloys through their exclusive physical, functional, and structural properties [6, 31, 33]. The cocktail effect in HEAs is related to phase number, size, boundaries, shape, distribution, and properties, which are contributed by the compositional design of alloy, and properties of each composed element. Liu et al. [34] reported that Al content caused a tendency in phase formation from FCC to BCC, and causes an increase in hardness in $Al_xCoCrCuFeNi$ HEA because of its BCC crystal structure, which clarifies the cocktail effect. Furthermore, in an article published by Kang et al. [35], the new FCC phase formed in $AlCo_xCrFeNi$ HEA with the concentration Co element due to the cocktail effect in HEAs.

1.6. Phase Formation in High Entropy Alloys

HEAs are known to be unique materials with their remarkable ability to form a single crystal phase even though they have high number of components and high configurational entropies. HEAs may have different types of crystal structures; BCC, FCC, and FCC+BCC, depending on the alloy contents, alloy composition, and thermodynamic parameters. The phase formation significantly affects the properties of HEAs.

1.6.1. Parametric Approaches in Phase Selection

The phase formation of a multi-component system in an ideal solution ($\Delta H_{mix} = 0$) or a regular solution ($\Delta H_{mix} \neq 0$) is controlled by Gibbs Free Energy of mixing (ΔG_{mix}). The concept of HEAs requires the configurational entropy, $\Delta S_{conf.} \geq 1.61R$. HEAs may have intermetallic or even amorphous phases, together with solid solution phases due to differences in the atomic sizes and electronegativities between constituent elements, valence electron configuration, and elemental compositions.

Hume-Rothery Rules explains the set of principles that were developed to control phase formation and alloying behavior for alloy systems [2]. These rules state that (1) the atomic sizes between atoms of additional elements (solute atoms) and principal elements (solvent atoms) must not be more than 15%, also should be less than 8% for

ideal solubility, (2) crystal structures of both additional and principal elements must be the same for maximum solubility, (3) there should be the same valency between both solute and solvent atoms, (4) electronegativity of each element shall be similar or nearly equal for prevention of possible intermetallic phase formation [2, 6, 36-37]. However, because of the insufficiency of the second rule, Hume-Rothery rules are not qualified alone to explain the possibility of the formation of a single solid solution phase despite different crystal structures of each element in a HEA [36, 38]. Therefore, some empirical parameters are used in the case of phase selection for the design of HEAs.

Zhang et al. [39] proved that the solid solution phase formation depends on the atomic size difference. Small difference at atomic radii between each atom helps the formation of a stable solid solution phase in HEA [37], and reduces strain energy between atoms. Other Atomic size difference, δ , for an N-element multi-component alloy system where the atomic radius of i th element, r_i , can be estimated by the following equation [8, 24].

$$\delta = 100 \sqrt{\sum_{i=1}^N x_i \left(1 - r_i / \sum_{i=1}^N x_i r_i \right)^2} \quad (1.5)$$

Stable solid solutions are expected to be formed in one condition, which is $\delta \leq 6.6$ [6], [40].

Gibbs Free Energy (ΔG_{mix}) thermodynamically controls phase formation of a multi-component system in an ideal solution ($\Delta H_{\text{mix}} = 0$) or a regular solution ($\Delta H_{\text{mix}} \neq 0$). ΔG_{mix} calculated by the following equation:

$$\Delta G_{\text{mix}} = \Delta H_{\text{mix}} - T \Delta S_{\text{mix}} \quad (1.6)$$

where the change in Gibbs Free Energy, ΔG_{mix} , is related to mixing enthalpy (ΔH_{mix}), mixing entropy (ΔS_{mix}), and temperature (T) of the system, higher component numbers can lower ΔG_{mix} with the contribution of ΔS_{mix} [2, 5, 24]. Mixing enthalpy is considered as another influencer factor for phase formation. It is used for the

characterization of chemical compatibility between elemental components of HEAs [26]. The following equation is used to calculate ΔH_{mix} :

$$\Delta H_{mix} = \sum_{i=1, i \neq j}^N 4\Delta H_{AB} x_i x_j \quad (1.7)$$

where $4\Delta H_{AB}$ is defined as mixing enthalpy of binary A-B alloys, N is the number of elements, and x_i and x_j are the atomic percentages of i th and j th elements in liquid or random solid solution state. Finally, ΔS_{mix} is calculated with the following equation:

$$\Delta S_{mix} = -R \sum_{i=1}^N x_i \ln x_i \quad (1.8)$$

where R is the gas constant of $8.314 \text{ J/mol}\cdot\text{K}$, and x_i is the atomic percentage of i th element [6, 24]. Guo et al. concluded that solid solution formation occurs at $-22 \leq \Delta H_{mix} \leq 7 \text{ kJ/mol}$, and $11 \leq \Delta S_{mix} \leq 19.5 \text{ J/K}\cdot\text{mol}$ [36].

The other determinative parameter for the expected stability of solid solution formation in multi-component alloys is Ω , which can be by the following equation:

$$\Omega = \frac{T_m \Delta S_{mix}}{|\Delta H_{mix}|} \quad (1.9)$$

The criterion indicates that in case $\Omega \geq 1.1$, the stable solid solution in HEAs can be formed [6], [42].

Guo et al. reported another empirical parameter, the valence electron configuration (VEC), to determine the phase formation in HEAs [29]. The VEC gives specific information about expected crystal structure and phase stability for a solid solution. Electron concentration is the average number of traveling electrons per atoms, e/a . VEC number of a multi-component alloy is defined as the summation of the VEC number of each composed element by its atomic percentage. They are calculated by the following equations:

$$e/a = \sum_i^N x_i (e/a)_i \quad (1.10)$$

$$VEC = \sum_i^N x_i (VEC)_i \quad (1.11)$$

It was reported that when $VEC \geq 8.0$, the FCC solid solution is stable, when $VEC < 6.87$, the BCC solid solution is stable, and $6.87 \leq VEC < 8.0$, the alloy will have a dual-phase structure of FCC + BCC [43].

The other important parameters related to the structure of HEAs, such as theoretical density, ρ_{theor} can be determined using the following relationship:

$$\rho_{theor} = \frac{\sum c_i A_i}{\sum \frac{c_i A_i}{\rho_i}} \quad (1.12)$$

where ρ_i , c_i , and A_i are density, nominal composition, and atomic weight of the i th element, respectively [20]. The melting point of a HEA (T_m^{mix}) can be calculated using the following equation where c_i , $(T_m)_i$ are nominal composition and melting point of i element [31].

$$T_m^{mix} = \sum c_i (T_m)_i \quad (1.13)$$

The determination of lattice parameters of the corresponding crystal structures of HEAs is significant. The unit cell geometry of a crystal structure system is defined by lattice parameters, which are three edge lengths, a , b , c , respectively in an x - y - z coordinate system, and three interaxial angles, α , β , γ of a unit cell. The axial relationship in cubic systems is such as $a=b=c$, and each interaxial angle equals 90° [44]. The determination of a crystal structure, only in cubic systems, is based on crystallographic planes called Miller indices (hkl), which either parallel or intersect with these three edge lengths. Miller indices are defined by the lattice parameter of a crystal structure (a), and interplanar spacing (d_{hkl}) between two parallel planes of atoms

A-A' and B-B' diffracting X-Ray beams. The condition for the formation of X-ray diffraction is exhibited in Figure 1.6.

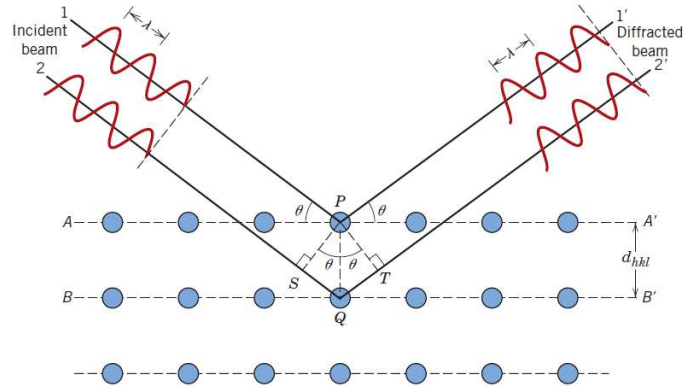


Figure 1. 6. X-Ray Diffraction occurred by atomic scattering [44].

The interplanar spacing, d is determined using Bragg's law;

$$n\lambda = 2d_{hkl}\sin\theta \quad (1.14)$$

where n is the order of reflection, λ is the wavelength of x-ray, and θ is the angle between the incident x-ray beam and the plane of atoms. Thus, d_{hkl} , as a function of Miller indices and lattice parameters, is calculated by the following equation [44].

$$d_{hkl} = \frac{a}{\sqrt{h^2 + k^2 + l^2}} \quad (1.15)$$

The lattice parameter can be determined using the combination of equations (1.14) and (1.15).

1.6.2. Phase Formation in High Entropy Alloys

The formation of ordered and disordered phases are commonly seen in HEAs. Previous studies reported the formation of terminal, intermetallic, and solution phases in HEAs. Terminal phases are also known as elemental phases, and include one dominant metallic element. Intermetallic phases are the compounds that have different and specific superlattices such as NiAl, Ni₃Ti, etc. The solution phases are the compounds

that mostly have simple crystal structures (FCC, BCC, HCP), and rarely complex (NiAl, Ni₃Ti, etc.) structures.

1.6.2.1. Solid Solution Phases

HEAs have a wide range of phase formation, such as simple disordered phases, simple ordered phases, and complex ordered phases due to different crystal structures [2, 5, 45]. The simple ordered FCC, BCC, and/or HCP crystal structures are observed mainly in HEAs. Solid solution phases within HEAs form at elevated temperatures, but they can experience with phase transformations at lower temperatures. This situation reduces the effect of high mixing entropy in solid solution phase stability. Additionally, sluggish diffusion has a favorable impact on reducing substitutional diffusion, nucleation, growth rate, and so phase transformation rate at lower temperatures. Therefore, phase selection in HEAs is more referable at elevated temperature conditions compared to the as-cast condition of alloys at lower temperatures [2, 37].

1.6.2.1.1. Phase Formation in Equiatomic High Entropy Alloys

Since the first HEA concept was proposed in equiatomic composition, the following studies to understand the mechanism of the formation of stable solid solution phases and their properties mainly concentrated on equiatomic HEA systems. Solid solution phases in HEAs have predominantly contains simple FCC, BCC crystal structures, or multiphase FCC+BCC crystal structure. Furthermore, single HCP HEAs were also reported. Simple phase structures have a great tendency to be formed in solid solutions of equiatomic HEAs. The formation of simple phase structures from these complex systems generally occurs due to the insufficient time for the formation of any secondary phase or intermetallic phase. In addition to these simple solid solutions, there is a tremendous increase in the reports of HEAs with multiphase structure [2, 37].

1.6.2.1.1.1. BCC Phase Formation

The formation of BCC solid solution phases is widely seen in HEAs. Senkov et al. [20] reported the first BCC refractory HEA that possesses excellent mechanical and thermal properties at the cryogenic, room, and high temperatures. Manzoni et al. reported [46],

single BCC phase in equiatomic AlCoCrFeNi alloy even though the expected crystal structure is FCC+BCC due to its VEC number of 7.2. They explained that this single-phase formation is due to the concentration of Al element, and nearly similar atomic sizes and the electronegativities of the constituent elements. Table 1.2 tabulates the atomic radii and electronegativity values of each transition element in this main alloy. It was also reported that the stable phase formation seems more likely to be controlled by binary elemental phases rather than single elements in HEAs [2]. Al-Ni rich phase, which is an ordered BCC phase called B2 phase, is the primary crystal structure governing phase formation. This structure, formed in the matrix of the microstructure of alloy, displayed excellent durability up to high-stress levels at cryogenic temperatures because of its strongly ordered structure [2, 46-47].

Table 1. 2. Atomic radii and electronegativity values of elements in AlCoCrFeNi HEA.

Elements	Atomic radius (nm)	Electronegativity
Al	0.14317 [12]	1.61 [13]
Co	0.12510 [12]	1.88 [13]
Cr	0.12491 [12]	1.66 [13]
Fe	0.12412 [12]	1.83 [13]
Ni	0.12459 [12]	1.91 [13]

BCC HEAs are mainly preferred as refractory high entropy alloys (RHEA) due to their significant mechanical properties, such as high strength and high hardness at high temperatures. For example, Senkov et al. [48] reported the single BCC phase formation in TaNbHfZrTi RHEA. Their findings showed that this alloy has good phase stability up to 1473 K, exhibit yield strength of 929±15 MPa, and Vickers hardness value of 3826 MPa after the hot isostatic pressing process.

1.6.2.1.1.2. FCC Phase Formation

Solid solutions with FCC structures are the rarely seen compared to the solutions that have BCC structures. The curial advantage of FCC HEAs compared to BCC HEAs is their more sluggish diffusion kinetics [2]. FCC HEAs promise more advantages for the cryogenic, room, and even high-temperature applications than BCC HEAs. The

phase formation in HEAs mainly depends on the constituent elements. The commonly known Cantor alloy, CoCrFeMnNi, has a single-phase FCC structure, although each constituent element has a different phase structure. When switched to the VEC criteria, FCC structure is expected from its value of 8.0. The nearly similar atomic sizes and electronegativities of constituent elements also result in single solid solution formation. These values are listed in Table 1.3.

Table 1. 3. The atomic radii and electronegativity values of constituent elements of CoCrFeMnNi HEA.

Elements	Atomic radius (nm)	Electronegativity
Co	0.12510 [12]	1.88 [13]
Cr	0.12491 [12]	1.66 [13]
Fe	0.12412 [12]	1.83 [13]
Mn	0.13500 [12]	1.55 [13]
Ni	0.12459 [12]	1.91 [13]

Gludovatz et al. reported that FCC CoCrFeMnNi HEA shows superior mechanical properties and solid solution strengthening mechanisms at room and even cryogenic temperatures due to the low stacking-fault energy and high lattice friction [11, 27]. Gludovatz et al. proposed that the ultimate tensile strength (σ_{UTS}) and yield strength (σ_y) value of CoCrFeMnNi HEA increase by ~85% (to 1280 MPa) and ~70% (759 MPa), respectively, when the temperature decreases from 293 K to 77 K, as shown in Figure 1.7 [11]. They reported the increase in ductility of the alloy with decreasing temperature. They proposed that the fracture toughness, K_{JIC} , of the alloy were determined as 217 MPa.m^{1/2}, 221 MPa.m^{1/2}, and 219 MPa.m^{1/2} at 293 K, 198 K, and 77 K, respectively. The FCC Cantor alloy has similar fracture toughness values with standard austenitic stainless steels, such as 316L and 304L (fracture toughness in the range from 175 to 400 MPa.m^{1/2}) at room temperature and Ni-based cryogenic steels such as 5Ni or 9Ni steels (fracture toughness in the range from 100 to 325 MPa.m^{1/2}) at cryogenic temperature [2, 11].

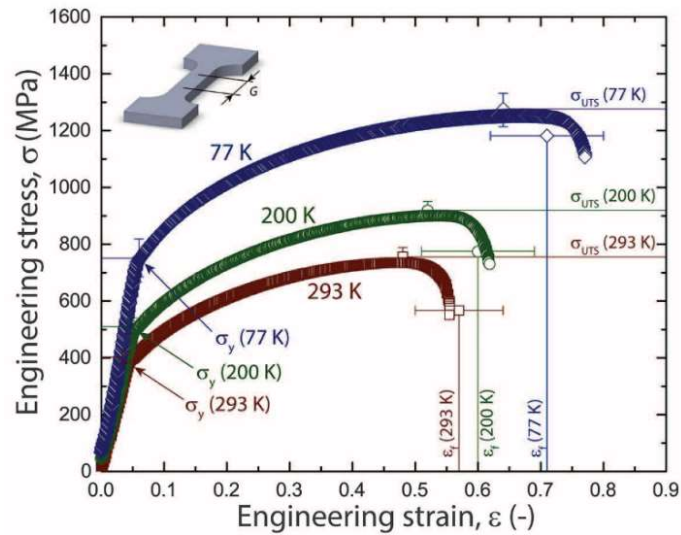


Figure 1. 7. Engineering stress and strain graph for CoCrFeMnNi at different temperatures [11].

1.6.2.1.1.3. Multiphase FCC+BCC Structure

The phase formation in HEAs depends on the empirical calculations such as ΔH_{mix} , ΔS_{mix} , ΔG_{mix} , δ (atomic size difference), and VEC number. The phase formation may also vary depending on the different processing techniques, such as arc melting, ball milling, spark plasma sintering (SPS) furnace melting, etc. due to different solidification rates achieved with these techniques [2]. The CoCrFeNiCuAl HEA synthesized by arc melting has a mixed FCC+BCC structure [7, 49], while a supersaturated single BCC phase was observed when the alloy was processed for 60 hours by mechanical alloying known as the ball milling process [50]. There are also differences in the phase formations depending on different durations of the alloying processes. Double FCC+BCC phase structure was observed after 20 hours ball milling process [51]. Figure 1.8 illustrates the XRD analysis of 20h ball milled equiatomic CoCrFeNiCuAl and nonequiatomic CoCrFeNiCuAl_x HEAs.

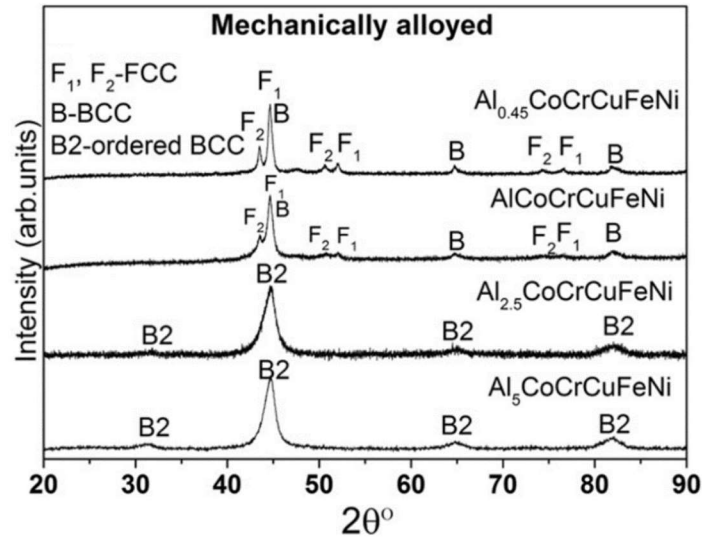


Figure 1. 8. XRD patterns of equiatomic AlCoCrFeNi HEA and nonequiatomic $Al_xCoCrFeNi$ HEA powders after 20h ball milling process [51].

Avila-Rubio et al. [40] studied AlCoFeNi, AlCoFeNiMo, AlCoFeNiTi, and AlCoFeNiMoTi alloys synthesized by mechanical alloying and conventional sintering methods. They reported that AlCoFeNiMo has a mixed 2BCC+FCC phase after 15h ball milling process, while the same alloy has a mixed BCC+FCC phase after the conventional sintering process at 1373-1473 K. Moreover, single BCC phase formation was observed in AlCoFeNiTi HEA after 15h ball milling, while multi 2FCC+BCC phase formation was observed in the same alloy after sintering. They also reported that ball-milled AlCoFeNiMoTi HEA has a mixed FCC+2BCC phase while the sintered AlCoFeNiMoTi alloy has 2FCC+BCC phase formation. Figure 1.9 and Figure 1.10 represent the XRD patterns of these alloy synthesized at corresponding techniques. The hardness values are also depending on processing routes. The sintered alloys have lower hardness values than the 15h ball milled ones. Figure 1.11 shows the microhardness values of these alloys. The microhardness test results were determined as 1225 HV and 894 HV for ball-milled AlCoFeNiMoTi and sintered AlCoFeNiMoTi, respectively. The microhardness test results were measured as 556 HV for sintered AlCoFeNi, and 749 HV for ball-milled AlCoFeNiTi alloys. The high hardness values were devoted to the constituent elements and the tendency of stable solid solution formation in terms of the conditions of $\delta \leq 6.6$ and $\Omega \geq 1.1$ [6, 40, 42].

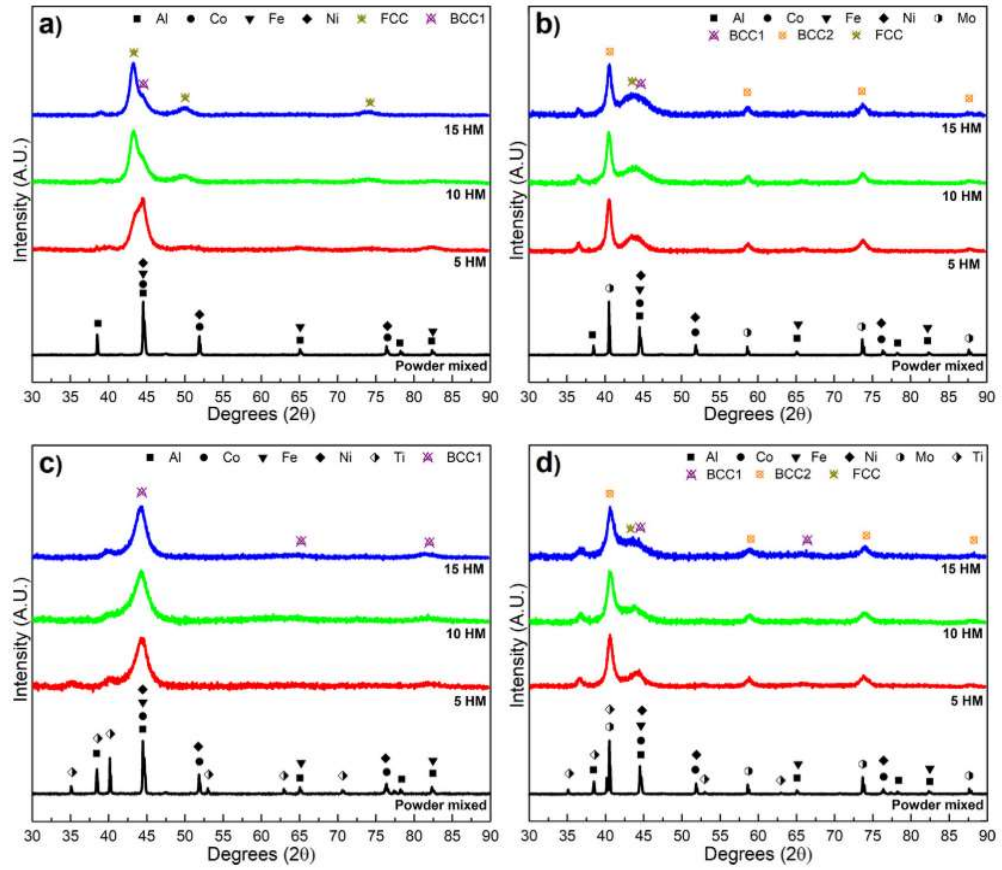


Figure 1. 9. XRD patterns of ball milled (a) AlCoFeNi, (b) AlCoFeNiMo, (c) AlCoFeNiTi, (d) AlCoFeNiMoTi HEAs at different times [40].

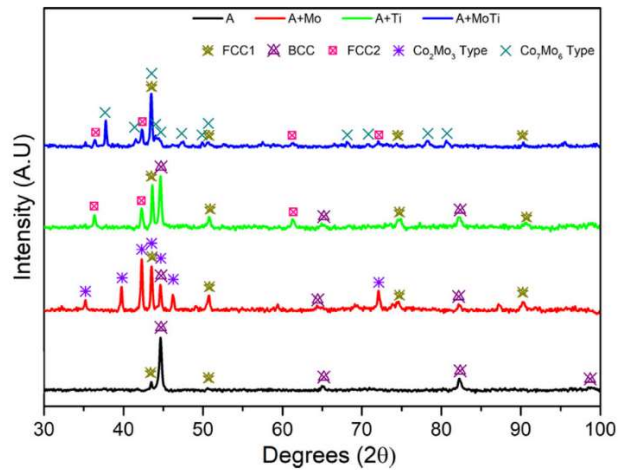


Figure 1. 10. XRD patterns of sintered HEAs at different temperatures [40].

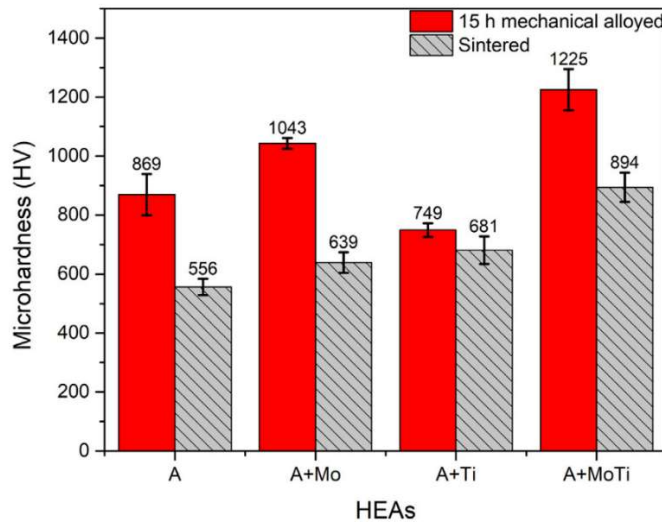


Figure 1. 11. Microhardness results of HEAs at different processing [40].

1.6.2.1.2. Solid Solution Formation in Nonequiatomic High Entropy Alloys

The non-equiatomic HEAs exhibit solid solutions with FCC, BCC, or mixed FCC+BCC structures similar to equiatomic HEAs. Due to the differences in elemental compositions, equiatomic and nonequiatomic alloys with same element constituents may show different phase formations. Tung et al. [49] showed that equiatomic AlCoCrFeCuNi HEA has a mixed FCC+BCC phase while nonequiatomic Al_{0.5}CoCrFeCuNi HEA has a single FCC phase, and nonequiatomic AlCoCrFeCu_{0.5}Ni HEA has a single BCC phase. Figure 1.12 illustrates the XRD patterns of nonequiatomic AlCoCrFeCuNi based HEAs.

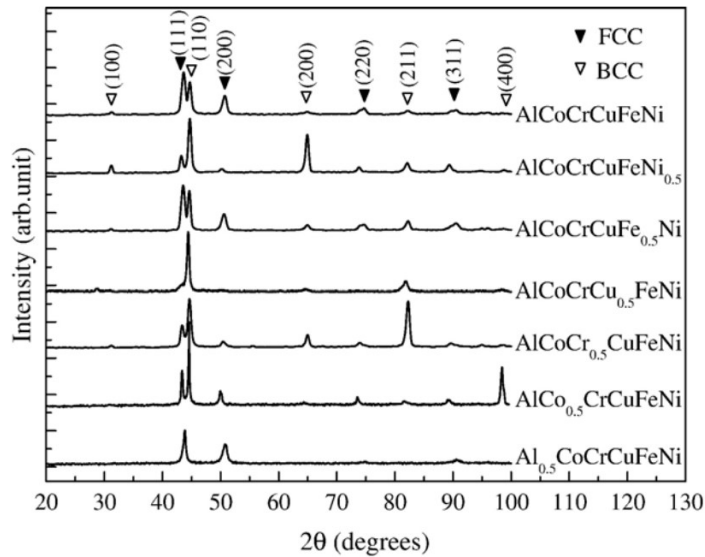


Figure 1. 12. XRD patterns of as-cast Al-Co-Cr-Cu-Fe-Ni based HEAs [49].

1.6.2.1.2.1. The Effect of Al on HEAs

Aluminum is one of the most common alloying elements of HEAs. Regarding its nearly similar electronegativity and atomic size values with most transition metal elements [12-13], and functional behavior in oxidation and wear resistance [14-15], It is interesting that Al element has FCC crystal structure, but it increases a tendency towards BCC structure formation in HEAs. He et al. [16] studied a set of $Al_xFeCoNiCrMn$ based HEAs with Al concentrations varying from 0 to 20 at.%. They reported that the Al element is a BCC stabilizer in single FCC FeCoNiCrMn Cantor HEA, as shown in Figure 1.13. The HEA with 9 at.% Al has strong BCC reflections in addition to FCC reflections. The ordered BCC structure, main peak indexed as (100), appears when the alloy contains 10 at.% of Al. A single BCC phase structure is observed when the HEA has 20 at.% Al.

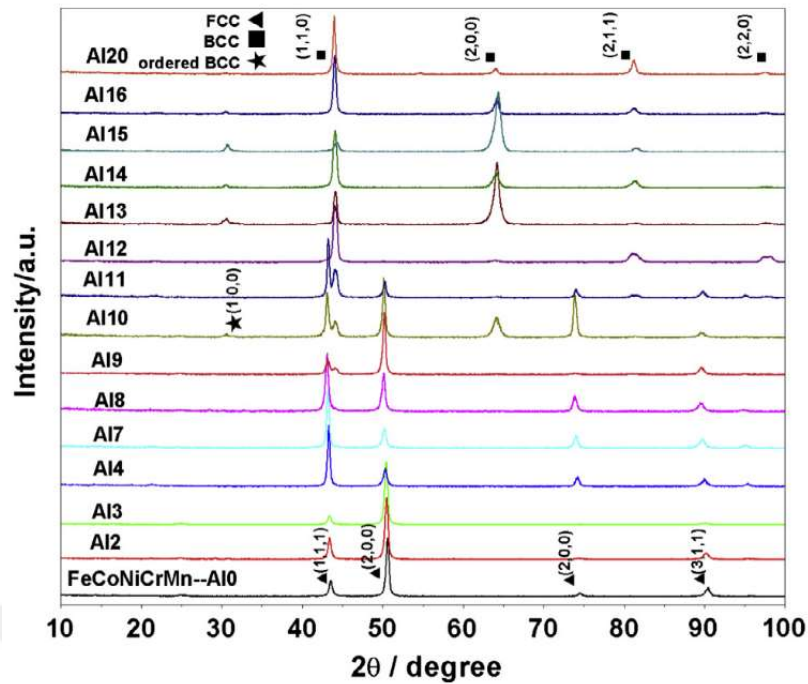


Figure 1. 13. XRD patterns of $\text{Al}_x\text{FeCoNiCrMn}$ based HEA with different concentrations of Al element [16].

The mechanical properties of the alloys also depend on the Al concentrations of the alloys. Figure 1.14 shows the engineering stress-strain curves of as-cast $\text{Al}_x\text{FeCoNiCrMn}$ HEAs ($x=0, 4, 7, 8, 9, 10, 11$ at.%). It was observed that the alloys have lower strength values with higher Al concentrations. The alloy with 0 at.% Al has the most ductile behavior with its lowest strength value and highest strain percent, while 11 at.% Al showed the most brittle character. Furthermore, it is seen from Figure 1.14 (b) that tensile strength value exhibits a slight increase from 496 to 529 MPa, and yield strength increases from 209 to 242 MPa when Al concentration increases from 0 to 7 at.% Al in the alloy. The alloy with 11 at.% Al has the tensile and yield strength values of 1174 MPa and 832 MPa, respectively. The tensile strain slightly decreases from 61.7% 0 at.% Al alloy to 47.2% in 7 at.% Al alloy, and then reaches its lowest value %7.7 in 11 at.% Al. Figure 2.15 (c) shows the Vickers microhardness results of $\text{Al}_x\text{FeCoNiCrMn}$ ($x=0, 2, 4, 7, 8, 9, 10, 11, 12, 13, 14, 15, 16, 20$) alloys. The microhardness test results show an increase in the concentration of the Al element. The gradual increase in hardness values is observed from 176 HV to 182 HV when Al concentration is increased from 0 to 7 at.%. The HV value increases sharply to 538 HV for $\text{Al}_{14}\text{FeCoNiCrMn}$ alloy. The increase in hardness value due to the increase of

Al concentration can be explained by the formation of the intermetallic B2 phase. B2 phase is an ordered BCC phase that enriched with Al and Ni [18, 53-54]. The HV values remain constant for the alloys that contain 16 and 20 at.% Al [16].

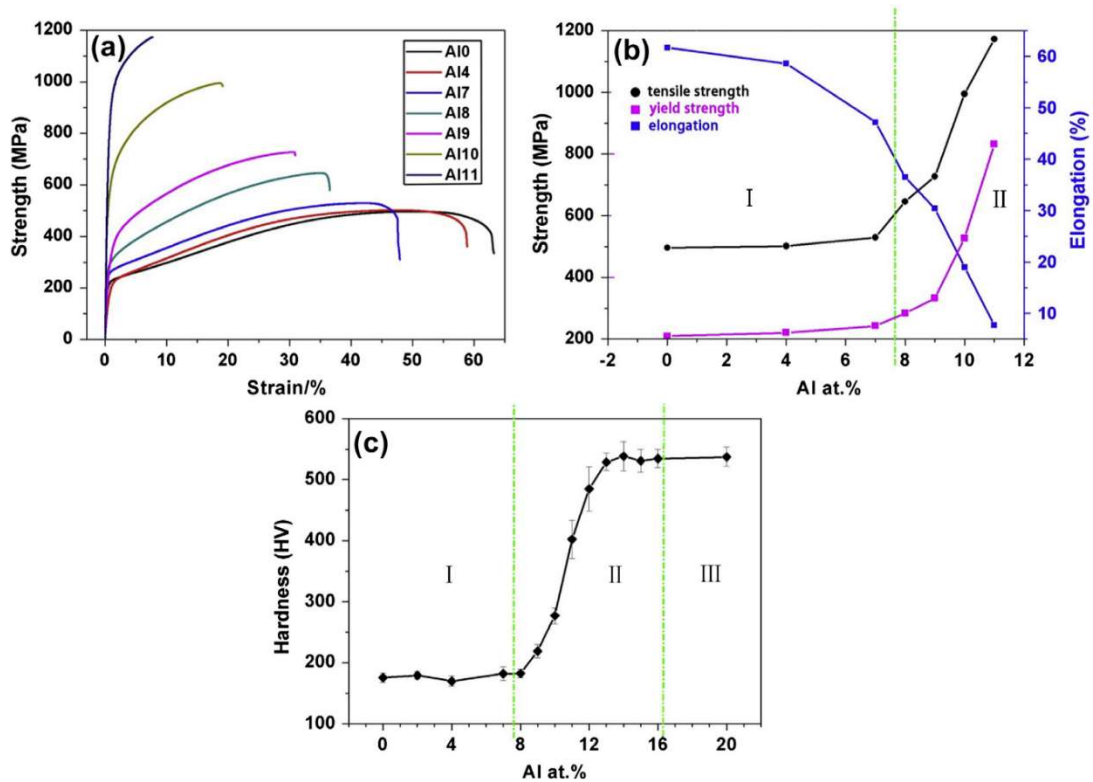


Figure 1. 14. (a) Engineering stress-strain curve, (b) tensile strength, yield strength, and elongation, and (c) Vickers hardness values of as-cast $\text{Al}_x\text{FeCoNiCrMn}$ concerning different Al concentrations [16]. The hardness graph of HEAs are separated as region I (single FCC alloys with $x < 8$), region II (mixed FCC+BCC phase alloys with $8 \leq x < 16$), and region III (available FCC alloys with $x > 16$).

1.6.2.1.2.2. Effect of Transition Metals

The most common HEAs mainly have transition metals. These transition metals are selected due to their similar atomic sizes and electronegativities, and less-negative mixing enthalpy values between each other. Co, Cr, Fe, Ni, Mn, and Cu are the commonly used transition metallic elements in HEAs. On the other hand, the high melting point transition metals such as Mo, Nb, V, Ti, Hf, Ta, even Cr, etc. are preferred as refractory HEA elements for high-temperature applications. Qin et al. [52] revealed that the Co element, with VEC number of 9, stabilizes the FCC phase formation in single BCC phase AlCoCrFeNi HEA. Figure 1.15 presents the XRD

patterns of $(\text{AlCoCrFeNi})_{100-x}\text{Co}_x$ alloy. The additional FCC peaks and the disappearance of most BCC peaks can be observed in $(\text{AlCoCrFeNi})_{92}\text{Co}_8$ system when $x=12$. They reported the formation of mixed FCC+BCC phase when $x=16$. It is observed that the increase in Co concentration stabilizes the FCC phase in HEA, enhances the plasticity, and lowers the fracture strength.

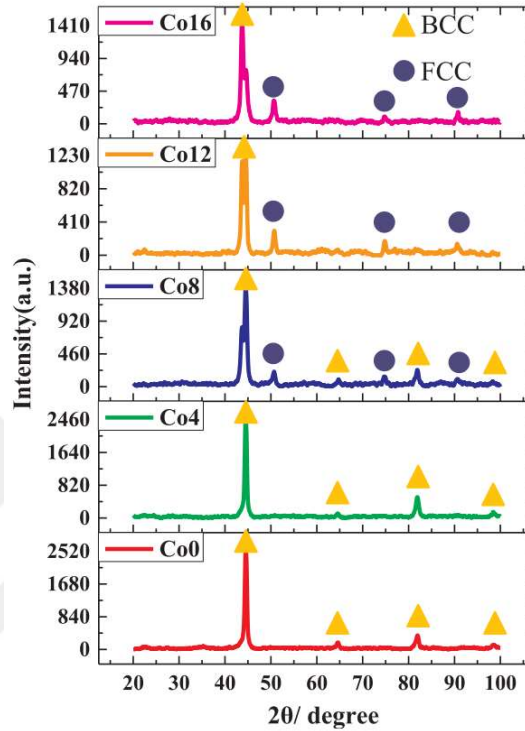


Figure 1. 15. XRD patterns of $(\text{AlCoCrFeNi})_{100-x}\text{Co}_x$ HEAs ($x=0, 4, 8, 12, 16$) [52].

Koppoju et al. [53] revealed that Ni is also an FCC stabilizer. Figure 1.16 shows the XRD patterns of as-cast CrMnFeCoNi_x HEAs. The intermetallic tetragonal peaks and an unidentified peak were observed in CrMnFeCoNi_0 alloy, and disappear for the alloy when $x=5$. BCC phase remains when $x=5$. BCC peaks disappear and new FCC peaks appear when $x=10$. Moreover, the hardness of CrMnFeCoNi_x alloy decreases from 310 HV to 160 HV with the addition of 5 at.% Ni, and decreases to 120 HV with the addition of 10 at.% Ni due increase in the volume fraction of FCC phase.

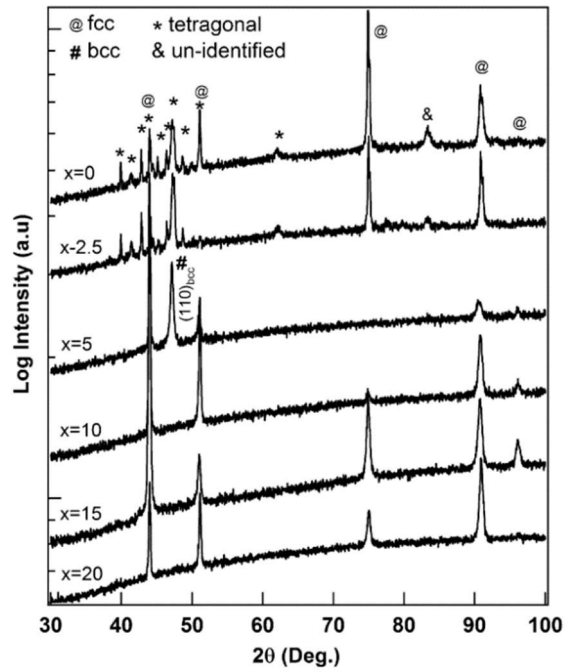


Figure 1. 16. XRD patterns of $(\text{CrMnFeCo})_{1-x}\text{-Ni}_x$ HEA with increasing Ni content [50].

Qiu et al. [54] studied on as-cast Fe_xCoNiCu HEAs. The XRD patterns of as-cast Fe_xCoNiCu HEAs are presented in Figure 1.17. The BCC peak appears when the alloy has 3 mol.% Fe. This study also confirms that Fe is another BCC stabilizer element. The microhardness values were determined as 323 HV, 335 HV, 516 HV, and 654 HV when $x=1, 5, 2, 2.5, 3$ (in at.%), respectively. The tensile strength value of HEA increases from 392 MPa when $x=1.5$ to 474 MPa at $x=2$, and to 639 MPa at $x=2.5$, and then decreases to 576 MPa when $x=3$.

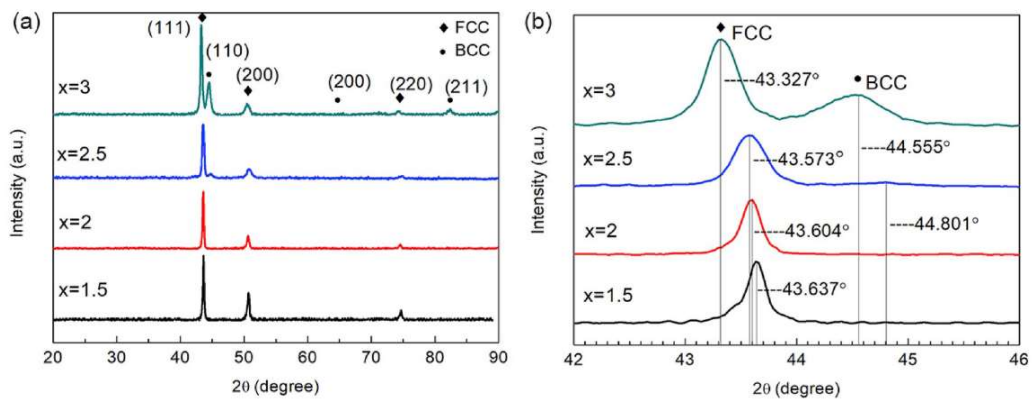


Figure 1. 17. (a) XRD patterns of Fe_xCoNiCu HEAs and their (b) FCC and BCC peak positions with degrees between 42° and 46° angles [54].

1.6.2.2. Intermetallic Phases

Intermetallic compound phases are observed as secondary phases in addition to disordered solid solutions in HEAs [2]. These compounds have ordered structures that can be useful for mechanical, chemical, or thermal enhancements in alloy systems. The formation of these phases depends on both elemental effect, number of components, concentration of each element, electrical or geometrical factors including VEC and electronegativity, and applied temperature for processing [55-56]. Intermetallic compounds that form in HEAs are classified as Laves phase, sigma (σ) phase, B2 phase, and $L1_2$ phase.

1.6.2.2.1. Laves Phase

Laves phases have an AB_2 stoichiometry and are categorized into three groups, such as $MgZn_2$ -type hexagonal C14, $MgCu_2$ -type cubic C15, and $MgNi_2$ -type hexagonal C36 [2]. In the formation of Laves phases, The addition of components and their compositional notations have an important role in the formation of Laves phases. Mishra et al. [56] developed a set of different HEA samples and submitted their ΔS_{mix} , ΔH_{mix} , VEC values in Table 1.4. They revealed the proportional dependence of the addition of more components and the attribution of valence electron configuration (VEC) per atom in the evolution of C14 Laves phases. XRD analysis indicates that the Laves phase peaks shift to higher angles as the number of elements increases [56].

Table 1. 4. Thermodynamic data of Ti-Zr-Ni based HEAs [56].

Alloys	ΔS_{mix} (J/mol.K)	ΔH_{mix} (kJ/mol)	VEC
TiZrNi	9.31	-37.33	5.99
TiZrNiV	11.53	-27.00	5.75
TiZrNiVCr	13.18	-21.76	5.80
TiZrNiVCrFe	14.89	-22.00	6.16
TiZrNiVCrFeMn	16.18	-18.61	6.29
TiZrNiVCrFeMnCo	17.29	-20.06	6.63

Hsieh et al. [57] revealed that $CoCrGeMnNb_xNi$ HEAs have high melting point, high strength, and low density. Also, the alloy easily formed Laves phase when $x=0.25$ (in at.%). Due to the low ΔH_{mix} of Nb with other transition elements, and the ability to

block outward diffusion of active metallic cations, Nb element stabilizes the Laves phase and improves oxidation resistance in HEAs.

1.6.2.2.2. Sigma Phase (σ)

Sigma phase, σ with a tetragonal crystal structure, is a very hard and brittle intermetallic compound phase. This phase mostly observed in Cr-contained transition alloy systems, such as Cr-Ni, Fe-Cr-Ni, Fe-Cr-Mn, Fe-Cr-Mo, and Fe-Cr-Ni-Mo systems [2, 57]. Zhang et al. [55] reported that the σ phase is produced in as-cast single FCC phase $\text{Co}_{34.5}\text{Cr}_{30}\text{Ni}_{26.5}\text{Al}_{5.4}\text{W}_{3.6}$ HEA after 2-hours of water quenching at 1473 K, cold rolling of 70%, and then 1-hour of water quenching at 1173 K [58]. It was reported that the tensile strength and the yield strength of the as-cast alloy increase from 647 MPa and 311 MPa to 1219 MPa and 875 MPa, respectively, after the σ phase strengthening. However, it was revealed that the ductility decreases from 52% elongation to 19% with σ phase formation.

1.6.2.2.3. B2 Phase

B2 phase is a brittle BCC-based ordered intermetallic phase. B2 phase is mostly observed in Al-based alloys containing Co, Cr, Fe, Ni, Cu, Mn, and Ti [2]. It was reported that the presence of the B2 phase improves corrosion resistance and strength of the alloys significantly [16, 59]. Ma et al. revealed [60] that the formation of BCC and B2 phases is promoted with the increase in the concentration of Al in $\text{Al}_x\text{CoCrFeNi}$ HEAs. XRD analysis showed that a single FCC HEA with 9.28 at.% Al switched to BCC and ordered B2 structure when the Al concentration increases to 12.5 at.%, and BCC/B2 phases become stable at $\text{Al}_{0.74}$ (15.63 at.% of Al). They proved that HEA lost its tensile ductility and became very brittle at room temperature due to spinodal decomposition of the BCC and B2 phase.

1.6.2.2.4. L1₂ Phase

L1₂ phase is an ordered FCC-based intermetallic phase. There are few studies about L1₂ phases that show L1₂ phase mostly forms at alloy systems based on transition metals [2]. L1₂ phase formation is mainly reported in AlNi_3 compounds [2], but Al and Ti elements are also considered as strong L1₂ phase stabilizers [61]. He et al. [62] revealed that two arc-melted $(\text{FeCoNiCr})_{94}\text{-Ti}_2\text{Al}_4$ HEAs have single FCC phase and

Ni₃(Ti, Al)-based L₁₂ phase after two different thermodynamic processes separately applied to each of them [62]. These processes were cold rolling of 30%, subsequent annealing at 1273 K for 2 hours, aging at 1073 K for 18 hours (Process 1), and cold rolling of 70%, and then aging at 923 K for 4 hours, followed by water quenching (Process 2).

1.7. Refractory High Entropy Alloys

HEAs serve as a new generation alloy systems due to their excellent mechanical, chemical, and thermal properties in compared to most conventional alloys. Since the first HEA systems were introduced based on transition metals (Co–Cr–Fe–Ni–Mn–Cu), many new alloy systems were developed to promise excellent mechanical and thermal properties for particular applications. HEAs may be divided into several groups based on their application areas. Refractory high entropy alloy (RHEA) is one member of this HEA group. Senkov et al. [20], introduced the first single BCC phase refractory high entropy alloys (RHEAs) in 2010. The RHEAs are based on nine high melting point refractory elements such as Mo, Nb, Ta, W, V, Hf, Zr, Ti, and Cr [5, 19-20, 63-65]. Al element is also used to decrease density and enhance oxidation resistance in refractory alloys [5, 63-65]. This brand new HEA class is considered to promise excellent mechanical properties, excessive environmental behavior (oxidation and corrosion resistance), and wear behavior at even superior temperatures in, aerospace industry [25, 66], nuclear industry [67], and chemical process industry [19].

1.7.1. Mechanical Properties of Refractory High Entropy Alloys

The mechanical properties of alloys are defined by their hardness, yield strength, tensile strength, elastic modulus, elongation percent, fatigue strength, and creep resistance properties. These mechanical properties are controlled mostly by the microstructure of the alloys. The phase formation, the volume fraction of phases [2, 5, 20], and the dislocation motions between the atoms of constituent elements effect the mechanical behavior of the alloys. The processing temperatures also affect the mechanical properties of the alloys. Therefore it brings the motivation to develop new HEAs for cryogenic, room, and high-temperature applications. RHEAs have been

developed due to their better mechanical performances at high temperatures compared to other known Ni-based superalloys.

Senkov et al. developed first single BCC phase equiatomic NbMoTaW and NbMoTaWV RHEAs [20, 68]. NbMoTaW and NbMoTaWV show high HV values of 4455 ± 185 MPa and 5250 ± 281 MPa, respectively. The higher hardness value of NbMoTaWV was explained due to its finer grain size, different strengthening mechanisms, and the addition of V that might cause lattice strain and thus higher hardness [20]. Furthermore, these arc-melted NbMoTaW and NbMoTaWV alloys have high yield strength values of 1058 MPa and 1246 MPa, respectively, at room temperature. However, compressive engineering stress vs. strain curves shown in Figure 1.18(a) and (b) reveal that NbMoTaW and NbMoTaWV alloys have lower yield strength values of 561 MPa and 862 MPa, respectively, at 873 K, and 405 MPa and 477 MPa, respectively, at 1873 K due to the microstructural deformations of both alloys. Both alloys exhibit higher yield strength than Inconel 718 [69] and Haynes 230 [70], which are (Cr, Ni)-based, high-strength, and corrosion-resistant superalloys, at a temperature range of 1073 K-1873 K [66]. Figure 1.19 shows the engineering stress-strain curves of NbMoTaW, NbMoTaWV, Inconel 718, and Haynes 230 alloys.

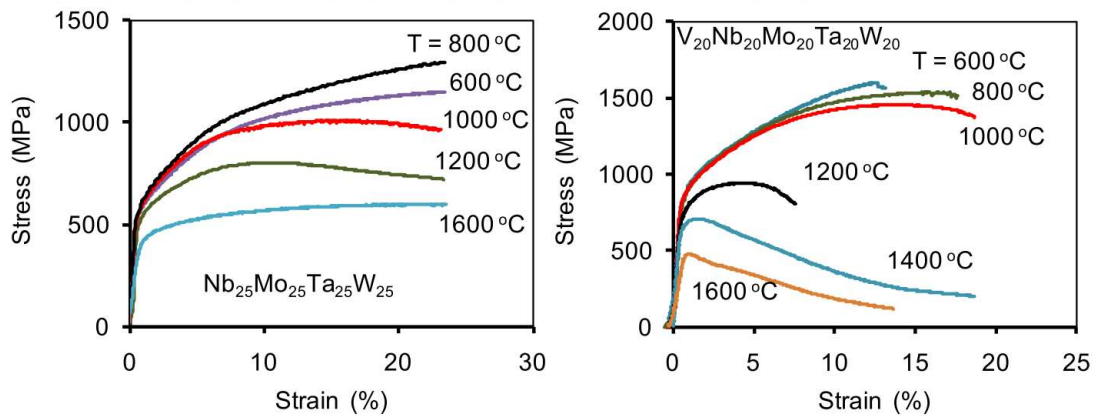


Figure 1. 18. Compressive engineering stress-strain curves of (a) $Nb_{25}Mo_{25}Ta_{25}W_{25}$ and (b) $V_{20}Nb_{20}Mo_{20}Ta_{20}W_{20}$ alloys at elevated temperatures [68].

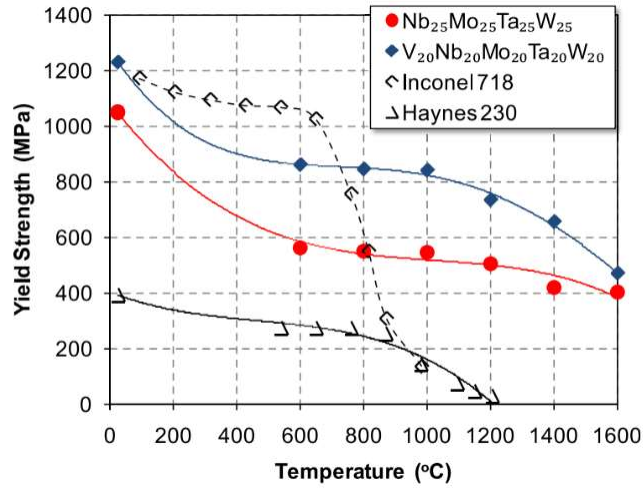


Figure 1. 19. The temperature dependence of yield strength of Nb₂₅Mo₂₅Ta₂₅W₂₅ and V₂₀Nb₂₀Mo₂₀Ta₂₀W₂₀ RHEAs and two superalloys; Inconel 718 and Haynes 230 [68].

The alloying elements also effect the mechanical performance of RHEAs at high temperatures. Wang et al. [71] showed that the additions of Mo and Mo-W elements to single BCC phase HfNbTaTiZr alloy improve the high-temperature yield strength and the softening resistance of the alloy. The W and Mo+W additions provide a strong solid solution strengthening and phase stability in RHEAs. Table 1.5 lists the yield strength values of HfNbTaTiZr, HfNbTaTiZrW, and HfNbTaTiZrMoW alloys depend at different heat treatment conditions.

Table 1. 5. Yield strength values of RHEAs at different heat treatment conditions [71].

Alloys	σ_y (MPa)			
	RT	1073 K	1273 K	1473 K
HfNbTaTiZr	929	535	295	92
HfNbTaTiZrW	1550	577	409	345
HfNbTaTiZrMoW	1637	1065	736	703

1.7.2. Oxidation Behavior of Refractory High Entropy Alloys

The oxidation behavior of RHEAs depends on temperature, processing time, and alloying elements. The oxidation resistance mechanism of alloys is defined with the formation of oxide scales, such as TiO₂, Al₂O₃, ZrO₂, MoO₃, and their protective levels. Oxide scales formations are led by some alloying elements such as Al, Cr, Mo,

Ti, Hf, and W elements. Some of them are resourceful at oxidation resistance improvements, while others cause faster oxidation. Cao et al. [72] proposed that Al decreases the oxidation rate while Mo element increases the oxidation speed of TiNbTa_{0.5}Zr, TiNbTa_{0.5}ZrAl, and TiNbTa_{0.5}ZrAlMo_{0.5} RHEA systems that have dual BCC phases. The protective alumina scale, Al₂O₃, was obtained in TiNbTa_{0.5}ZrAl alloy after the isothermal oxidation tests applied at 1273 K. Thus, the average oxidation rate (k) of alloy in 5 hours decreases from 5.2 mg/(cm².h) to 0.46 mg/(cm².h) in next 35 hours. On the other hand, MoO₃ was detected in TiNbTa_{0.5}ZrAlMo_{0.5}, MoO₃ that weakened the Al₂O₃ scale. It was reported that the addition of Mo causes pores and cracks and thus leads to faster oxidation. Figure 1.20 (a) shows the XRD patterns of RHEAs that were oxidized at 1273 K for 10 hours. Figure 1.20 (b) presents the isothermal oxidation curves of each alloy measured by mass gain per time.

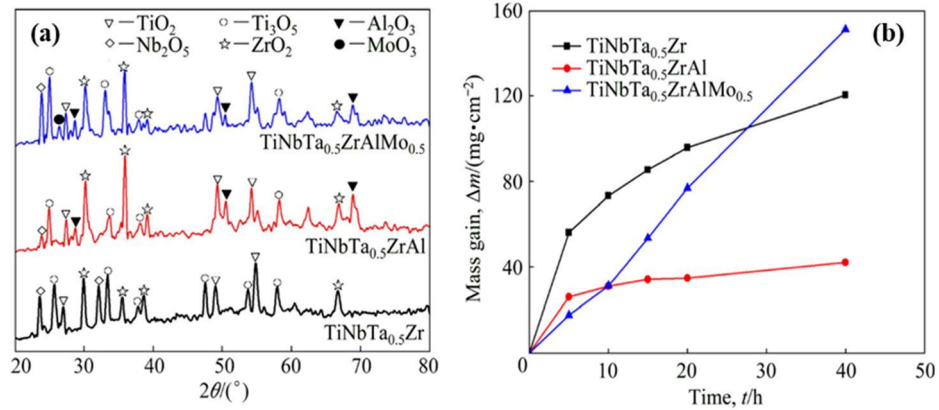


Figure 1. 20. (a) XRD patterns of RHEAs oxidized at 1273 K for 10h and (b) isothermal oxidation curves RHEAs at 1273 K [72].

Gorr et al. [65] presented the Ta addition in X-Mo-Cr-Ti-Al alloy (X=W, Nb, Ta) results in a significant increase in oxidation resistance compared to Nb and W additions at 1273 K. However, it is observed that Nb-Mo-Cr-Ti-Al alloy had a great potential to form the Alumina scale (Al₂O₃) after 24 and 48 hours at 1273 K, even though it has less oxidation resistance than Ta-Mo-Cr-Ti-Al alloy. They also mentioned that W-Mo-Cr-Ti-Al alloy has the lowest oxidation resistance due to the formation of Al₂(WO₄)₃, which occurred by an unfavorable reaction of Al₂O₃ and WO₃ oxides after 24 and 48 hours of oxidation test at 1273 K.

1.7.3. Application Areas of Refractory High Entropy Alloys

RHEAs have a great potential for wide application areas due to their excellent mechanical properties, oxidation behavior, and wear behavior in aerospace propulsion systems, heat exchanger tubes, nuclear reactors, and the chemical process industry [19-20, 25, 66]. Among these areas, the aerospace industry is on the main spot. One of the primary requirements of the aerospace industry is to have lightweight materials with high-temperature resistance against harsh environmental conditions. Therefore much effort has been given have to improve low density and high strength RHEAs to surpass Ni-based superalloys used in turbine blades and combustion chambers of aerospace gas turbine engines [19]. Figure 1.21 exhibits the cut section of a gas turbine engine [74]. For this purpose, Nb, Mo, Ti, and V elements are the most preferable refractory metals with their low densities 8.57 g.cm^{-3} , 10.28 g.cm^{-3} , 4.51 g.cm^{-3} , and 6.11 g.cm^{-3} , respectively, during the design of RHEAs [13, 66, 75]. W is an exception between these refractory metals even though it has a comparably higher density ($16,69 \text{ g.cm}^{-3}$), and it is used for nozzles of some different missiles, rockets, and satellites [66]. Li et al. [73] presented that single BCC phase W_xNbMoTa RHEAs ($x=0.16, 0.33, 0.53$) show better mechanical properties, such as high HV and yield strength values compared to that of conventional refractory alloys such as T-111 (Ta-8%W-2%Hf), C103 (89%Nb-10%Hf-1%Ti), and Nb-1Zr alloys that are dominantly used in aerospace applications [66].

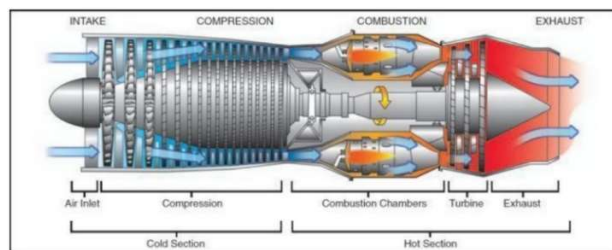


Figure 1. 21. Cut section of a gas turbine engine [74].

Moreover, RHEAs can be more suitable for next generation nuclear reactors. Kareer et al. [65] suggested that neutron activation of elements is an essential requirement to reduce radioactive waste occurring in fusion applications. Therefore, Cr or Zr elements having low neutron activation can be preferred to decrease the high level of nuclear waste instead of mostly used Nb or Mo elements that have higher neutron activation in TiVXTa HEA systems.

1.8. Thesis Organization

This thesis divided into four chapters. The first chapter is the general “Introduction” including introduction and literature review. The second chapter is the “Experimental Procedure” including the production and the characterization of alloys. This chapter gives the details of alloy production using the vacuum arc melting method, heat treatment procedure and the characterization techniques including X-ray diffraction (XRD), in-situ XRD, optic microscope (OM) and scanning electron microscope (SEM), hardness, compression and tension tests. The third chapter is the “Results and Discussion” chapter including the results and the discussion of these results. The fourth chapter is the “Conclusions and Future Predictions” including the summary of the findings in this study and the suggestions for future studies.

CHAPTER II

EXPERIMENTAL PROCEDURE

2.1. Alloy Production

The alloy compositions were determined based on thermodynamic data calculations, including ΔH_{mix} , ΔS_{mix} , δ , and VEC parameters. Table 2.1 and Table 2.2 tabulate the nominal compositions of these selected alloy systems.

Table 2. 1. Nominal compositions Al-Co-Cr-Fe-Ni (Nb-Ti) based alloys.

Alloy	Al	Co	Cr	Fe	Ni	Nb	Ti
RA01	8.00	30.00	18.00	9.00	31.00	4.00	-
RA02	8.00	30.00	18.00	9.00	31.00	2.00	2.00
RA08	8.00	30.00	18.00	9.00	25.00	5.00	5.00
RA10	14.29	14.29	14.29	14.29	14.29	14.29	14.29
RA14	8.00	30.00	18.00	9.00	31.00	-	4.00

Table 2. 2. Nominal compositions of Al-Hf-Mo-Nb-Ta-Ti (V) based alloys.

Alloy	Al	Hf	Mo	Nb	Ta	Ti	V
RA20	16.67	16.67	16.67	16.67	16.67	16.67	-
RA23	14.29	14.29	14.29	14.29	14.29	14.29	14.29

The alloy ingots with nominal compositions of alloys were produced by Edmund Bühler MAM-1 vacuum arc melter with Turbomolecular pumping system HVT52/G, as seen in Figure 2.1 (a, b) using high purity elements (0.999 Al, Co, Cr, Fe, Ni, Nb, Ti, Mo, Hf, Ta, Ti, and V, by weight) under an Ar atmosphere. The alloy ingots with a mass of 3-5 g were cast three times to ensure chemical homogeneity. The alloys were then cast into copper molds, given in Figure 2.1 (c), with diameters of 3 and 4 mm via suction casting for compression and tension tests.

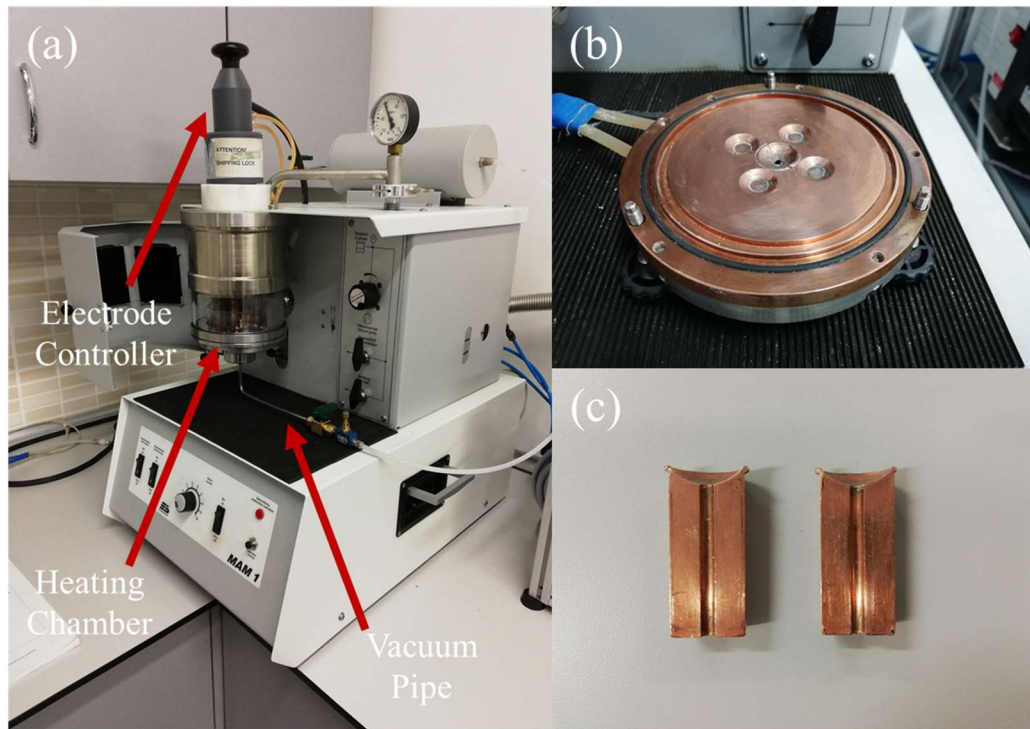


Figure 2. 1. (a) Edmund Bühler MAM 1 vacuum-arc-melting device, (b) copper plate, and (c) copper mold used for vacuum suction casting.

2.2. Heat Treatment of Alloys

The as-cast alloys were heat treated isothermally to investigate their thermal stability. The heat treatment process of alloys was carried out using Protherm PLF Series Chamber Furnace, shown in Figure 2.2. (a) and (b). The as-cast RA01, RA08, RA10, and RA14 alloys were continuously heated up to 1073 K (800 °C) and 1273 K (1000 °C) with a 10 K/min heating rate, kept isothermally at corresponding temperature for 24 hours and then furnace cooled.

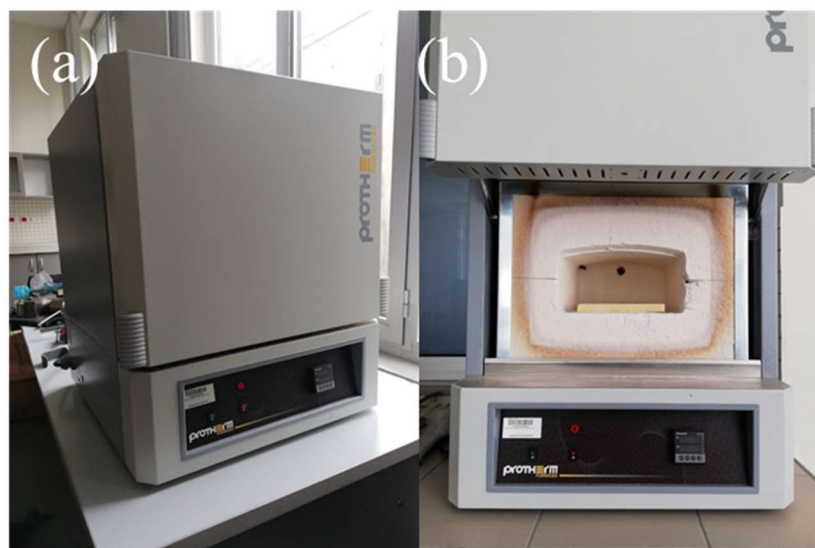


Figure 2. 2. (a) Protherm PLF Series Chamber Furnace and (b) inside the furnace.

2.3. Characterization

2.3.1. X-Ray Diffraction Analysis

The structural analysis and phase stability of the as-cast and heat-treated alloys were investigated by XRD analysis using D8 Advance Bruker X-ray Diffractometer, as seen in Figure 2.3 (a). XRD analysis was carried out using Cu-K α radiation ($\lambda=1.5406 \text{ \AA}$) with the tube voltage of 40 kV and a current of 30 mA. The diffraction data were collected in a diffraction angle range from 10° to 100° with a scanning rate of $2^\circ/\text{min}$. XRD analysis was carried out on the bulk and powder form of rod specimens. The specimens were initially ground to remove any oxide layer on the surface. The thermal stability of the structure of the alloys was investigated using in situ high-temperature XRD. The rod specimens were prepared in powder form using SPEX SamplePrep 8000M Mixer/Mill device, shown in Figure 2.4 for in-situ high-temperature XRD analysis. The powder specimens were heated up to 1373 K with a heating rate of $300^\circ\text{C}/\text{min}$ in the furnace inserted in in-situ XRD equipment. The XRD data were collected in a diffraction angle range from 10° to 100° with a scanning rate with 1K/min scanning rate. The XRD data were collected at 298 K, 773 K, 873 K, 973 K, 1073 K, 1173 K, 1273 K, and 1373 K during heating and after quenching to room temperature.

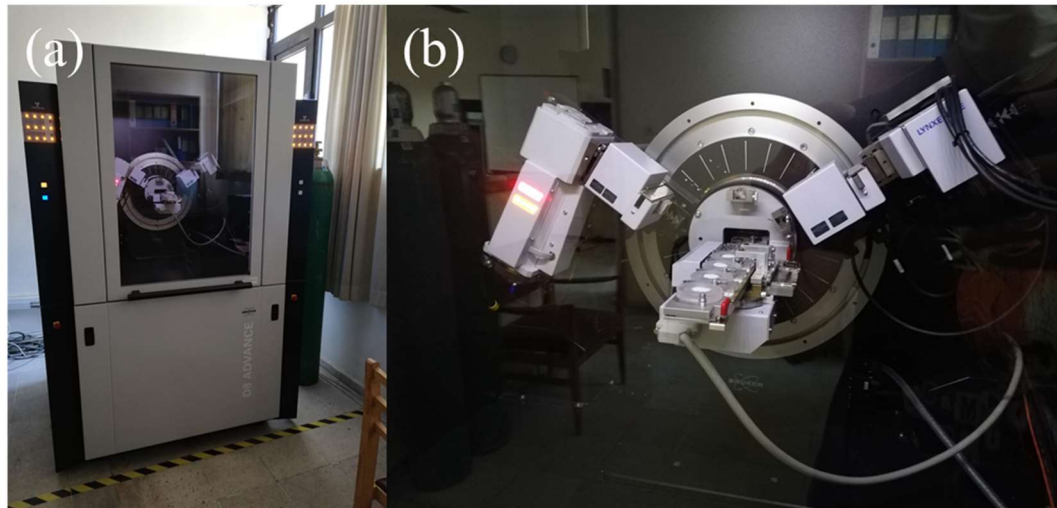


Figure 2. 3. (a) D8 Advance Bruker X-ray Diffractometer, and (b) X-ray tube, detector, and specimen holders.



Figure 2. 4. SPEX SamplePrep 8000M Mixer/Mill ball milling device.

2.3.2. Optical and Scanning Electron Microscopy (SEM) Analysis

The microstructure of as-cast alloys, heat-treated alloys, and fractured surfaces of alloys were investigated using OM and SEM analysis. The OM and SEM analysis were performed using Nikon Eclipse LV150 digital camera optical microscope, seen in Figure 2.5 (a), and FEI Nova NanoSEM 430 Scanning electron microscope, given in Figure 2.5 (b), respectively. The elemental and element distribution analysis were carried out using Energy-dispersive X-ray Spectroscopy detector (EDS) inserted in FEI Nova NanoSEM 430 scanning electron microscope. The OM and SEM specimens were initially ground using 400, 600, 800, 1000, 1200, and 2500 grit sized SiC papers and then polished with 6 μm Alumina solution. The RA01, RA02, RA08, RA10, RA14

alloys were etched using aqua regia ($3\text{HCl}:\text{HNO}_3$) acid solution, and RA20 and RA23 were etched using $\text{HF}:\text{HNO}_3:8\text{H}_2\text{O}$ acid solution.

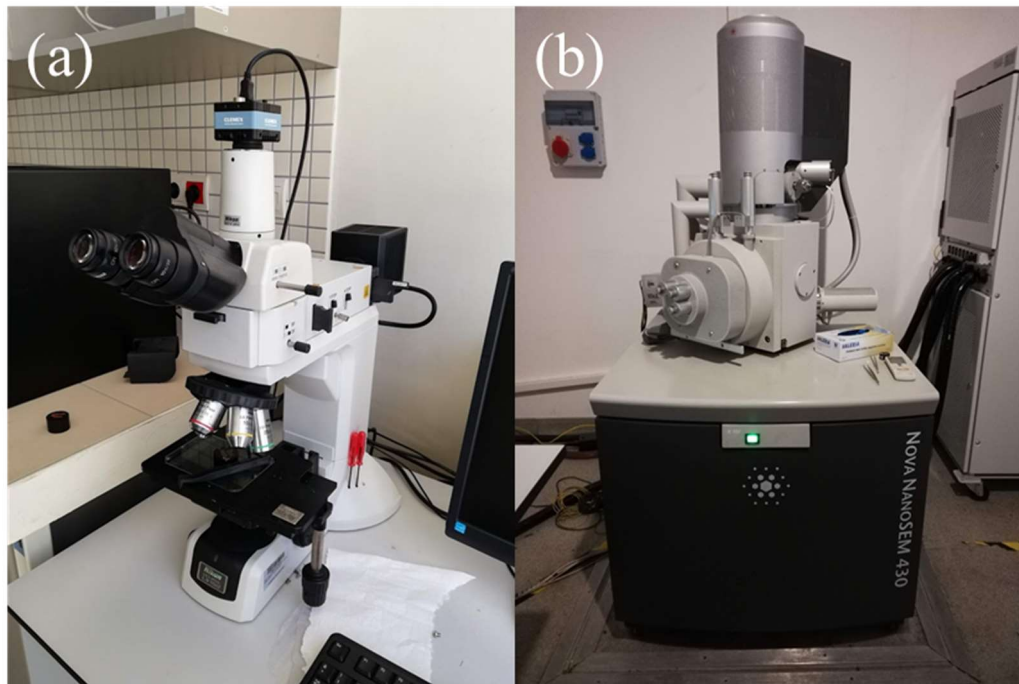


Figure 2. 5. (a) Nikon Eclipse LV150N optic microscope, and (b) FEI Nova NanoSEM 430 scanning electron microscope.

2.4. Mechanical Tests

The mechanical properties of the as-cast and heat-treated alloys were investigated using hardness, compression and tension tests. The hardness tests were performed using INNOVATEST Nexus 7500TM Universal Hardness Tester shown in Figure 2.6. The Vickers micro-hardness tests due to ASTM standard E92 were carried out using a test load of 1 kgf for RA20 and RA23 alloys and 10 kgf for RA01, RA02, RA08, RA10, and RA14 alloys. At least 10 indentation measurements were taken for each specimen, and then the average Vickers Hardness (HV) values with standard deviations were calculated. The HV values were also converted into MPa by multiplying by 9.807 for convenience.



Figure 2. 6. INNOVATEST Nexus 7500TM Universal hardness tester.

The compression test specimens of as-cast RA01, RA08, and RA14 HEAs were prepared due to ASTM E9-19 standard using Instron 5582 universal testing machine, as shown in Figure 2.8 (a) and (b). The specimens were adjusted to the gauge dimensions of ~3 mm in diameter and ~6 mm in height to achieve an aspect ratio of 2:1. The test specimens were precisely cut into 5-6 mm by Buehler branded IsoMet 5000 Linear Precision Saw device, as shown in Figure 2.7, and ground to obtain parallel surfaces. The compression tests were performed on three specimens for each alloy to obtain average compressive properties. Compression tests were done with a strain rate of 10^{-4} . The tensile tests were performed on RA01 and RA14 alloys. The test specimens with the gauge dimensions of 4 mm in diameter and 16 mm in height were prepared according to ASTM E8/E8M standard. Two specimens were prepared for each alloy, and average tensile properties were determined. Tension tests were operated with a crosshead speed of 1 mm/min. The fracture surfaces of specimens were then investigated using FEI Nova NanoSEM 430 scanning electron microscope shown in Figure 2.5 (c).



Figure 2. 7. Buehler IsoMet 5000 Linear Precision Saw device.

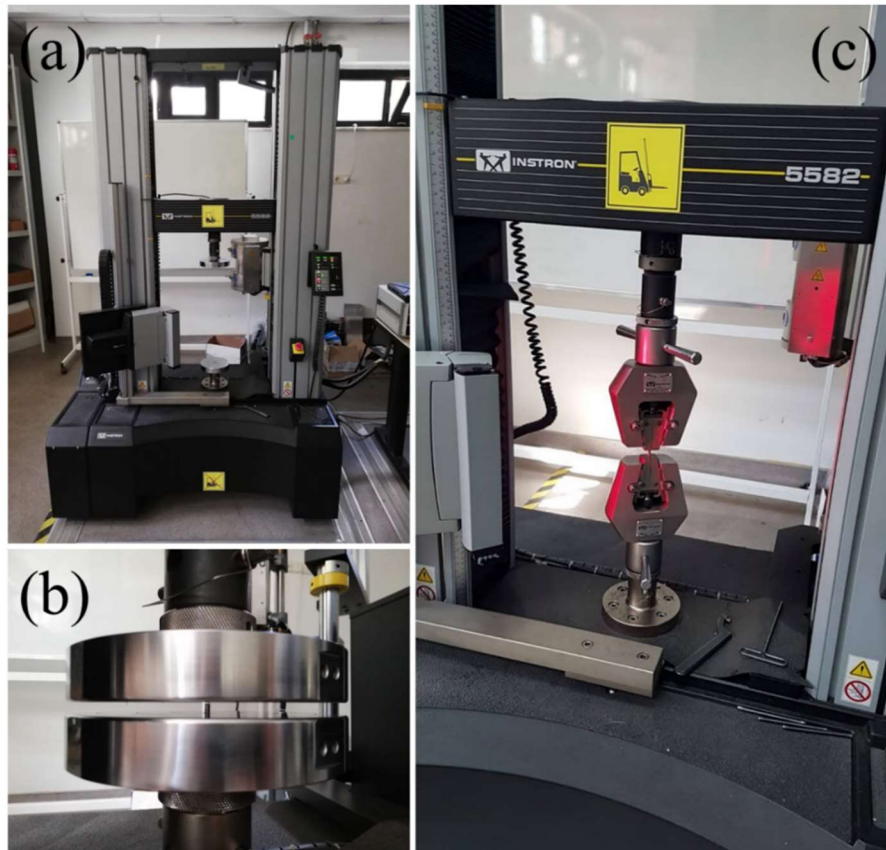


Figure 2. 8. (a) Instron 5582 mechanical testing machine with (b) compression apparatus holding 3 mm specimen, and (c) tensile apparatus holding 4 mm specimens.

CHAPTER III

RESULTS AND DISCUSSION

3.1. Thermodynamic Calculations of High Entropy Alloys

The calculated thermodynamic parameters; ΔH_{mix} , ΔS_{mix} , VEC, and atomic size differences (δ) of equiatomic and nonequiatomic Al-Co-Cr-Fe-(Ni-Nb-Ti) alloys were tabulated in Table 3.1. It was observed that the variation of Ni, Nb, and Ti concentrations of the alloys effect the thermodynamical parameters of the high entropy alloys. For instance, while all other nonequiatomic HEA alloys given in Table 3.1 have average negative ΔH_{mix} values, equiatomic RA10 alloy has the largest negative ΔH_{mix} . This ΔH_{mix} value is mainly caused by the significant decrease in Co, Ni, and increase in Al, Fe, Nb, and Ti concentrations in the alloy. It was also expected that possible intermetallic phases could form in the alloy due to the high ΔH_{mix} . The expected crystal structures based on the calculated VEC values are single FCC for RA01 (31% Ni – 4% Nb), RA02 (31% Ni – 2% Nb – 2% Ti), and RA14 (31% Ni – 4% Ti) HEAs, both FCC and BCC for RA08 HEA and a single BCC for equiatomic RA10 HEA. The structure change is mainly due to the atomic size differences between constituent elements. Table 3.2 gives the list of atomic radius values of the constituent elements of the studied alloys.

Table 3. 1. Thermodynamical data of alloys.

Alloy	ΔH_{mix} (kJmol ⁻¹)	ΔS_{mix} (JK ⁻¹ mol ⁻¹)	ΔS_{mix}	VEC	δ	Expected Crystal Structure
RA01	-11.11	13.14	1.58R	8.04	4.69	FCC
RA02	-11.59	13.37	1.60R	8.02	4.83	FCC
RA08	-15.74	14.42	1.73R	7.69	5.75	FCC+BCC
RA10	-25.88	16.18	1.94R	6.43	7.25	BCC
RA14	-11.75	13.14	1.58R	8	4.98	FCC

Table 3. 2. Atomic radii of constituent elements of the alloys.

Element	Atomic Radius (nm)
Al	0.14317 [12]
Co	0.12510 [12]
Cr	0.12491 [12]
Fe	0.12412 [12]
Ni	0.12459 [12]
Nb	0.14290 [12]
Ti	0.14615 [12]

3.2. Characterization of As-Cast High Entropy Alloys

3.2.1. X-Ray Diffraction Analysis

Figure 3.1 displays the XRD patterns of as-cast Al-Co-Cr-Fe-(Ni-Nb-Ti) alloys. XRD pattern of as-cast nonequiatomic RA01 alloy shows the FCC phase as expected from its VEC calculations. The overlapped main peaks of the Ni₃Al phase were also observed for RA01 alloy due to the XRD analysis. The lattice parameter of the FCC phase in the RA01 alloy was determined as 0.3592 nm, based on the interplanar spacing of peaks from the XRD pattern. Ni₃Al is an intermetallic L₁₂ phase having an ordered FCC crystal structure, and the formation can be interpreted by the Al and Nb contents, which are the most L₁₂ stabilizers in alloy [22]. The lattice parameter of the

Ni₃Al phase in the RA01 alloy was determined as 0.3590 nm. The as-cast nonequiatomic RA02 alloy is composed of FCC phase as expected from its VEC calculations, but RA02 alloy has the strongest Ni₃Al peaks, which are overlapped with FCC peaks, as well. The corresponding lattice parameters of FCC and Ni₃Al phases in the RA02 alloy were determined as 0.3597 nm and 0.3592 nm, respectively. Co and Ni are the FCC stabilizers, so their high concentrations promote the formation of the FCC phase. On the other hand, lower concentrations of Al and Fe promotes the BCC phase formation. The XRD pattern of RA08 alloy indicates FCC + BCC double phase formation as expected from the VEC calculations. The additional peaks corresponding to the intermetallic phases were also observed. The corresponding lattice parameters of FCC and BCC phases were calculated as 0.3597 nm and 0.3375 nm, respectively. The higher concentration of the Ti element compared to RA01 and RA02 alloys results in the formation of an ordered FCC Ni₃Ti phase. The formation of intermetallic Ni₃Ti phase is due to the high-negative ΔH_{mix} value of the atomic bonding pair between Ni and Ti elements. Table 3.3 tabulates the ΔH_{mix} values of elements. The ΔH_{mix} value between Ni and Ti elements is -34.5 kJmol^{-1} from Table 3.3, which indicates they have the weakest bonding interaction between each other compared to the other atom pairs. Therefore, Ni and Ti are more likely to form an intermetallic phase in RA08 alloy. Moreover, from the XRD pattern of RA08 alloy, Laves phase reflection was also observed. The XRD pattern of as-cast equiatomic RA10 alloy shows the mixed FCC and BCC phases and additional Laves and B2 reflections. The lattice parameters of FCC, BCC, and B2 phases were determined as 0.3587, 0.3396, and 0.3329 nm, respectively. Even though the VEC calculations indicate a single BCC crystal structure, the XRD analysis indicates multiphase formation. It also reveals that the VEC number is not the only criterion to guess the final phase formation. The variation of elements and their concentrations play a significant role in the intermetallic phase formation in high entropy alloys. RA10 alloy has the highest Nb and Ti concentrations amongst other alloys. Nb and Ti are poorly compatible with other transition metals, Al, Co, Cr, Fe, and Ni. Therefore, their atomic size differences promote the formation of intermetallic phases. The XRD pattern of RA14 alloy indicates nice FCC reflections, which has a lattice parameter of 0.3589 nm. The XRD fitting analysis also reveals the reflections of tetrataenite FeNi phase overlapped with FCC peaks. The

lattice parameter of FeNi was calculated as 0.3587 nm. The tetragonal FeNi is an L1₀ type metallic phase, which is an essential magnetic phase in Fe-Ni based alloys [76].

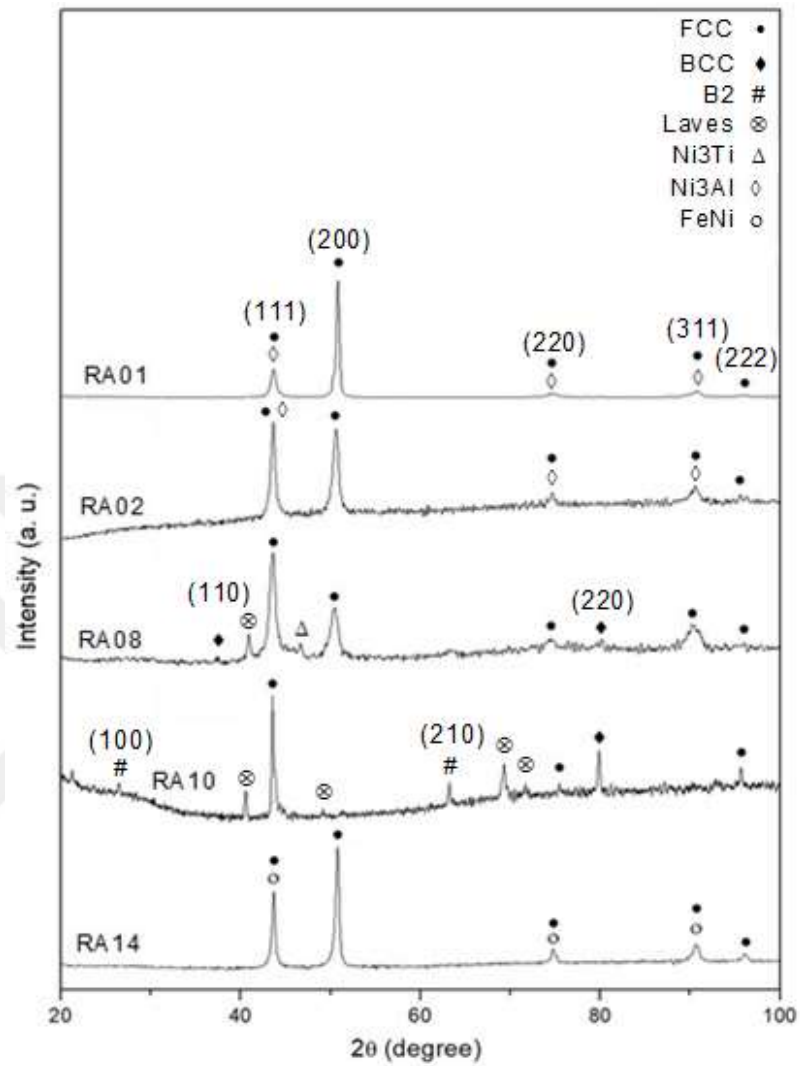


Figure 3. 1. XRD patterns of as-cast HEAs.

Table 3. 3. ΔH_{mix} values of elements in $\text{kJ}\cdot\text{mol}^{-1}$ [77].

Al	Co	Cr	Fe	Ni	Nb	Ti	
	-18.8	-9.9	-11.1	-22.3	-18.2	-29.5	Al
		-4.5	-0.6	-0.2	-24.5	-28.3	Co
			-1.5	-6.7	-7.2	-7.5	Cr
				-1.6	-15.7	-16.8	Fe
					-29.9	-34.5	Ni
						2.0	Nb
							Ti

3.2.2. Microstructure Analysis

The microstructure of as-cast and heat-treated alloys were investigated using OM and SEM. Figure 3.2 shows the SEM images of as-cast Al-Co-Cr-Fe-(Ni-Nb-Ti) alloys at different magnifications. SEM micrographs of all alloys exhibited dendritic and interdendritic structures. Figure 3.2 (a, b) illustrates the SEM images of RA01 alloy. The micrograph shows the precipitates between dendrites. These precipitates were defined as Ni_3Al from the XRD analysis. SEM images in Figure 3.2 (c, d) show more dense dendritic structure formation in RA02 due to 2 at.% decrease in Nb, and 2 at.% addition of Ti element. SEM images of RA08 in Figure 3.2 (e, f) illustrate the more dispersed (less equiaxed) dendritic structure and precipitates. It can be interpreted that the precipitates were formed due to the formation of intermetallic phases depending on the decrease in Ni, and increase in both Nb and Ti concentrations. The SEM images of equiatomic RA10 alloy are presented in Figure 3.2 (g, h). RA10 alloy has the most dispersed interdendritic regions due to the intermetallic phase formation supported by XRD analysis. Figure 3.2 (i, j) illustrates the SEM images of RA14 alloy. The micrographs show the equiaxed precipitates embedded in the dendritic matrix. These precipitates are determined as the tetrataenite FeNi phase with tetragonal structure due to XRD analysis.

The elemental analysis of the alloys was also performed. Table 3.4 and Table 3.5 show the EDS analysis of alloys from the whole surface, dendritic, and interdendritic regions. The EDS analysis reveals the accumulation of Nb and Ti elements at interdendritic regions due to their high negative ΔH_{mix} for the alloys except RA10 alloy. Cr and Fe tended to be segregated into dendritic regions in all alloys. According to EDS results, noticeable decreases in Al and Ni, a slight decrease in Fe, and a significant increase in Nb concentrations in interdendritic regions are observed in RA01 alloy. It can be interpreted that precipitates occurred in interdendritic regions are observed due to Nb segregation. In RA08, growth and disarrangement in precipitates can be explained by critical increases in Al, Ni, and Ti elements causing $\text{Ni}_3(\text{Ti}, \text{Al})$ -based Ni_3Ti phase in the interdendritic region. The elemental analysis of RA14 alloy reveals the Al pile up at dendritic regions and minor increases in Ni and Ti at interdendritic regions.

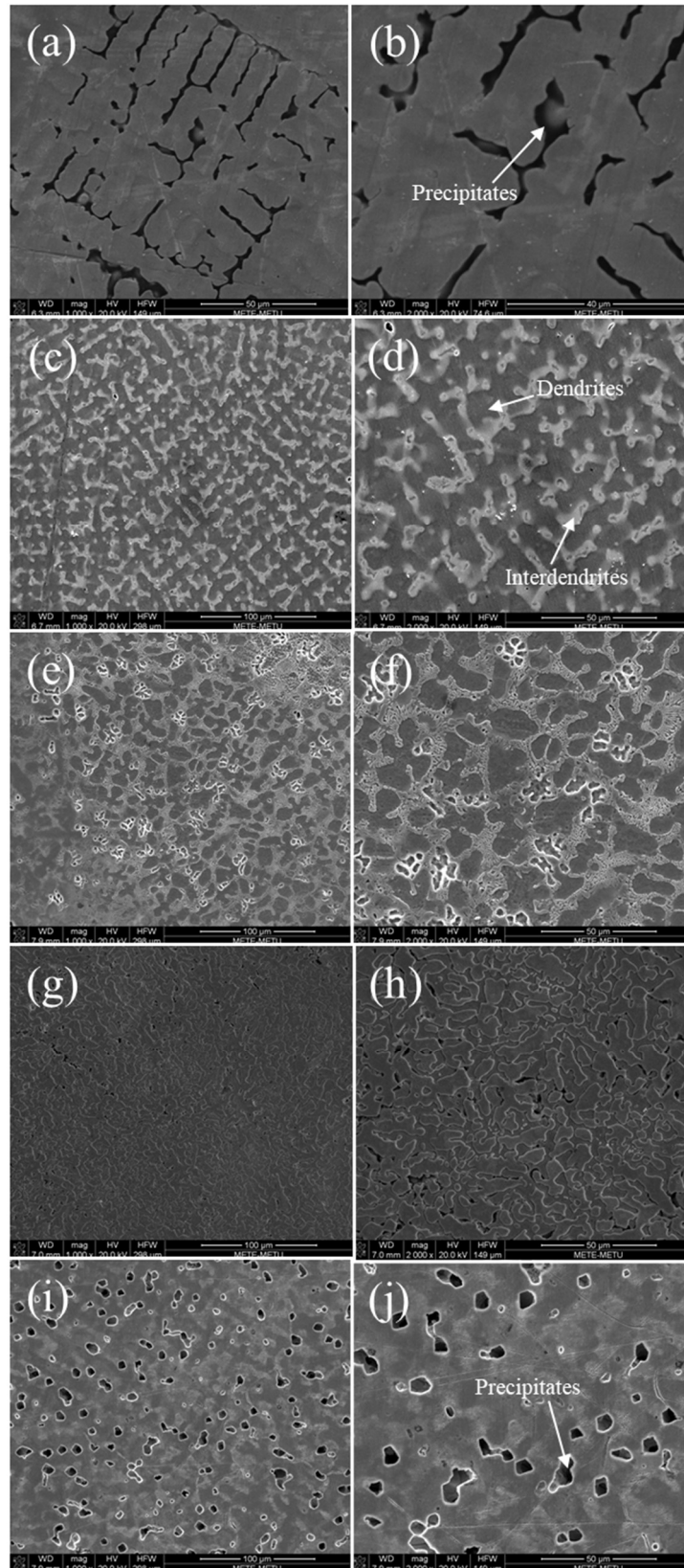


Figure 3. 2. SEM images of as-cast (a) RA01 (1000x), (b) RA01 (2000x), (c) RA02 (1000x), (d) RA02 (2000x), (e) RA08 (1000x), (f) RA08 (2000x), (g) RA10 (1000x), (h) RA10 (2000x), (i) RA14 (1000x), and (j) RA14 (2000x)

Table 3. 4. EDS analysis of alloys in at.%.

	Al	Co	Cr	Fe	Ni	Nb	Ti
RA01	9.14±0.08	29.02±0.23	17.85±0.22	9.09±0.16	30.40±0.13	4.51±0.29	-
RA02	9.01±0.28	30.11±1.14	17.28±0.64	9.07±0.10	30.73±0.05	2.38±0.04	2.06±0.10
RA08	8.23±0.02	29.76±1.07	17.26±0.77	9.11±0.05	25.09±0.28	5.64±0.02	5.00±0.16
RA10	13.73	13.00	15.41	15.68	15.55	12.78	13.85
RA14	7.72±0.10	29.59±0.11	18.15±0.12	9.16±0.04	31.32±0.05	-	4.07±0.37

Table 3. 5. EDS analysis of dendritic (D) and interdendritic (ID) regions of alloys in at.%.

	RA01		RA02		RA08		RA10		RA14	
	D	ID	D	ID	D	ID	D	ID	D	ID
Al	3.19	2.91	4.90	4.18	8.15	15.55	7.86	25.83	7.22	0.57
Co	31.92	32.36	31.81	29.04	30.45	24.92	12.26	17.19	30.89	31.89
Cr	16.86	12.51	18.51	15.26	20.44	9.63	22.18	3.24	18.76	18.46
Fe	8.96	6.82	10.10	7.66	10.65	5.15	19.82	6.73	10.00	8.97
Ni	36.32	26.15	32.69	30.49	24.86	28.36	8.84	24.60	30.45	34.90
Nb	2.77	19.37	0.79	9.71	2.31	5.90	17.31	3.83	-	-
Ti	-	-	1.20	3.67	3.15	10.51	11.73	18.59	2.68	5.23

The EDS elemental distribution maps of alloys are illustrated in Figure 3.3. EDS maps confirm the segregation of Nb and Ti through interdendritic regions, while Cr and Fe pile up at dendritic regions for (a) RA01, (b) RA02, (c) RA08, and (d) RA14 alloys. The accumulate of Ni in the precipitates distributed in the dendritic matrix of RA14 alloy supports the XRD analysis that claims the formation of the tetragonal FeNi phase.

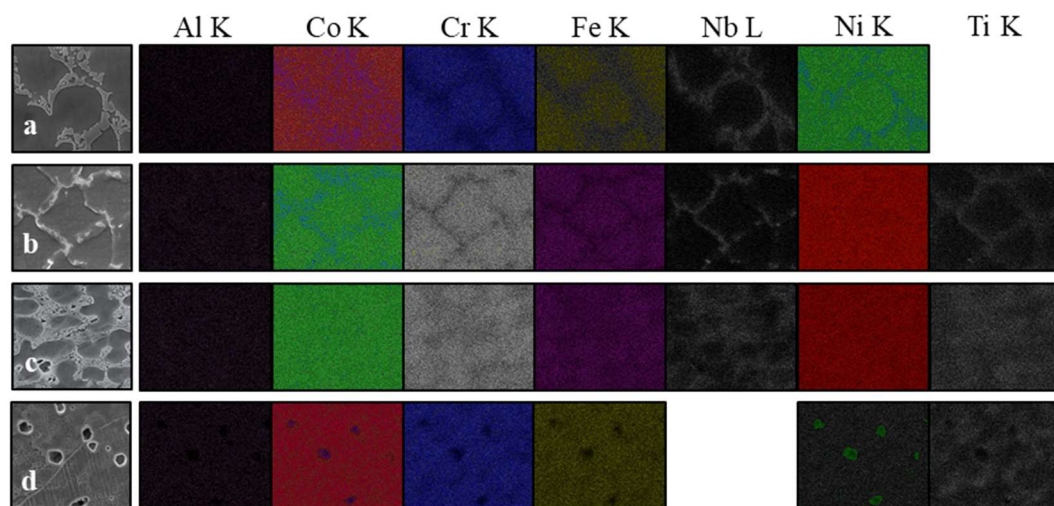


Figure 3. 3. EDS maps according to elemental distributions of (a) RA01, (b) RA02, (c) RA08, (d) RA14 HEAs

3.3. Characterization of Isothermally Heat-Treated High Entropy Alloys

The as-cast alloys were heat-treated to investigate their high-temperature behavior and the effect of heat treatment on their microstructure, phase stability, and mechanical properties. The RA01, RA08, RA10, and RA14 alloys were isothermally annealed at 1073 K (800 °C) and 1273 K (1000 °C) for 24 hours to investigate the precipitation behavior, phase stability, and mechanical properties. The alloys were then cooled to room temperature rapidly. The phase stability and microstructure of isothermally annealed alloys were investigated using XRD and optic microscopy.

3.3.1. RA01 ($\text{Al}_8\text{Co}_{30}\text{Cr}_{18}\text{Fe}_9\text{Ni}_{31}\text{Nb}_4$) Alloy

Figure 3.4 shows the XRD patterns of as-cast and isothermally annealed RA01 alloy at 1073 K, and 1273 K temperatures for 24 hours. XRD patterns indicate that the isothermally annealed RA01 alloy at 1073 K and 1273 K temperatures keep its structure, and it is composed of FCC and Ni_3Al phases. It shows the phase stability of RA01 alloy. Some of the peaks corresponding to FCC and Ni_3Al phases are not observed in the XRD pattern of the isothermally annealed RA01 alloy at 1273 K due to preferred orientation. It is also observed that the FCC peaks are shifting to larger theta values by increasing the isothermal annealing temperature. Thus, the interplanar spacing, d values decrease slightly due to the increase in lattice strain energy and lattice distortion. The heat treatment also affected the lattice parameters. The lattice

parameter of the FCC phase decreases from 0.3592 nm to 0.3578 nm at 24-hours 1073 K HT, and to 0.3552 nm at 24-hours 1273 K HT conditions.

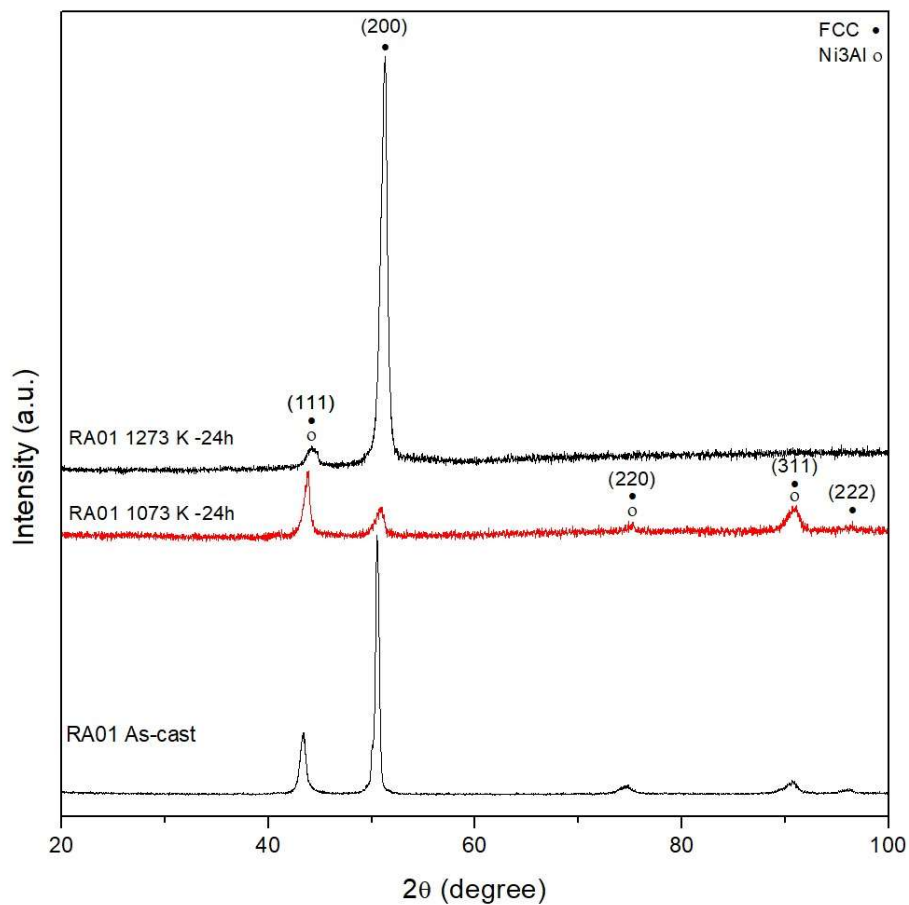


Figure 3. 4. XRD patterns of as-cast RA01 alloy, isothermally annealed RA01 alloy at 1073 K for 24 hours and isothermally annealed RA01 alloy at 1273 K for 24 hours.

The optic microscope (OM) images of as-cast RA01 alloy, isothermally annealed RA01 alloy at 1073 K, and 1273 K are presented in Figures 3.5 (a, b), (c, d) and (e, f), respectively. The microstructures of as-cast and heat-treated alloys exhibit two distinct regions; dendritic (darker regions) and interdendritic (lighter regions). These are typical microstructures of many HEAs. The contrast differences between dendritic and interdendritic regions are due to the difference in chemical compositions. The dendrites become coarser when annealed at 1073 K for 24 hours due to grain growth. The micrographs in Figure 3.5 (e, f) show a finer dendritic structure, which is similar to equiaxed dendrites for isothermally annealed RA01 alloy at 1273 K for 24 hours. It is worth to mention that the dendritic structure will probably transform into equiaxed dendritic grains when longer annealing time at 1273 K is applied.

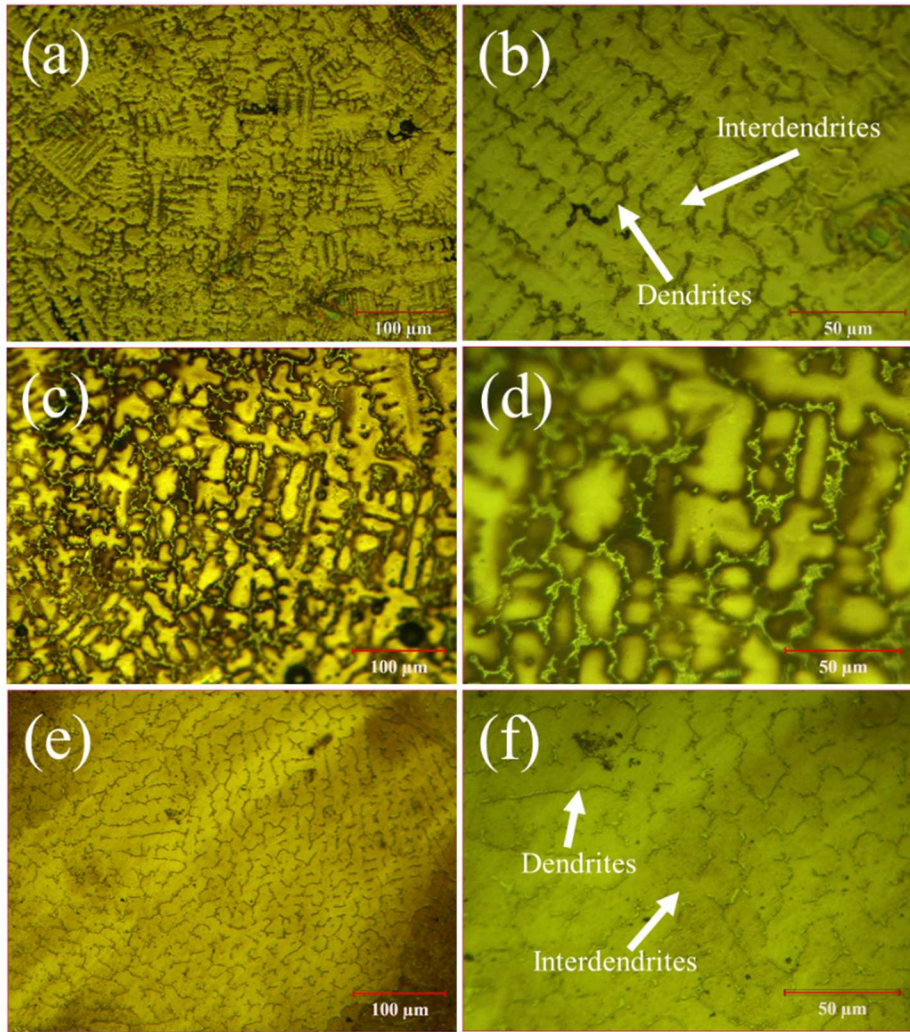


Figure 3. 5. OM images of (a, b) as-cast RA01 alloy, (c, d) isothermally annealed RA01 alloy at 1073 K for 24 hours, and (e, f) isothermally annealed RA01 alloy at 1273 K for 24 hours at different magnifications.

3.3.2. RA08 ($\text{Al}_8\text{Co}_{30}\text{Cr}_{18}\text{Fe}_9\text{Ni}_{25}\text{Nb}_5\text{Ti}_5$) Alloy

Figure 3.6 presents the XRD patterns of as-cast and isothermally annealed RA08 alloy at 1073 K and 1273 K for 24 hours. It is observed that phases remain stable during isothermal annealing. Furthermore, the FCC reflections shift to larger theta by increasing the isothermal annealing temperature. It is seen that the peaks corresponding to the Laves phase become more distinct and sharper for isothermally annealed RA08 alloy at 1273 K. The lattice parameter of the FCC phase decreases from 0.3597 nm (1073 K HT) to 0.3578 nm for 1273 K isothermal annealing condition.

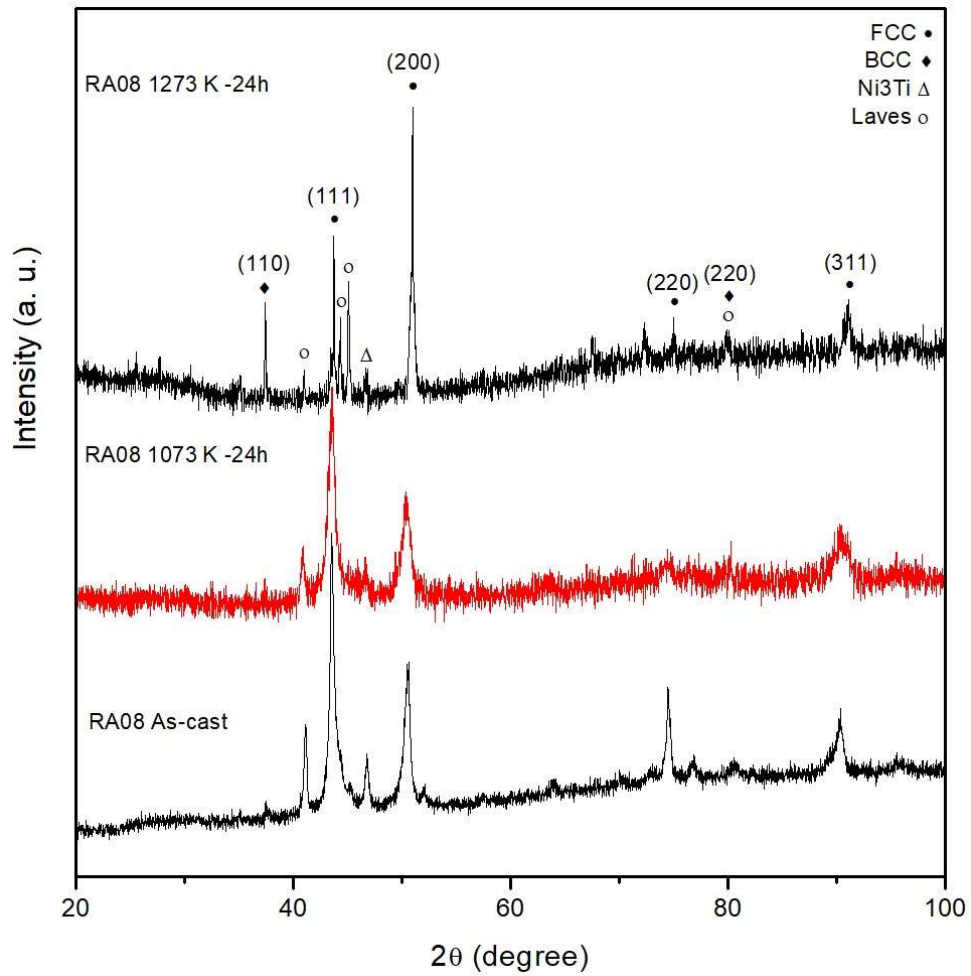


Figure 3. 6. XRD patterns for RA08 HEA isothermally annealed at 1073 K (800 °C) and 1273 K (1000 °C) for 24 hours.

The OM images of as-cast RA08 alloy, isothermally annealed RA08 alloy at 1073 K, and 1273 K are presented in Figure 3.7 (a, b), (c, d) and (e, f), respectively. The microstructures of as-cast and heat-treated alloys exhibit two distinct regions; dendritic (darker regions) and interdendritic (lighter regions). The microstructure of the alloy remains nearly same through the heat treatment process, which shows the phase stability of this alloy.

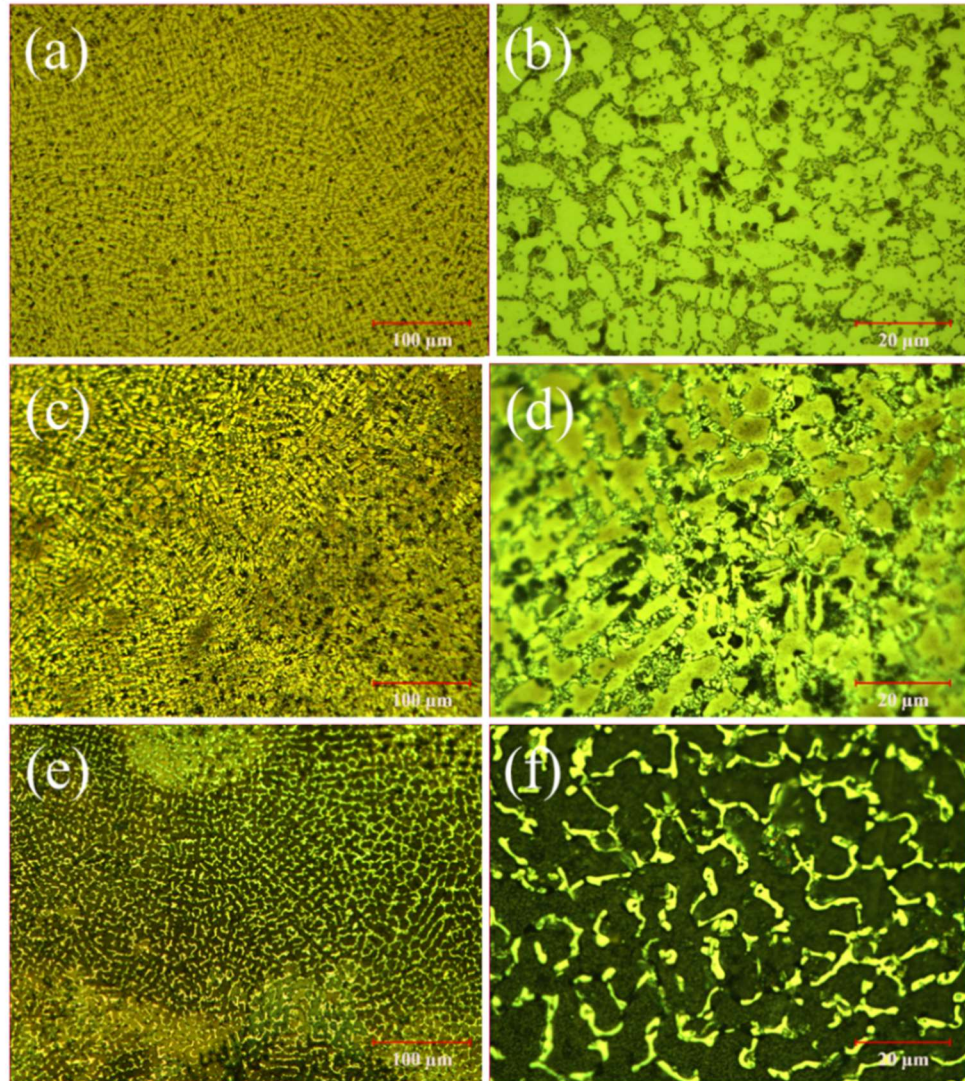


Figure 3. 7. OM images of (a, b) as-cast RA08 alloy, (c, d) isothermally annealed RA08 alloy at 1073 K for 24 hours, and (e, f) isothermally annealed RA08 alloy at 1273 K for 24 hours at different magnifications.

3.3.3. RA10 (AlCoCrFeNiNbTi) Alloy

The XRD patterns of as-cast and isothermally annealed RA10 alloy at 1073 K and 1273 K for 24 hours are illustrated in Figure 3. 8. The phase stability of the RA10 alloy is seen from the XRD analysis. However, at 1273 K-HT condition, additional oxidation peaks are observed. It is mainly caused during the annealing process at the high temperature. The RA10 alloys have B2 and Laves phases. These are the typical intermetallic phases observed in HEAs. The intermetallic phase formation in HEAs is sometimes inevitable, and a new term, high entropy intermetallic compounds (HEIC),

has been introduced to fill the gap between traditional high entropy alloys and emerging (mostly ionic) HEAs. HEIC serves new metallic material of new characteristics of high entropy alloy [78].

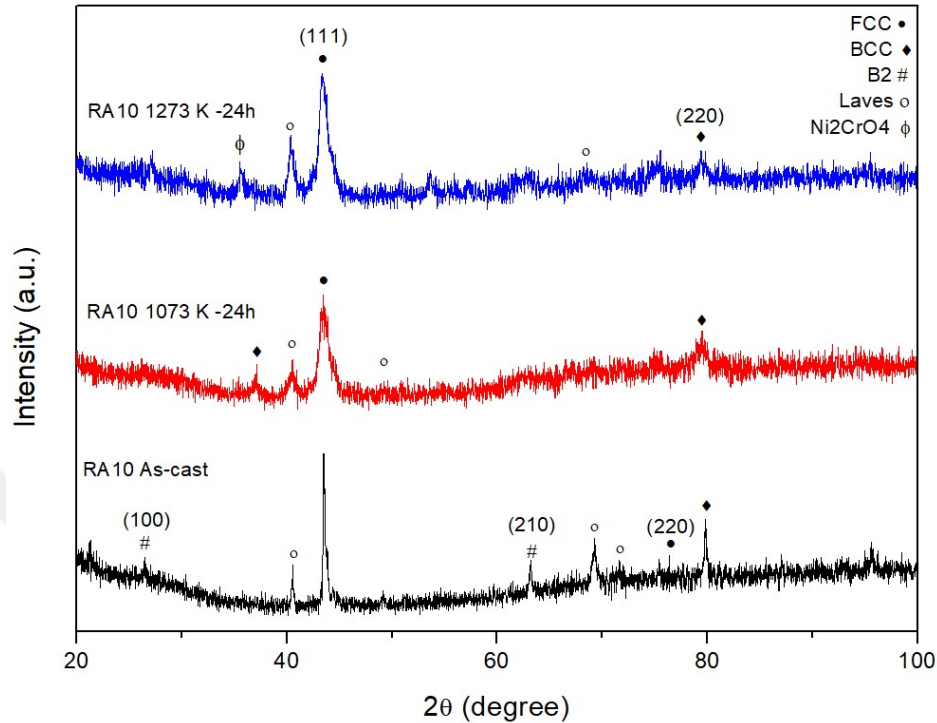


Figure 3. 8. XRD patterns for RA10 HEA isothermally annealed at 1073 K (800 °C) and 1273 K (1000 °C) for 24 hours.

The OM images of as-cast RA10 alloy, isothermally annealed RA10 alloy at 1073 K, and 1273 K are presented in Figure 3.9 (a, b), (c, d) and (e, f), respectively. The micrographs indicate dendritic and interdendritic regions with contrast differences. Furthermore, the microstructure of the alloy remains similar after each annealing step. There is no noticeable change in the structure of dendrites. RA10 alloy has intermetallic phases and strong phase stability. The phase stability is an important advantage for possible applications of this alloy.

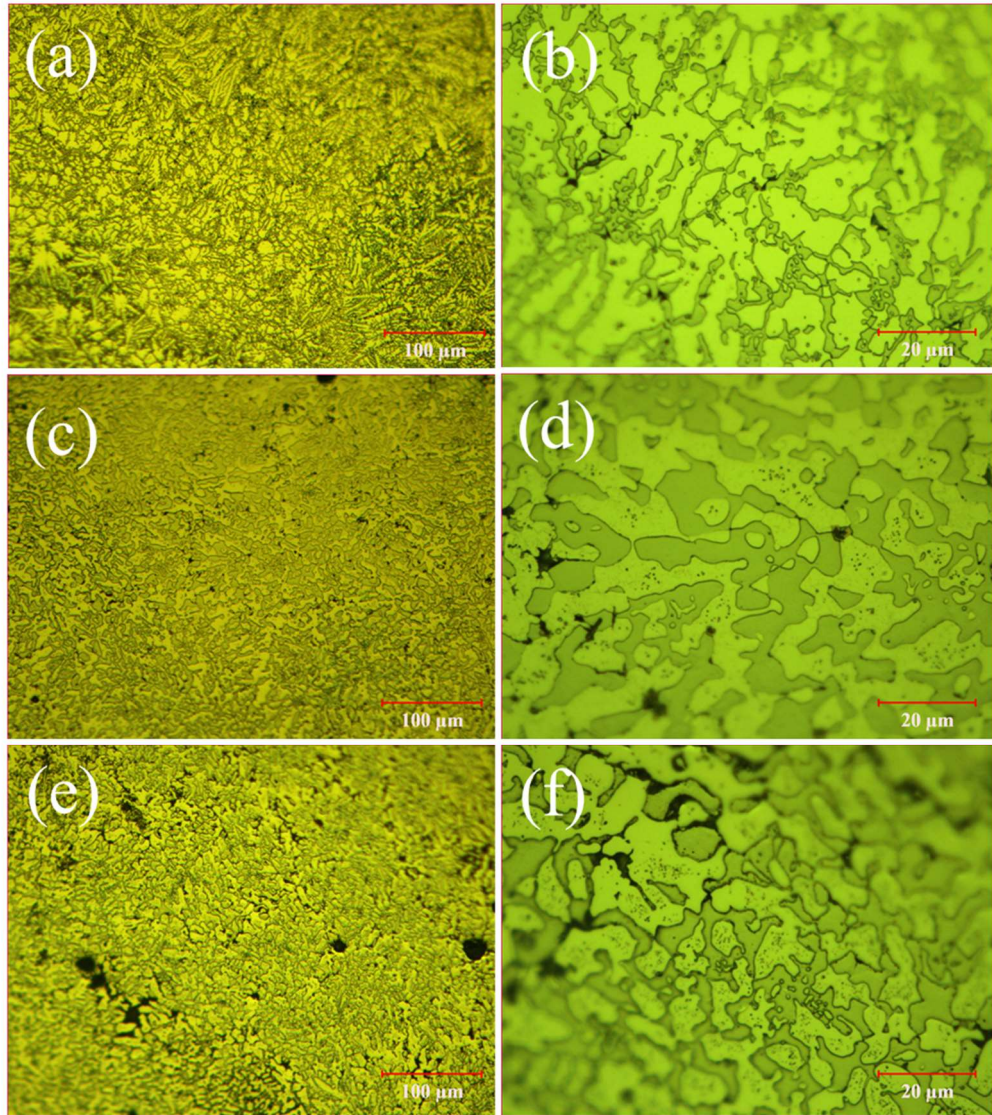


Figure 3. 9. OM images of (a, b) as-cast RA10 alloy, (c, d) isothermally annealed RA10 alloy at 1073 K for 24 hours, and (e, f) isothermally annealed RA10 alloy at 1273 K for 24 hours at different magnifications.

3.3.4. RA14 ($\text{Al}_8\text{Co}_{30}\text{Cr}_{18}\text{Fe}_9\text{Ni}_{31}\text{Ti}_4$) Alloy

Figure 3.10 illustrates the XRD patterns of as-cast and isothermally annealed RA14 alloy at 1073 K and 1273 K for 24 hours. XRD analysis shows the phase stability during isothermal annealing. The lattice parameters of the FCC phase were calculated as 0.3589 nm, 0.3580 nm, and 0.3564 nm for as-cast, 1073 K HT, and 1273 K HT conditions, respectively. The lattice parameter of the FCC phase decreases with annealing. The XRD pattern of isothermally annealed RA14 alloy at 1273 K has additional oxidation peaks, and the reflections were fit as Maghemite-C, Fe_2O_3 phase.

When compared with RA01 alloy, which has 4 at.% Nb, RA14 alloy has weaker oxidation resistance with its 4 at.% Ti content at 1273 K HT condition. It may be concluded that Nb serves better oxidation resistance than Ti at high temperatures.

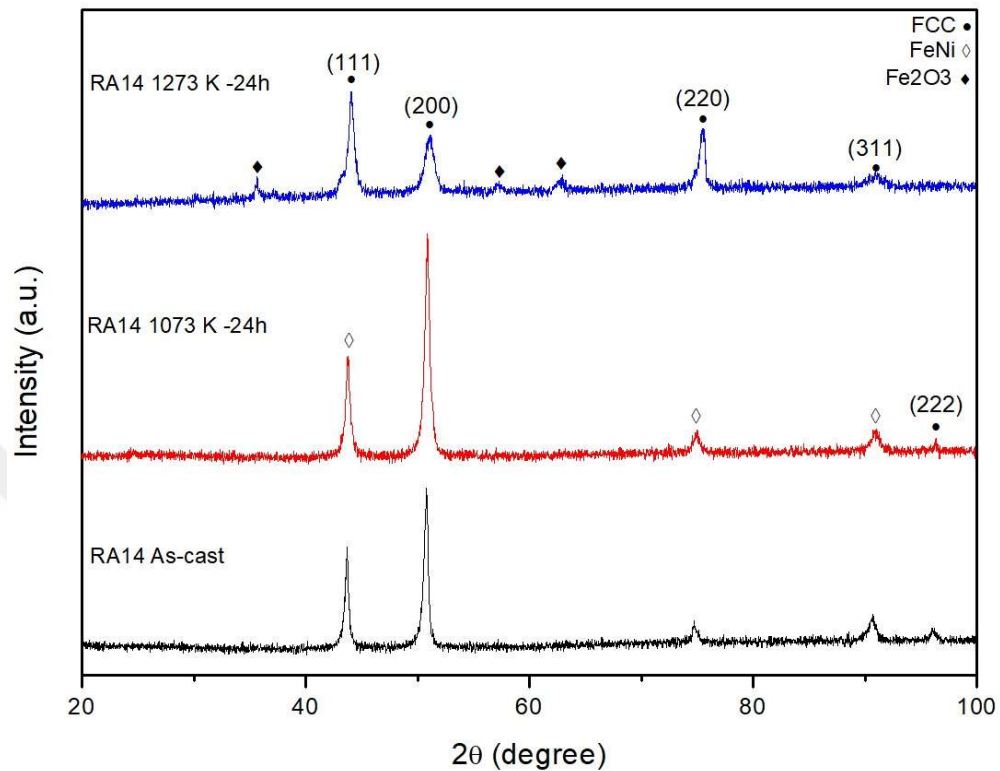


Figure 3. 10. XRD patterns of as-cast RA14 alloy, isothermally annealed RA14 alloy at 1073 K (800 °C) and 1273 K (1000 °C) for 24 hours.

The OM images of as-cast RA14 alloy, isothermally annealed RA14 alloy at 1073 K, and at 1273 K in are presented in Figure 3.11 (a, b), (c, d) and (e, f), respectively. The microstructures of as-cast and heat-treated alloys exhibit dendrite grains and precipitates. These precipitates were determined as FeNi from XRD analysis. The dendritic grains become more equiaxed with annealing. The precipitates become coarser and needle-like with heat treatment and increasing annealing temperature.

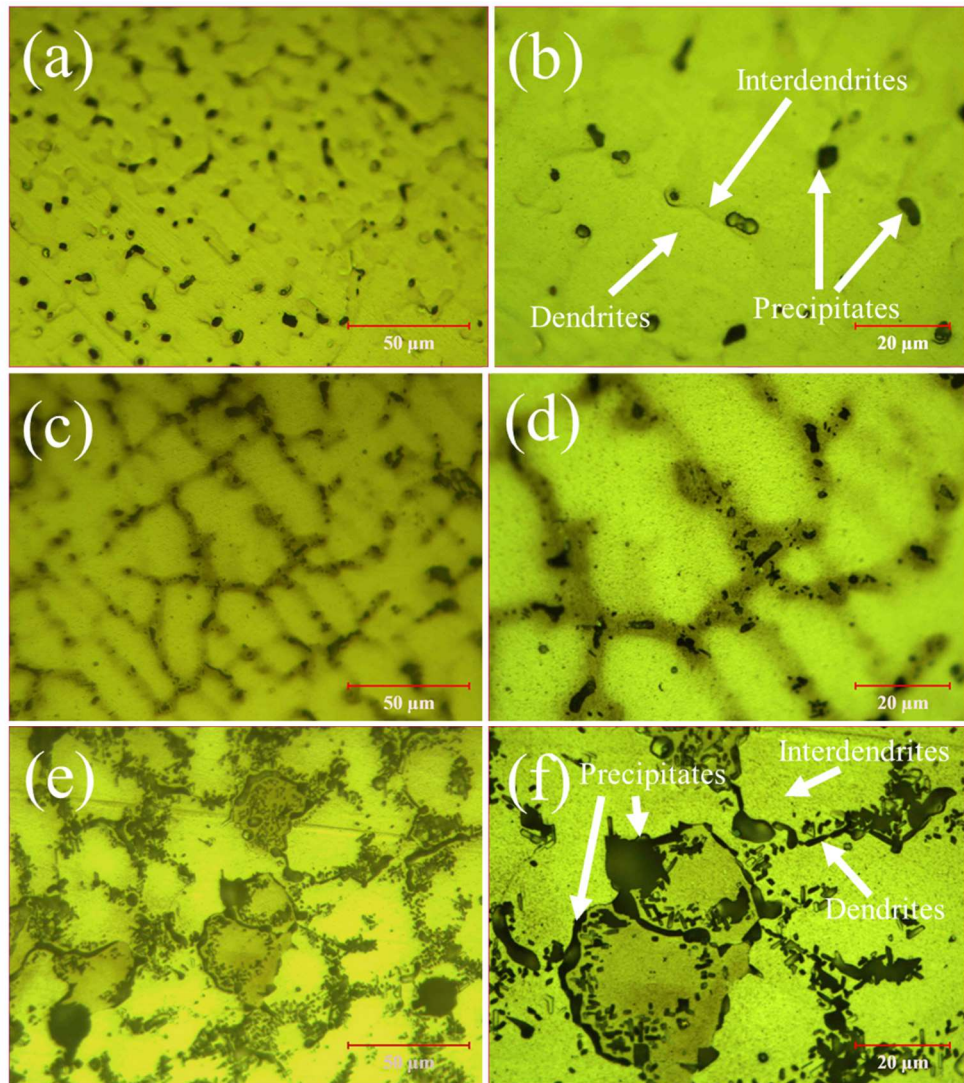


Figure 3. 11. OM images of (a, b) as-cast RA14 alloy, (c, d) isothermally annealed RA14 alloy at 1073 K for 24 hours, and (e, f) isothermally annealed RA14 alloy at 1273 K for 24 hours at different magnifications.

3.4. Characterization of Mechanical Properties of High Entropy Alloys

3.4.1. Hardness Measurements

The microhardness test results of as-cast and heat-treated RA01, RA08, RA10, and RA14 alloys are given in Figure 3.12. The hardness values vary depending on the differences in main elements, their concentrations and atomic sizes, and the heat treatment process. The as-cast RA01 alloy has a low value of 291 ± 12 HV (2849 ± 118 MPa) as it has high amounts of Ni (31 at.%) and Co (30 at.%), which are FCC

stabilizers, and low amounts of Al (8 at.%) and Fe (9 at.%). It is noteworthy to mention that the soft and ductile FCC phase is responsible for low hardness value. The HV value of as-cast RA01 alloy increases drastically to 420 ± 11 HV (4117 ± 104 MPa) when the alloy is heat-treated at 1073 K, and 403 ± 11 HV (3948 ± 110 MPa) when the alloy is heat-treated at 1273 K. This increase may be due to an increase in lattice strain energy.

The hardness value of as-cast RA08 alloy is measured as 534 ± 10 HV (5235 ± 95 MPa), which is higher than that of RA01 alloy. This difference may result from the lower concentration of Ni element, and higher concentrations of Nb and Ti elements in RA08 alloy. The HV value of as-cast RA08 alloy increases significantly to 611 ± 11 HV (5989 ± 106 MPa) when the alloy is heat-treated at 1073 K due to the presence of intermetallic phases. The increase in annealing temperature to 1273 K, the hardness value decreases sharply to 437 ± 13 HV (4289 ± 127 MPa). The decrease in hardness may be due to the increase in the volume fraction of the FCC phase with increasing heat treatment temperature. The grain growth may result in a decrease in hardness, as well.

The highest hardness values were observed in as-cast and heat-treated equiatomic RA10 alloy due to the high amount of Nb, Al, Fe, and Ti elements and the presence of the Laves phase. The hardness value of as-cast RA10 alloy increases from 702 ± 9 HV (6885 ± 90 MPa) to 756 ± 12 HV (7404 ± 120 MPa) when heat-treated at 1073 K. The hardness value decreases to 721 ± 3 HV (7061 ± 30 MPa) after 1273 K HT. The lowest HV values are observed in as-cast and heat-treated RA14 alloy. The HV value of 274 ± 10 HV (2688 ± 100 MPa) is achieved in as-cast RA14 alloy. The hardness values of RA14 and RA01 alloys are close to each other. The hardness value increases to 371 ± 6 HV (3637 ± 59 MPa) and 377 ± 15 HV (3697 ± 142 MPa) when heat-treated at 1073 K and 1273 K, respectively. The increase in hardness values is due to the presence of intermetallic phase formations.

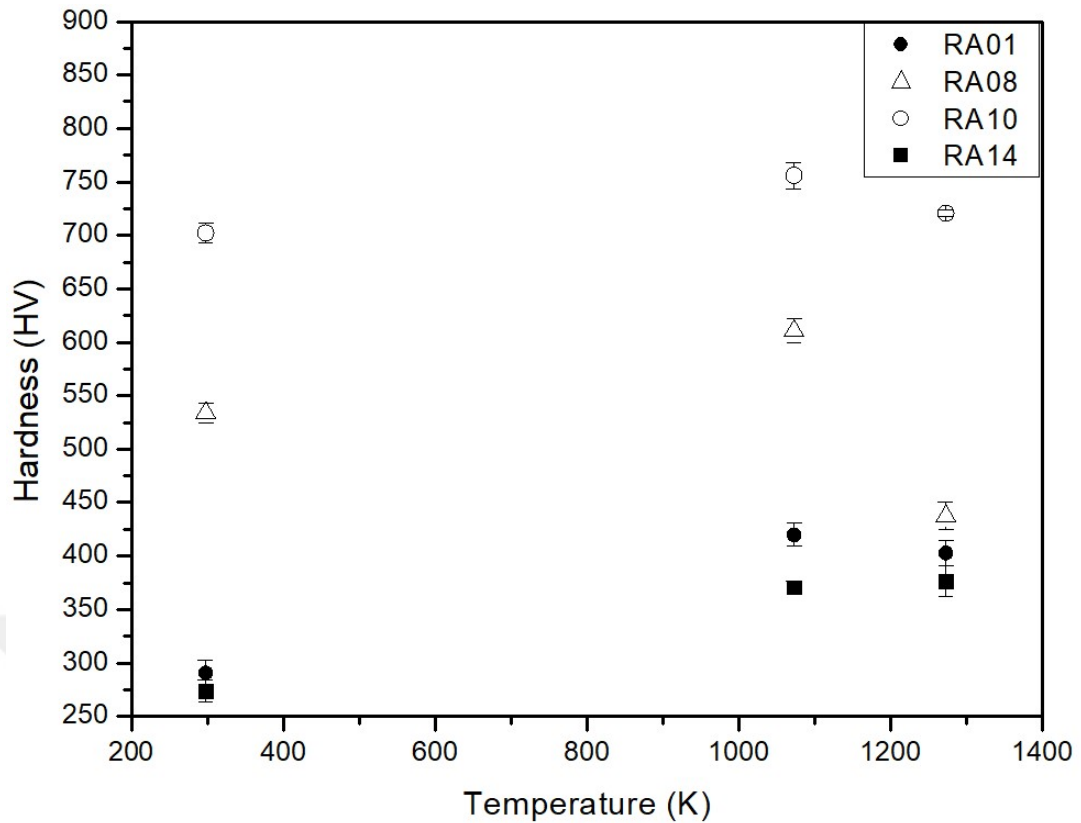


Figure 3. 12. Vickers hardness graph presenting hardness values with their standard deviations of both as-cast and heat-treated alloys at 1073 K and 1273 K.

3.4.2. Compression Tests

The compression tests were applied on as-cast RA01, RA08, and RA14 HEAs. RA10 alloy has multi intermetallic phases; therefore, it was also too brittle to conduct a compression test. The specimens were prepared initially due to the standards (as mentioned in the previous chapter), and the photos of specimens before and after compression tests are given in Figure 3.13. The RA01 and RA14 alloy specimens were completely barreled after the compression test was completed. The RA01 and RA14 alloys are also extraordinarily ductile and due to their high amount of FCC phase. Barreling occurs in these alloys due to strain hardening; thus, the plastic deformation occurs after a specific stress value, cross-sectional areas of specimens change, and diameters increase after the compressive force, which is called the bulge effect. The RA08 alloy specimen after the compression test, as shown in Figure 3.13, was fractured with an angle closed to 45°, which is an indicator of ductile behavior. RA08

alloy has a mixed FCC+BCC structure, and the presence of FCC improves the ductility of an alloy.

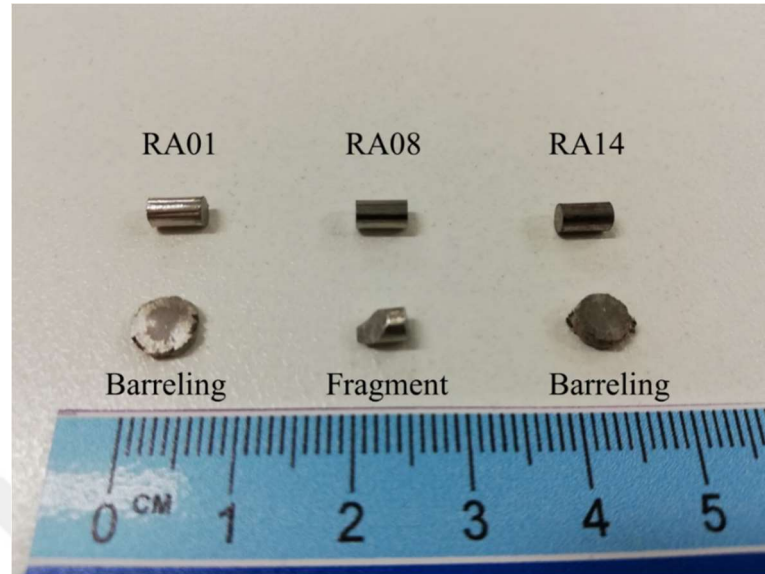


Figure 3. 13. The 3 mm diameter and 5 mm length compression test specimens of RA01, RA08, and RA14 alloys, which were prepared due to standards (top) and the barreled and fragmented specimens after compression tests (below).

Figure 3.14 shows the compressive engineering stress-strain diagrams of as-cast RA01, RA08, and RA14 alloys. The bulging of RA01 and RA14 alloys due to strain hardening are observed from their stress-strain curves, as well. It is seen that RA01 and RA14 alloys strain hardened, starting from 3141 MPa and 1834 MPa stress levels, respectively. Table 3.6 tabulates the compressive yield strength (σ_y), ultimate compressive strength (σ_{max}), and compressive fracture strain (ϵ_f) of RA01, RA08, and RA14 alloys. The σ_y values of the alloys were determined from the diagrams using 0.002 strain offset rule. The compressive σ_y values of RA01 and RA14 are determined as 387 MPa and 343 MPa, respectively. The presence of the tetraetaenite FeNi phase can be interpreted as responsible for the lower σ_y value of RA14 than that of RA01 alloy. Due to the bulge effect, the ultimate compressive strength (σ_{max}) and compressive fracture strain (ϵ_f) values could not be determined from their compression tests.

The fracture of the RA08 alloy specimen occurs after a nice plastic deformation, as seen from its compressive engineering stress-strain diagram in Figure 3.14. The

compressive σ_y , σ_{max} , and ϵ_f values of RA08 alloy were determined as 848 MPa, 2615 MPa, and 21.76%, as listed in Table 3.6. The significant increase in the σ_y value of RA08 compared to RA01 and RA14 alloys are mainly due to the BCC and intermetallic Laves phases. It should be mentioned that the high Ti concentration in RA08 alloy enhances the strength of the alloy significantly.

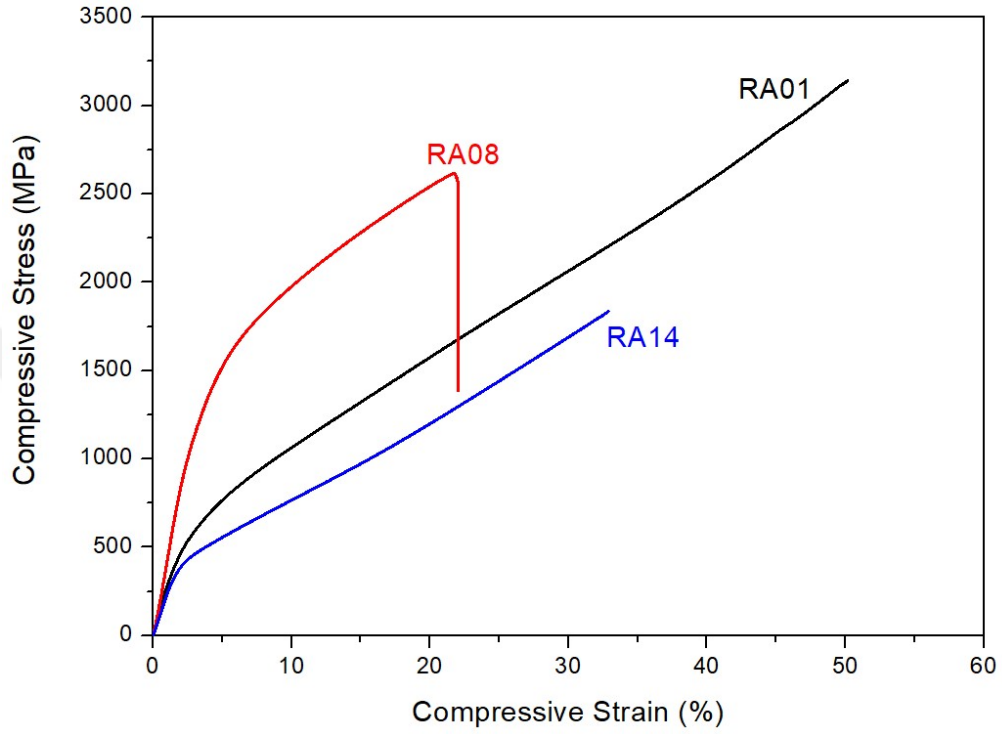


Figure 3. 14. Compressive stress-strain curves of RA01, RA08, and RA14 HEAs.

Table 3. 6. Compressive properties of RA01, RA08, RA14 HEAs.

Alloy	σ_y (MPa)	σ_{max} (MPa)	ϵ_f (%)
RA01	387	-	-
RA08	848	2616	21.77
RA14	343	-	-

The fractured surface of RA08 HEA after compression test were investigated using SEM. Figure 3.15 (a) and (b) indicate the SEM images of the fractured surface of RA08 alloy. The fracture surface of RA08 alloy indicates cleavage fracture implying a brittle character and dimples in various sizes due to the ductile type of behavior. The surface of the alloy shows cleavage facets and river patterns. It shows the brittle character of fracture due to the presence of Laves and BCC phases. The presence of dimples, which are microvoids that occurred during ductile fracture, and dimpled rupture is the indicator of plastic deformation. The FCC phase is responsible for the ductile type of fracture.

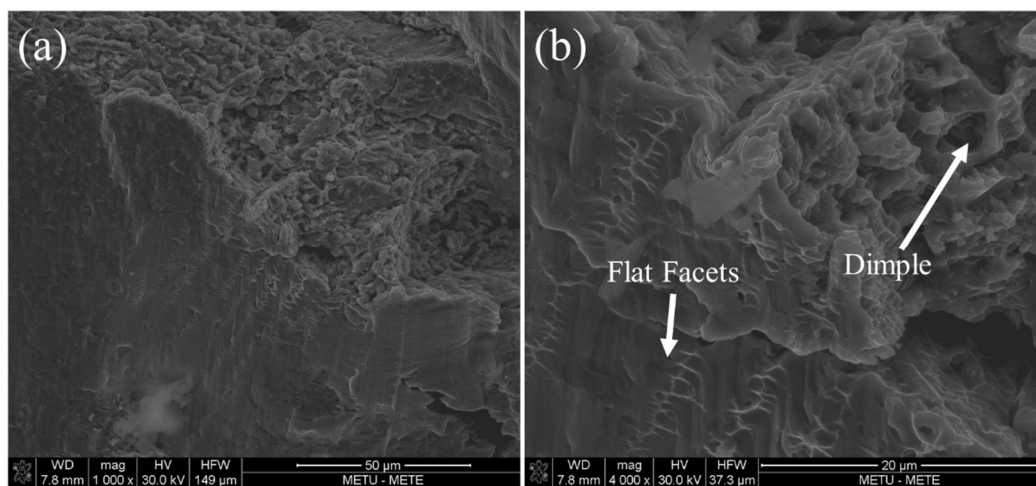


Figure 3. 15. SEM micrographs of the fractured surface of RA08 alloy after compression test.

Comparison of compressive properties of RA01, RA08, and RA14 HEAs with other CoCrFeNi-based alloys is presented in Table 3.7. It is seen that both 3 alloys have better compressive properties. Thus it may have the potential for structural applications compared to other alloys except for the CoCrFeMnNiTi_{0.25} alloy. Higher Co and lower Nb-Ti contents can be attributed to lower yield strength and higher strain level.

Table 3. 7. Comparison of compressive properties of HEAs with CoCrFeNi-based alloys.

Alloys	σ_y (MPa)	ϵ_f (%)
RA01 ($\text{Al}_8\text{Co}_{30}\text{Cr}_{18}\text{Fe}_9\text{Ni}_{31}\text{Nb}_4$)	387	-
RA08 ($\text{Al}_8\text{Co}_{30}\text{Cr}_{18}\text{Fe}_9\text{Ni}_{25}\text{Nb}_5\text{Ti}_5$)	848	21.77
RA14 ($\text{Al}_8\text{Co}_{30}\text{Cr}_{18}\text{Fe}_9\text{Ni}_{31}\text{Nb}_4$)	343	-
$\text{AlCo}_{0.25}\text{CrFeNi}$ [41]	1363	19
$\text{AlCo}_{0.75}\text{CrFeNi}$ [41]	1332	20
$\text{AlCoCrFeNb}_{0.25}\text{Ni}$ [79]	1959	10.5
$\text{AlCoCrFeNb}_{0.75}\text{Ni}$ [79]	2473	4.1
$\text{CoCrFeMnNiTi}_{0.25}$ [80]	317	-
$\text{CoCrFeMnNiTi}_{0.75}$ [80]	1578	7

3.4.3. Tensile Test Results of RA01 and RA14 High Entropy Alloys

The uniaxial tensile tests of RA01 and RA14 alloys were carried out to determine the yield strength (σ_y), tensile strength (σ_{UTS}), and strain rate (ϵ_f) because the compression tests these alloys did not supply these parameters due to bulging. Aluminum 3105 alloy was used as a standard tensile test specimen to compare the mechanical test results. Figure 3.16 (a) and (b) show the tensile stress-strain diagrams of as-cast RA01 and RA14 alloys and Aluminum 3105 alloy.

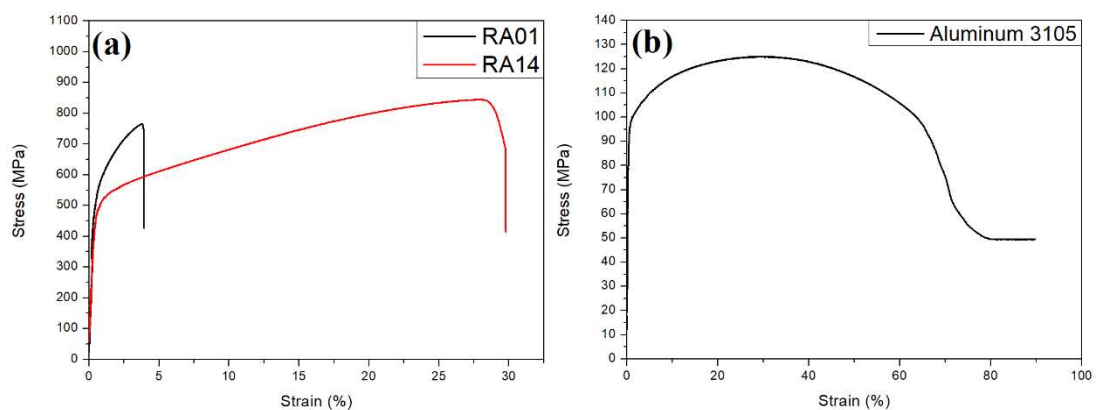


Figure 3. 16. Tensile test results of (a) RA01 and RA14 HEAs, and (b) Aluminum 3105 alloy.

The standard Aluminum 3105 alloy is composed of $AlMn_{0.5}Mg_{0.5}$ compound, which is greatly formable, weldable, and highly corrosion resistant alloy. The ultimate tensile strength value of Aluminum 3105 alloy was reported between 115 and 145 MPa [81]. The ultimate tensile strength value of Aluminum 3105 was determined as 125 MPa from the stress-strain diagram in Figure 3.16 (b). This value is in the acceptable range, which shows the reliability of the tensile test machine and tensile test analysis. The stress-strain diagrams of as-cast RA01 and RA14 alloys in Figure 3.16 (a) present the yielding followed by the plastic deformation region and fracture of the alloys. The tensile test analysis of the alloys also reveals the ductile behavior of alloys. It is clear that RA14 alloy is more ductile than RA01 alloy where the area under the stress-strain curve of RA14 upon fracture is greater than that of RA01 alloy. The yield strength (σ_y), ultimate tensile strength (σ_{UTS}), and tensile fracture strain (ϵ_f) values determined from stress-strain diagrams in Figure 3.16 were listed in Table 3.7. The ϵ_f values were determined using the 0.002 strain offset rule. The σ_y were determined as 568 MPa and 486 MPa for RA01 and RA14 alloys, respectively. The σ_{UTS} and ϵ_f values were determined as 765 MPa and 3.90% for RA01, and 844 MPa and 29.76% for RA14 alloy, respectively. The higher σ_y value of RA01 is due to the Nb concentration of the alloy. RA14 has more considerable ductility and toughness.

Table 3. 8. Values yield strength (σ_y), ultimate tensile strength (σ_{UTS}), and strain values at break (ϵ_{comp}) for RA01 and RA14 HEAs.

Alloy	σ_y (MPa)	σ_{max} (MPa)	ϵ_f (%)
Aluminum 3105	-	125	-
RA01	568	765	3.90
RA14	486	844	29.76

SEM images in Figure 3.17 (a, b) and (c, d) present the fractured surfaces of RA01 and RA14 alloy after the tensile test, respectively. Fractured surfaces of both alloys indicate dimples and dimpled rupture, which reveals the ductile type of fracture. The dimple sizes are greater for RA14 alloy than that of RA01 alloy. This difference is

mainly due to the higher strain rate of RA14, where the dimple density decreases, and thus the dimple size increases due to the increase in strain rate.

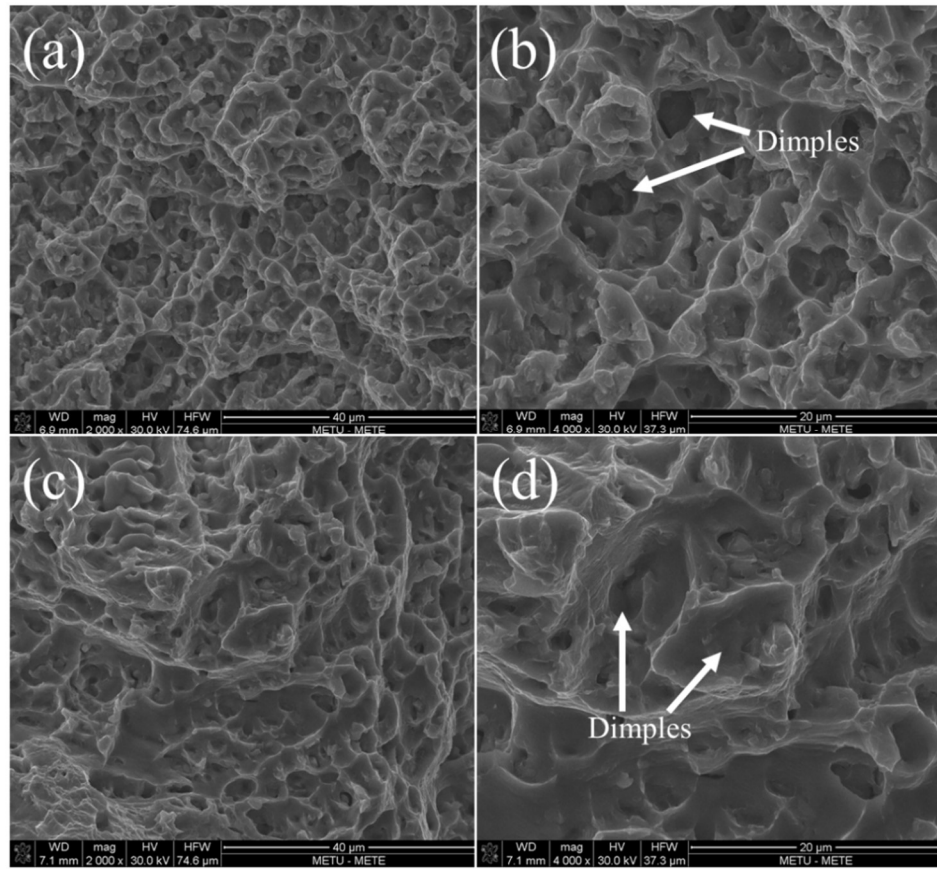


Figure 3.17. SEM images of fractured surfaces of (a, b) RA01 and (c, d) RA14 alloys after tensile test.

3.5. Characterization of High Entropy Alloys for High-Temperature Applications

The AlHfMoNbTaTi (RA20) and AlHfMoNbTaTiV (RA23) alloys were investigated to determine their high-temperature behavior. The calculated thermodynamic parameters, ΔH_{mix} , ΔS_{mix} , VEC, and atomic size differences (δ) of equiatomic RA20 and RA23 alloys, were listed in Table 3.10. Both alloys have medium-negative ΔH_{mix} values, which indicate that solid solution phases may form. The expected crystal structure is BCC for RA20 and RA23 alloys based on the VEC numbers. Furthermore, the atomic size differences, δ , are also small enough to prevent any possible intermetallic phase formation. Atomic radius values of each constituent element of RA20 and RA23 alloys are given in Table 3.11. According to the estimated values of

density (ρ) and melting point (T_m), it is concluded that both alloys are appropriate for low density and high melting point criteria. Therefore, these two alloys were designed for high temperature applications because of their low density and high melting temperature values. Table 3.9 gives the list of crystal structures, densities (ρ), and melting points (T_m) of RA20, RA23, and other reported alloys with similar compositions. All the densities are experimentally calculated ones except RA20 (AlHfMoNbTaTi) and RA23 (AlHfMoNbTaTiV) alloys. RA20 and RA23 alloys have great potential as high temperature applications with their high melting points.

Table 3. 9. Crystal structures, densities (ρ), and melting points (T_m) of RA20, RA23 alloys, and other alloy systems published in recent years.

Alloys	Crystal structure	ρ (g.cm ⁻³)	T_m (°C)
AlHfMoNbTaTi	B2+BCC	9.58 (Theor.)	2112
AlHfMoNbTaTiV	B2+BCC	9.18 (Theor.)	2083
AlMoNbTi [83]	BCC	6.46	1780
AlMoNbTaTi [84]	BCC	8.54	2089
AlMoTaTiV [85]	BCC	8.05	-
AlMoNbTaV [86]	BCC (at 873 K)	9.10	2202
AlCrMoNbTi [83]	BCC + Laves	6.56	1780
AlCrMoNbTiV [86]	BCC (at 873 K)	6.50	1881
MoNbTaTiV [86]	BCC1 + BCC2	9.40	2325
Al _{0.2} MoNbTaTiV [87]	BCC1 + BCC2	9.12	2543
Al _{0.6} MoNbTaTiV [87]	BCC1 + BCC2	8.79	2428
Al ₁ MoNbTaTiV [87]	BCC1 + BCC2	8.15	2328
AlMo _{0.5} NbTa _{0.5} TiZr [88]	BCC1 + BCC2	7.14	1982
AlMo _{0.5} NbTa _{0.5} TiZr _{0.5} [19]	B2	7.40	-
AlNbTa _{0.5} TiZr _{0.5} [19]	B2	7.10	-
AlHfNbTaTiZr [89]	BCC1 + BCC2	8.92	-
Al _{0.5} HfNbTaTiZr [89]	BCC	9.34	-
HfNbTaTiZr [65]	BCC	9.72	-

Table 3. 10. Thermodynamical parameters of RA20 and RA23 alloys.

Alloy	ΔH_{mix} (kJmol ⁻¹)	ΔS_{mix} (JK ⁻¹ mol ⁻¹)	VEC	δ	ρ (g/cm ³)	T _m (K)
RA20	-13.15	14.9	4.5	4.47	9.58	2385.1
RA23	-13.03	16.18	4.57	5.31	9.18	2356.1

Table 3. 11. Atomic radius values in nm of each element in RHEAs.

Elements	Atomic Radius (nm)
Al	0.14317 [33]
Hf	0.15775 [33]
Mo	0.13626 [33]
Nb	0.14290 [33]
Ta	0.14300 [33]
Ti	0.14615 [33]
V	0.13160 [33]

3.5.1. In situ XRD Analysis of Refractory High Entropy Alloys

In situ XRD technique was used to investigate the structure and phase stability of RA20 and RA23 alloys while heating. The XRD patterns were obtained while gradually increasing annealing steps. Figure 3.18 indicates the in situ XRD patterns of RA20 alloy prepared in the powder form. In situ XRD patterns of RA20 alloy show mixed BCC+B2 phase structure at room temperature. The phase structure of RA20 alloy does not change during heating and apparently sustains its stability at high temperatures. The lattice parameter of the BCC phase was determined as 0.3260 nm at room temperature. The BCC peaks shift toward smaller thetas. Thus the lattice parameter of BCC increases slightly while heating. Figure 3.19 shows the XRD pattern of RA20 after quenched to room temperature. The XRD pattern has B2/BCC reflections, as well.

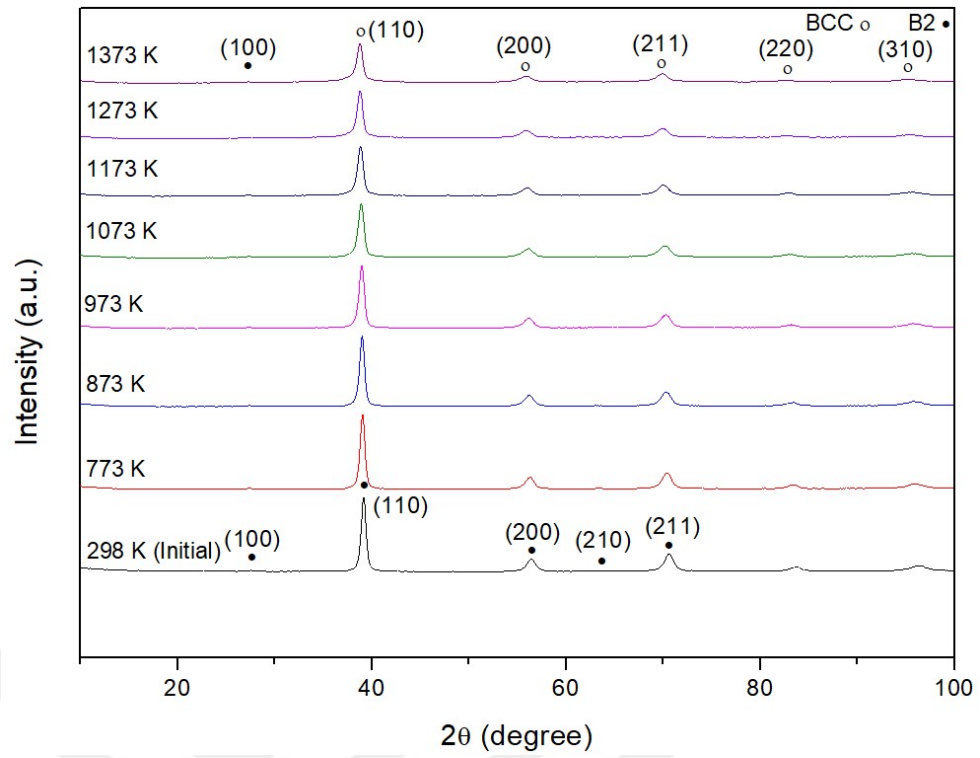


Figure 3. 18. In situ XRD patterns of RA20 alloy.

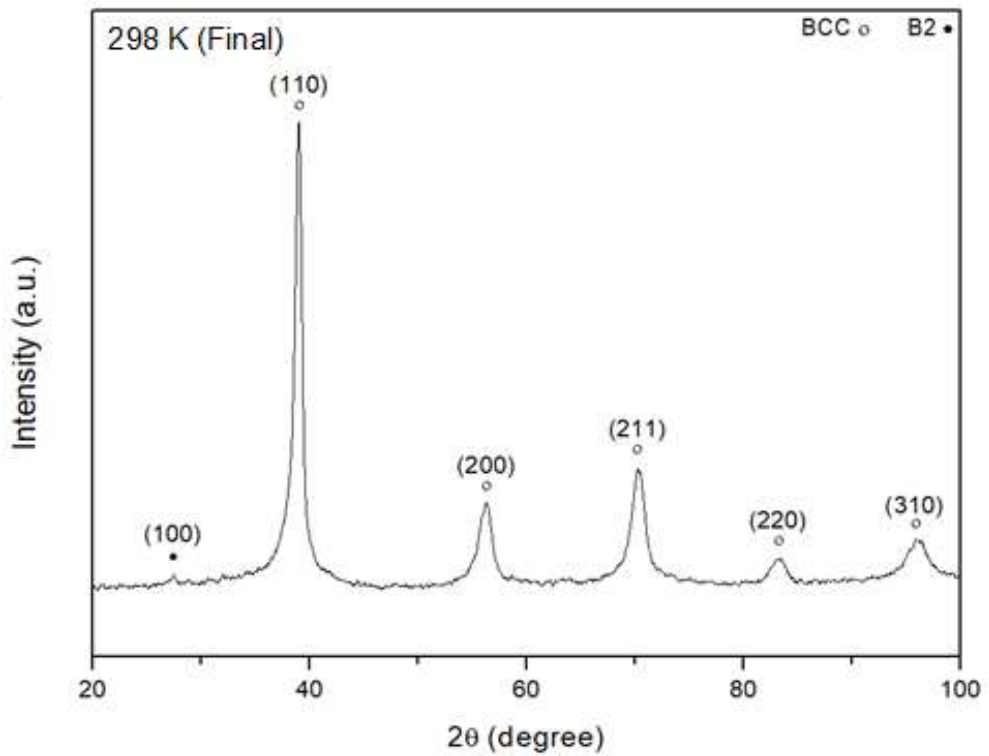


Figure 3. 19. XRD pattern of RA20 alloy after quenching to room temperature.

The in situ XRD patterns of RA23 alloy in the powder form is shown in Figure 3.19. In situ XRD patterns of RA20 alloy show mixed BCC+B2 phase structure at room temperature. The phase stability of RA20 alloy is observed while heating the alloy. The mixed BCC+B2 phase structure is commonly seen for HEAs. The coherent relationship between BCC and B2 phases is important, especially for mechanical properties. The lattice parameter of the BCC phase was determined as 0.3228 nm at room temperature. The BCC peaks shift toward smaller thetas, so the lattice parameter of BCC increases slightly while heating. In the XRD pattern of RA23 after quenched to room temperature shown in Figure 3.21, lattice parameter of the BCC phase is calculated as 0.3248 nm due to the shifting of reflections. Table 3.12 gives the list of ΔH_{mix} values of constituent elements of RA20 and RA23 alloys.

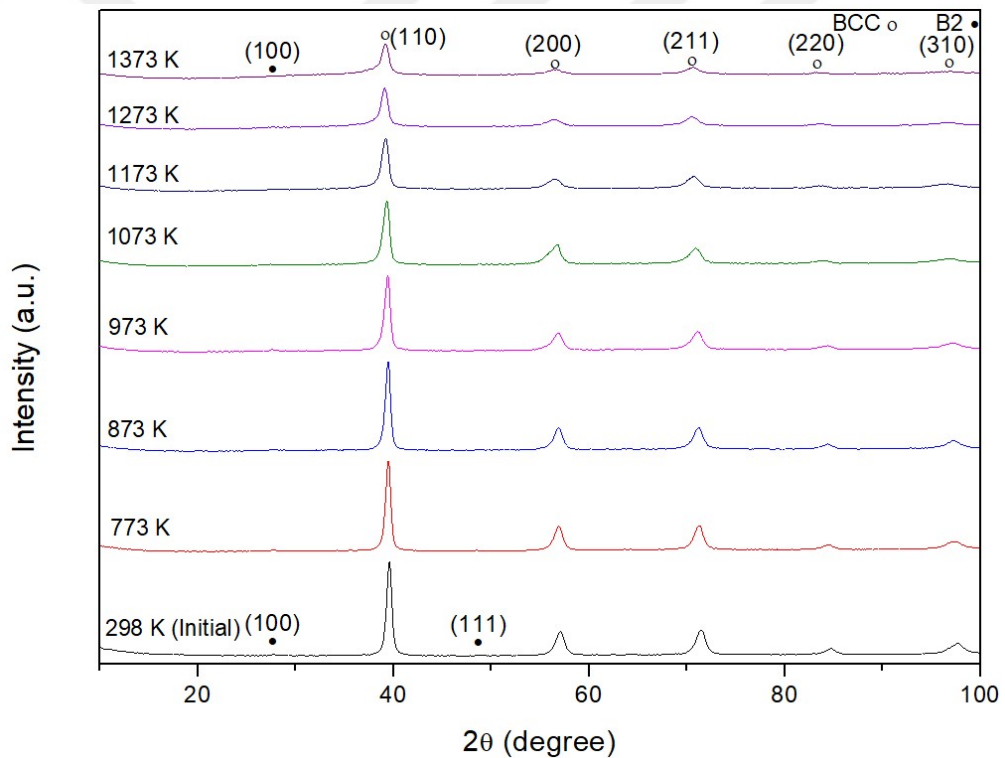


Figure 3. 20. In situ XRD pattern of RA23 alloy.

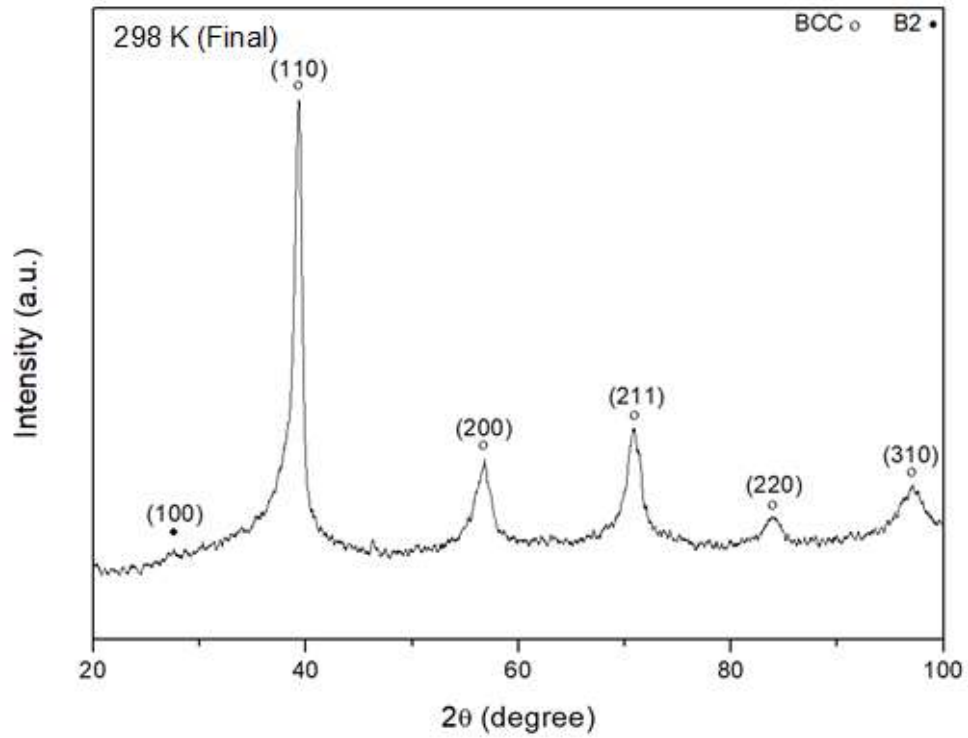


Figure 3. 21. XRD pattern of RA23 alloy after quenching to room temperature.

Table 3. 12. ΔH_{mix} values of constituent elements of RA20 and RA23 alloys [76].

Al	Hf	Mo	Nb	Ta	Ti	V	
	-38.5	-5.1	-18.2	-19.2	-29.5	-16.3	Al
		-4.0	3.9	2.9	-1.0	-2.2	Hf
			-5.7	-4.9	-3.6	0.0	Mo
				0.0	2.0	-1.0	Nb
					1.40	-1.00	Ta
						-1.70	Ti
							V

3.5.2. Microstructure Analysis of RA20 and RA23 High Entropy Alloys

Figure 3.20 (a,b) and (c, d) show the OM images of as-cast RA20 and RA23 alloys, respectively. Both alloys have partially similar microstructures, and each microstructure consists of darker dendritic and lighter interdendritic regions and precipitates. These OM images reveal the presence of a double BCC+B2 phase. It is clear that these spherical precipitates are distributed through the dendritic matrix.

Based on the coherency between disordered BCC and ordered B2 phases, the spherical BCC particles are embedded into the B2 matrix.

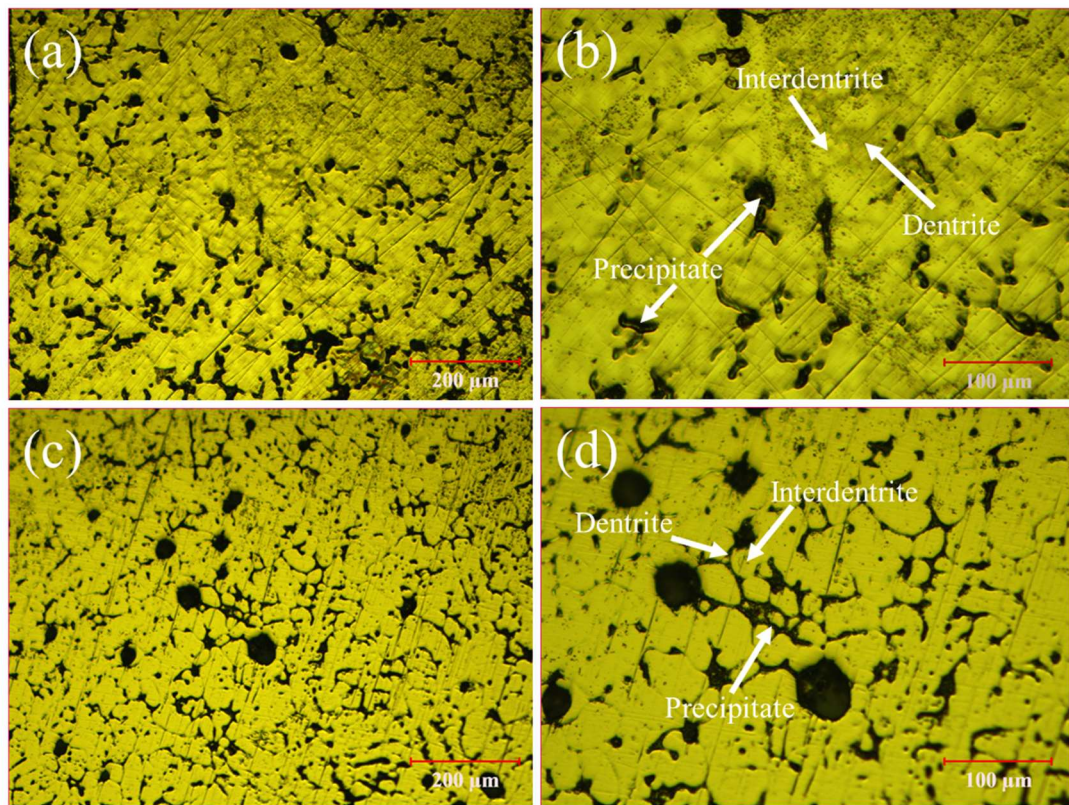


Figure 3. 22. Optical microscopy images of as-cast (a – b) RA20 and (c – d) RA23 alloys.

The elemental analysis of the alloys was carried out from overall, dendritic, and interdendritic regions. Table 3.4 and Table 3.5 list the EDS analysis results of alloys. The segregations of Al and Hf elements were observed through dendritic regions RA20 alloy. Likewise, slight increases in Al and Hf, and differently, Ti elements are also observed through dendritic regions of RA23 alloy. On the other hand, Ta, Ti, Mo, and Nb elements are distributed throughout interdendritic regions of RA20, while Ta, V, Mo, Nb elements piled up at interdendritic regions of RA23 alloy.

Table 3. 13. Overall, dendritic (D), and interdendritic (ID) EDS results of RHEAs in at.%.

	RA20			RA23		
	Overall	D	ID	Overall	D	ID
Al	21.71	25.09	16.28	16.17	18.32	15.30
Hf	19.92	30.70	16.47	16.18	17.37	14.72
Mo	10.81	8.15	13.74	8.52	7.07	9.08
Nb	11.82	9.00	14.41	9.25	9.37	10.14
Ta	12.98	6.19	17.95	14.25	9.55	15.94
Ti	22.60	20.89	21.17	17.84	19.84	17.31
V	-	-	-	17.78	16.61	17.52

3.5.3. Hardness Measurements of Alloys

The microhardness test results of as-cast RA20 and RA23 RHEAs are given in Figure 3.21. The hardness values of RA20 and RA23 were determined as 532 ± 16 HV (5217 ± 160 MPa) and 542 ± 11 HV (5315 ± 111 MPa), respectively. The hardness values are so closed to each other as both alloys have similar structures.

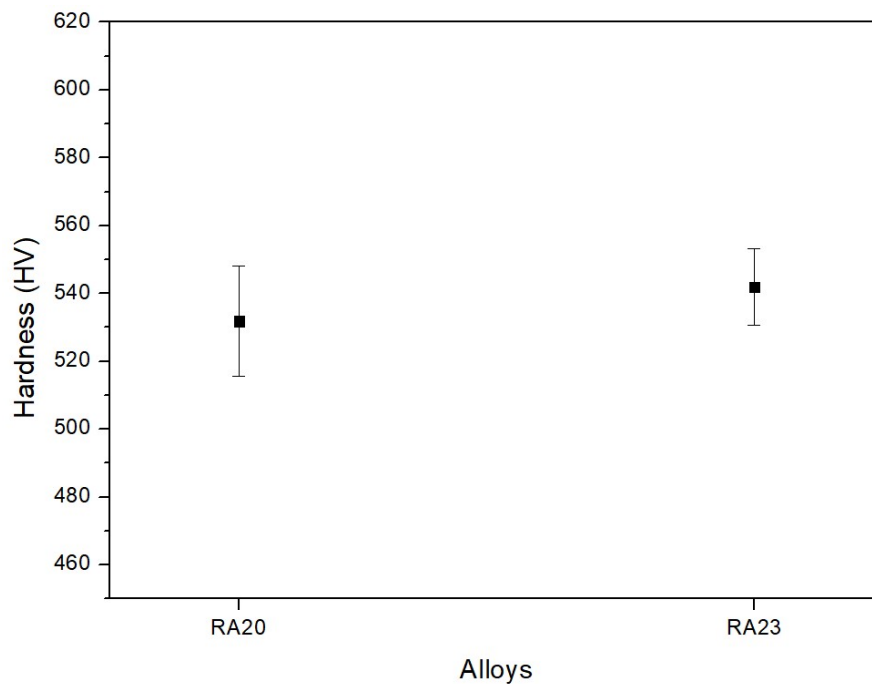


Figure 3. 23. Vickers hardness graph presenting hardness values of as-cast RA20 and RA23 with their standard deviations.

CHAPTER IV

CONCLUSIONS AND FUTURE PREDICTIONS

4.1. Conclusions

This thesis focused on the synthesis and development of refractory high entropy alloys. This study concentrated on Al-Co-Cr-Fe-Ni-Nb-Ti and Al-Hf-Mo-Nb-Ta-Ti-V based systems. The thermodynamic data of alloys were first estimated, and the selected alloys were produced by vacuum arc melter using high purity elements. The high entropy alloy systems were investigated using X-ray diffraction (XRD), in-situ X-ray diffraction (XRD), optic microscope (OM), scanning electron microscope (SEM), hardness, compression, and tension tests. The conclusions of this study can be given as follows:

- The thermodynamic calculations show that the variation of Ni, Nb, and Ti concentrations of the alloys effect the thermodynamic parameters of the high entropy alloys.
- The analysis reveals the dependency of mechanical properties and phase formation on Nb and Ti concentration of the Al-Co-Cr-Fe-(Ni-Nb-Ti) alloy systems.
- Single FCC phase for RA01 and RA14 alloys, mixed FCC+BCC phase for RA08 alloy that are observed in XRD analysis are coherent with VEC calculations except RA10.
- Intermetallic phase formation is sometimes inevitable due to high-negative ΔH_{mix} , values of atomic pairs composed in alloys.
- Dendritic and interdendritic regions observed in OM and SEM micrographs are the evidence for multiple phase formation.
- Nb and Ti elements are poorly compatible with each other, and allowed the formation of intermetallic phases in alloys.

- Density and dispersity of dendritic/interdendritic regions in microstructure depend on increase in intermetallic behavior.
- Phase and microstructural stabilities for Al-Co-Cr-Fe-(Ni-Nb-Ti)-based alloys depend on the intermetallic structure at high temperatures.
- RA14 with 4 at.% Ti content is oxidized after 1273 K HT due to low oxidation resistance of Ti compared Nb element, which consisted in RA01.
- The enhancements of hardness values were observed with Nb and Ti.
- The as-cast $\text{Al}_8\text{Co}_{30}\text{Cr}_{18}\text{Fe}_9\text{Ni}_{31}\text{Nb}_4$ and $\text{Al}_8\text{Co}_{30}\text{Cr}_{18}\text{Fe}_9\text{Ni}_{31}\text{Ti}_4$ alloys show the ductile type of fracture, and the highest toughness value was achieved in $\text{Al}_8\text{Co}_{30}\text{Cr}_{18}\text{Fe}_9\text{Ni}_{31}\text{Ti}_4$ alloy, which has tetraetaenite FeNi intermetallic phase.
- The highest ultimate tensile strength of 844 MPa and the highest compressive fracture strain of 29.76% were observed for this alloy.
- The compression tests show that RA08 has the most brittle character due to its intermetallic phase
- The tensile test reveals the highest ductility, highest toughness, and highest strength for RA14 HEA.
- The Al-Hf-Mo-Nb-Ta-Ti-V alloy systems (RA20 and RA23) indicate good phase stability upon heating. B2/BCC dual-phase structure were seen in the alloy systems. The analysis show that these two systems are also good candidates for potential high-temperature applications.

4.2. Future Recommendations

Based on the current results, future suggestions can be stated as follows:

- The high temperature tensile tests can be applied on RA20 and RA23 alloys to investigate their high temperature mechanical behavior. These alloys have good potential as RHEA for high temperature applications.
- In elevated temperature applications, the thermal fatigue and creep behavior of materials are critical parameters. Therefore, the fatigue and creep tests can be performed, especially on RA20 and RA23 HEAs.

- The oxidation resistance is very crucial for RHEAs at elevated temperatures. The oxidation results in the degradation of the mechanical properties of the alloys. Therefore oxidation tests can be carried out to understand the oxidation behavior of RHEAs.
- Corrosion is one of the main causes of the failure of materials. Previous studies have shown the good passivation characteristics of HEAs. Thus, the corrosion test can be performed to test the corrosion resistance of alloys.



REFERENCES

- [1] Shewmon, P., & Gill, C. (2018). *Metallurgy*. Retrieved 2020.
- [2] Murty, B., Yeh, J., & Ranganathan, S. (2014). *High-Entropy Alloys*. 1st ed. San Diego: Elsevier.
- [3] Tasan, C., Deng, Y., Pradeep, K., Yao, M., Springer, H., & Raabe, D. (2014). Composition Dependence of Phase Stability, Deformation Mechanisms, and Mechanical Properties of the CoCrFeMnNi High-Entropy Alloy System. *JOM*, 66(10), pp.1993-2001.
- [4] Pradeep, K., Tasan, C., Yao, M., Deng, Y., Springer, H., & Raabe, D. (2015). Non-equiatomic high entropy alloys: Approach towards rapid alloy screening and property-oriented design. *Materials Science and Engineering: A*, 648, pp.183-192.
- [5] Miracle, D., & Senkov, O. (2017). A critical review of high entropy alloys and related concepts. *Acta Materialia*, 122, pp.448-511.
- [6] Gao, M., Gao, M., Yeh, J., Liaw, P., & Zhang, Y. (2016). *High-Entropy Alloys*. Cham: Springer International Publishing.
- [7] Yeh, J., Chen, S., Lin, S., Gan, J., Chin, T., Shun, T., Tsau, C., & Chang, S. (2004). Nanostructured High-Entropy Alloys with Multiple Principal Elements: Novel Alloy Design Concepts and Outcomes. *Advanced Engineering Materials*, 6(5), pp.299-303.
- [8] Zhang, Y., Zuo, T., Tang, Z., Gao, M., Dahmen, K., Liaw, P., & Lu, Z. (2013). Microstructures and properties of high-entropy alloys. *Progress in Materials Science*, 61, pp.1-93.

- [9] Yeh, J. (2006). Recent progress in high-entropy alloys. *Annales de Chimie Science des Matériaux*, 31(6), pp.633-648.
- [10] Cantor, B., Chang, I., Knight, P., & Vincent, A. (2004). Microstructural development in equiatomic multicomponent alloys. *Materials Science and Engineering: A*, 375-377, pp.213-218.
- [11] Gludovatz, B., Hohenwarter, A., Catoor, D., Chang, E. H., George, E. P., & Ritchie, R. O. (2014). A fracture-resistant high-entropy alloy for cryogenic applications. *Science*, 345(6201), pp.1153–1158.
- [12] Senkov, O. N., & Miracle, D. B. (2001). Effect of the atomic size distribution on glass forming ability of amorphous metallic alloys. *Materials Research Bulletin*, 36(12), pp.2183–2198.
- [13] Winter, M. The periodic table of the elements. Retrieved 2020, from <https://www.webelements.com/>
- [14] Liu, Y. Y., Chen, Z., Shi, J. C., Wang, Z. Y., & Zhang, J. Y. (2019). The effect of Al content on microstructures and comprehensive properties in Al_xCoCrCuFeNi high entropy alloys. *Vacuum*, 161, pp.143–149.
- [15] Wu, J. M., Lin, S. J., Yeh, J. W., Chen, S. K., Huang, Y. S., & Chen, H. C. (2006). Adhesive wear behavior of Al_xCoCrCuFeNi high-entropy alloys as a function of aluminum content. *Wear*, 261(5–6), pp.513–519.
- [16] He, J. Y., Liu, W. H., Wang, H., Wu, Y., Liu, X. J., Nieh, T. G., & Lu, Z. P. (2014). Effects of Al addition on structural evolution and tensile properties of the FeCoNiCrMn high-entropy alloy system. *Acta Materialia*, 62, pp.105–113.
- [17] Joseph, J., Jarvis, T., Wu, X., Stanford, N., Hodgson, P., & Fabijanic, D. M. (2015). Comparative study of the microstructures and mechanical properties of direct laser fabricated and arc-melted Al_xCoCrFeNi high entropy alloys. *Materials Science and Engineering: A*, 633, pp.184–193.
- [18] Joseph, J., Stanford, N., Hodgson, P., & Fabijanic, D. M. (2017). Understanding the mechanical behaviour and the large strength/ductility differences between FCC and BCC Al_xCoCrFeNi high entropy alloys. *Journal of Alloys and Compounds*, 726, pp.885–895.

- [19] Senkov, O. N., Miracle, D. B., Chaput, K. J., & Couzinie, J.-P. (2018). Development and exploration of refractory high entropy alloys—A review. *Journal of Materials Research*, 33(19), pp.3092–3128.
- [20] Senkov, O. N., Wilks, G. B., Miracle, D. B., Chuang, C. P., & Liaw, P. K. (2010). Refractory high-entropy alloys. *Intermetallics*, 18(9), pp.1758–1765.
- [21] Mishra, S. S., Yadav, T. P., Srivastava, O. N., Mukhopadhyay, N. K., & Biswas, K. (2020). Formation and stability of C14 type Laves phase in multi component high-entropy alloys. *Journal of Alloys and Compounds*, 832.
- [22] Detrois, M., Antonov, S., & Tin, S. (2019). Phase stability and thermodynamic database validation in a set of non-equiatomic Al-Co-Cr-Fe-Nb-Ni high-entropy alloys. *Intermetallics*, 104, pp.103–112.
- [23] Antonov, S., Detrois, M., & Tin, S. (2017). Design of Novel Precipitate-Strengthened Al-Co-Cr-Fe-Nb-Ni High-Entropy Superalloys. *Metallurgical and Materials Transactions A*, 49(1), pp.305–320.
- [24] Xu, X., Guo, S., Nieh, T., Liu, C., Hirata, A., & Chen, M. (2019). Effects of mixing enthalpy and cooling rate on phase formation of Al_xCoCrCuFeNi high-entropy alloys. *Materialia*, 6.
- [25] Ye, Y., Wang, Q., Lu, J., Liu, C., and Yang, Y. (2016). High-entropy alloy: challenges and prospects. *Materials Today*, 19(6), pp.349-362.
- [26] Cheng, C., Yang, Y., Zhong, Y., Chen, Y., Hsu, T., & Yeh, J. (2017). Physical metallurgy of concentrated solid solutions from low-entropy to high-entropy alloys. *Current Opinion in Solid State and Materials Science*, 21(6), pp.299-311.
- [27] Li, Z., Zhao, S., Ritchie, R., & Meyers, M. (2019). Mechanical properties of high-entropy alloys with emphasis on face-centered cubic alloys. *Progress in Materials Science*, 102, pp.296-345.
- [28] Yeh, J., Lin, S., Chin, T., Gan, J., Chen, S., Shun, T., Tsau, C., & Chou, S. (2004). Formation of simple crystal structures in Cu-Co-Ni-Cr-Al-Fe-Ti-V alloys with multiprincipal metallic elements. *Metallurgical and Materials Transactions A*, 35(8), pp.2533-2536.

- [29] Tsai, M., Fan, A., & Wang, H. (2017). Effect of atomic size difference on the type of major intermetallic phase in arc-melted CoCrFeNiX high-entropy alloys. *Journal of Alloys and Compounds*, 695, pp.1479-1487.
- [30] Tsai, K. Y., Tsai, M. H., & Yeh, J. W. (2013). Sluggish diffusion in Co–Cr–Fe–Mn–Ni high-entropy alloys. *Acta Materialia*, 61(13), pp.4887–4897.
- [31] Chen, J., Zhou, X., Wang, W., Liu, B., Lv, Y., Yang, W., Xu, D., & Liu, Y. (2018). A review on fundamental of high entropy alloys with promising high-temperature properties. *Journal of Alloys and Compounds*, 760, pp. 15–30.
- [32] Tsai, M. H., Yeh, J. W., & Gan, J. Y. (2008). Diffusion barrier properties of AlMoNbSiTaTiVZr high-entropy alloy layer between copper and silicon. *Thin Solid Films*, 516(16), pp.5527–5530.
- [33] Ranganathan, S. (2003). Alloyed pleasures: Multimetallic cocktails. *Current Science*, 85(10), pp.1404-1406.
- [34] Liu, Y. Y., Chen, Z., Chen, Y. Z., Shi, J. C., Wang, Z. Y., Wang, S., & Liu, F. (2019). Effect of Al content on high temperature oxidation resistance of Al_xCoCrCuFeNi high entropy alloys (x=0, 0.5, 1, 1.5, 2). *Vacuum*, 169.
- [35] Kang, M., Lim, K. R., Won, J. W., & Na, Y. S. (2018). Effect of Co content on the mechanical properties of A2 and B2 phases in AlCoxCrFeNi high-entropy alloys. *Journal of Alloys and Compounds*, 769, pp.808–812.
- [36] Guo, S., & Liu, C. T. (2011). Phase stability in high entropy alloys: Formation of solid-solution phase or amorphous phase. *Progress in Natural Science: Materials International*, 21(6), pp.433–446.
- [37] Wang, Z., Guo, S., & Liu, C. T. (2014). Phase Selection in High-Entropy Alloys: From Nonequilibrium to Equilibrium. *JOM*, 66(10), pp.1966–1972.
- [38] Tong, C. J., Chen, Y. L., Yeh, J. W., Lin, S. J., Chen, S. K., Shun, T. T., Tsau, C. H., & Chang, S. Y. (2005). Microstructure characterization of Al_xCoCrCuFeNi high-entropy alloy system with multiprincipal elements. *Metallurgical and Materials Transactions A*, 36(4), pp.881–893.

- [39] Zhang, Y., Zhou, Y. J., Lin, J. P., Chen, G. L., & Liaw, P. K. (2008). Solid-Solution Phase Formation Rules for Multi-component Alloys. *Advanced Engineering Materials*, 10(6), pp.534–538.
- [40] Avila-Rubio, M. A., Baldenebro-Lopez, J. A., Soto-Rojo, R., Ceballos-Mendivil, L. G., Carreño-Gallardo, Garza-Montes-de-Oca, N. F., & Baldenebro-Lopez, F. J. (2020). Effect of Mo and Ti on the microstructure and microhardness in AlCoFeNiMoTi high entropy alloys prepared by mechanical alloying and conventional sintering. *Advanced Powder Technology*, 31(4), pp.1693–1701.
- [41] Guo, S. (2013). Phase selection rules for cast high entropy alloys: an overview. *Materials Science and Technology*, 31(10), pp.1223–1230.
- [42] Yang, X., & Zhang, Y. (2012). Prediction of high-entropy stabilized solid-solution in multi-component alloys. *Materials Chemistry and Physics*, 132(2–3), pp.233–238.
- [43] Tsai, M. H., & Yeh, J. W. (2014). High-Entropy Alloys: A Critical Review. *Materials Research Letters*, 2(3), pp.107–123.
- [44] Callister, W. D., & Rethwisch, D. G. (2009). *Materials Science and Engineering: An Introduction, 8th Edition* (8th ed.). John Wiley and Sons.
- [45] Guo, S., Ng, C., Lu, J., & Liu, C. T. (2011). Effect of valence electron concentration on stability of fcc or bcc phase in high entropy alloys. *Journal of Applied Physics*, 109(10), pp.103505.
- [46] Manzoni, A., Daoud, H., Völkl, R., Glatzel, U., & Wanderka, N. (2013). Phase separation in equiatomic AlCoCrFeNi high-entropy alloy. *Ultramicroscopy*, 132, pp.212–215.
- [47] Park, J. M., Moon, J., Bae, J. W., Kim, D. H., Jo, Y. H., Lee, S., & Kim, H. S. (2019). Role of BCC phase on tensile behavior of dual-phase Al_{0.5}CoCrFeMnNi high-entropy alloy at cryogenic temperature. *Materials Science and Engineering: A*, 746, pp.443–447.

- [48] Senkov, O. N., Scott, J. M., Senkova, S. V., Miracle, D. B., & Woodward, C. F. (2011). Microstructure and room temperature properties of a high-entropy TaNbHfZrTi alloy. *Journal of Alloys and Compounds*, 509(20), pp.6043–6048.
- [49] Tung, C. C., Yeh, J. W., Shun, T., Chen, S. K., Huang, Y. S., & Chen, H. C. (2007). On the elemental effect of AlCoCrCuFeNi high-entropy alloy system. *Materials Letters*, 61(1), pp.1–5.
- [50] Zhang, K. B., Fu, Z. Y., Zhang, J. Y., Shi, J., Wang, W. M., Wang, H., Wang, Y. C., & Zhang, Q. J. (2009). Nanocrystalline CoCrFeNiCuAl high-entropy solid solution synthesized by mechanical alloying. *Journal of Alloys and Compounds*, 485(1–2), pp.L31–L34.
- [51] Sriharitha, R., Murty, B. S., & Kottada, R. S. (2013). Phase formation in mechanically alloyed Al_xCoCrCuFeNi (x = 0.45, 1, 2.5, 5 mol) high entropy alloys. *Intermetallics*, 32, pp.119–126.
- [52] Qin, G., Xue, W., Fan, C., Chen, R., Wang, L., Su, Y., Ding, H., & Guo, J. (2018). Effect of Co content on phase formation and mechanical properties of (AlCoCrFeNi)₁₀₀-Co high-entropy alloys. *Materials Science and Engineering: A*, 710, pp.200–205.
- [53] Koppoju, S., Konduri, S. P., Chalavadi, P., Bonta, S. R., & Mantripragada, R. (2019). Effect of Ni on Microstructure and Mechanical Properties of CrMnFeCoNi High Entropy Alloy. *Transactions of the Indian Institute of Metals*, 73(4), pp.853–862.
- [54] Qiu, H., Zhu, H., Zhang, J., & Xie, Z. (2020). Effect of Fe content upon the microstructures and mechanical properties of Fe_xCoNiCu high entropy alloys. *Materials Science and Engineering: A*, 769.
- [55] Yang, T., Zhao, Y. L., Tong, Y., Jiao, Z. B., Wei, J., Cai, J. X., Han, X. D., Chen, D., Hu, A., Kai, J. J., Lu, K., Liu, Y., & Liu, C. T. (2018). Multicomponent intermetallic nanoparticles and superb mechanical behaviors of complex alloys. *Science*, 362(6417), pp.933–937.

- [56] Mishra, S. S., Yadav, T. P., Srivastava, O. N., Mukhopadhyay, N. K., & Biswas, K. (2020). Formation and stability of C14 type Laves phase in multi component high-entropy alloys. *Journal of Alloys and Compounds*, 832.
- [57] Hsieh, C. C., & Wu, W. (2012). Overview of Intermetallic Sigma (σ) Phase Precipitation in Stainless Steels. *ISRN Metallurgy*, 2012, pp.1–16.
- [58] Wu, J. M., Lin, S. J., Yeh, J. W., Chen, S. K., Huang, Y. S., & Chen, H. C. (2006). Adhesive wear behavior of AlxCoCrCuFeNi high-entropy alloys as a function of aluminum content. *Wear*, 261(5–6), pp.513–519.
- [59] Meng, Y. H., Duan, F. H., Pan, J., & Li, Y. (2019). Phase stability of B2-ordered ZrTiHfCuNiFe high entropy alloy. *Intermetallics*, 111.
- [60] Ma, Y., Jiang, B., Li, C., Wang, Q., Dong, C., Liaw, P., Xu, F., & Sun, L. (2017). The BCC/B2 Morphologies in AlxNiCoFeCr High-Entropy Alloys. *Metals*, 7(2), pp.57.
- [61] Zhao, Y. L., Yang, T., Zhu, J. H., Chen, D., Yang, Y., Hu, A., Liu, C. T., & Kai, J. J. (2018). Development of high-strength Co-free high-entropy alloys hardened by nanosized precipitates. *Scripta Materialia*, 148, pp.51–55.
- [62] He, J. Y., Wang, H., Huang, H. L., Xu, X. D., Chen, M. W., Wu, Y., Liu, X. J., Nieh, T. G., An, K., & Lu, Z. P. (2016). A precipitation-hardened high-entropy alloy with outstanding tensile properties. *Acta Materialia*, 102, pp.187–196.
- [63] Chang, C. H., Titus, M. S., & Yeh, J. W. (2018). Oxidation Behavior between 700 and 1300 °C of Refractory TiZrNbHfTa High-Entropy Alloys Containing Aluminum. *Advanced Engineering Materials*, 20(6).
- [64] Yurchenko, N., Panina, E., Zhrebtsov, S., Salishchev, G., & Stepanov, N. (2018). Oxidation Behavior of Refractory AlNbTiVZr0.25 High-Entropy Alloy. *Materials*, 11(12).
- [65] Gorr, B., Müller, F., Azim, M., Christ, H.-J., Müller, T., Chen, H., Kauffmann, A., & Heilmaier, M. (2017). High-Temperature Oxidation Behavior of Refractory High-Entropy Alloys: Effect of Alloy Composition. *Oxidation of Metals*, 88(3–4), pp.339–349.

- [66] Dam, T., & Shaba, S. (2016). *Ductilizing Refractory High Entropy Alloys* (Bachelor's thesis. Chalmers University of Technology). Chalmers Publication Library.
<http://publications.lib.chalmers.se/records/fulltext/237688/237688.pdf>
- [67] Kareer, A., Waite, J. C., Li, B., Couet, A., Armstrong, D. E. J., & Wilkinson, A. J. (2019). Short communication: 'Low activation, refractory, high entropy alloys for nuclear applications.' *Journal of Nuclear Materials*, 526.
- [68] Senkov, O. N., Wilks, G. B., Scott, J. M., & Miracle, D. B. (2011). Mechanical properties of Nb₂₅Mo₂₅Ta₂₅W₂₅ and V₂₀Nb₂₀Mo₂₀Ta₂₀W₂₀ refractory high entropy alloys. *Intermetallics*, 19(5), pp.698–706.
- [69] Inconel ® Alloy 718,
https://www.specialmetals.com/assets/smc/documents/inconel_alloy_718.pdf
- [70] Haynes ® 230 ® Alloy, <http://haynesintl.com/docs/default-source/pdfs/new-alloy-brochures/high-temperature-alloys/brochures/230-brochure.pdf>
- [71] Wang, M., Ma, Z., Xu, Z., & Cheng, X. (2019). Microstructures and mechanical properties of HfNbTaTiZrW and HfNbTaTiZrMoW refractory high-entropy alloys. *Journal of Alloys and Compounds*, 803, pp.778–785
- [72] Cao, Y., Liu, Y., Liu, B., Zhang, W., Wang, J., & Du, M. (2019). Effects of Al and Mo on high temperature oxidation behavior of refractory high entropy alloys. *Transactions of Nonferrous Metals Society of China*, 29(7), pp.1476–1483.
- [73] Li, Q., Zhang, H., Li, D., Chen, Z., Huang, S., Lu, Z., & Yan, H. (2019). W_xNbMoTa Refractory High-Entropy Alloys Fabricated by Laser Cladding Deposition. *Materials*, 12(3).
- [74] Vimal, R. K., & Dhanjayan, G. (2018). Improving fatigue life of gas turbine fan blade using advanced composite materials. *IOP Conference Series: Materials Science and Engineering*, 455.
- [75] Guo, S., Hu, Q., Ng, C., & Liu, C. T. (2013). More than entropy in high-entropy alloys: Forming solid solutions or amorphous phase. *Intermetallics*, 41, pp.96–103.

- [76] Kurichenko, V. L., Karpenkov, D. Y., Karpenkov, A. Y., Lyakhova, M. B., & Khovaylo, V. V. (2019). Synthesis of FeNi tetrataenite phase by means of chemical precipitation. *Journal of Magnetism and Magnetic Materials*, 470, pp.33–37.
- [77] Takeuchi, A., & Inoue, A. (2010). Mixing enthalpy of liquid phase calculated by miedema's scheme and approximated with sub-regular solution model for assessing forming ability of amorphous and glassy alloys. *Intermetallics*, 18(9), pp.1779–1789.
- [78] Zhou, N., Jiang, S., Huang, T., Qin, M., Hu, T., & Luo, J. (2019). Single-phase high-entropy intermetallic compounds (HEICs): bridging high-entropy alloys and ceramics. *Science Bulletin*, 64(12), 856–864.
- [79] Ma, S. G., & Zhang, Y. (2012). Effect of Nb addition on the microstructure and properties of AlCoCrFeNi high-entropy alloy. *Materials Science and Engineering: A*, 532, 480–486.
- [80] Cao, Y., Liu, Y., Liu, B., Zhang, W., Wang, J., & Du, M. (2019). Effects of Al and Mo on high temperature oxidation behavior of refractory high entropy alloys. *Transactions of Nonferrous Metals Society of China*, 29(7), 1476–1483.
- [81] AZoM. (2013, June 11). *Aluminium / Aluminum 3105 Alloy (UNS A93015)*. AZoM.Com. <https://www.azom.com/article.aspx?ArticleID=6620>
- [82] Das, A., & Tarafder, S. (2008). Geometry of dimples and its correlation with mechanical properties in austenitic stainless steel. *Scripta Materialia*, 59(9), pp.1014–1017.
- [83] Senkov, O. N., Gorsse, S., & Miracle, D. B. (2019). High temperature strength of refractory complex concentrated alloys. *Acta Materialia*, 175, pp.394–405.
- [84] Li, Y. (2019). *Mechanics of Quantum Mechanical Behaviors and Machine Learning Model for Predicting High-entropy Alloy* (Doctoral dissertation, Nanjing University of Aeronautics and Astronautics, Nanjing, Jiangsu, China).

- [85] Xiang, L., Guo, W., Liu, B., Fu, A., Li, J., Fang, Q., & Liu, Y. (2020). Microstructure and Mechanical Properties of TaNbVTiAl_x Refractory High-Entropy Alloys. *Entropy*, 22(3).
- [86] Senkov, O. N., Miller, J. D., Miracle, D. B., & Woodward, C. (2015). Accelerated exploration of multi-principal element alloys for structural applications. *Calphad*, 50, pp.32–48.
- [87] Ge, S., Fu, H., Zhang, L., Mao, H., Li, H., Wang, A., Li, W., & Zhang, H. (2020). Effects of Al addition on the microstructures and properties of MoNbTaTiV refractory high entropy alloy. *Materials Science and Engineering: A*, 784.
- [88] Senkov, O. N., Senkova, S. V., & Woodward, C. (2014). Effect of aluminum on the microstructure and properties of two refractory high-entropy alloys. *Acta Materialia*, 68, pp.214–228.
- [89] Lin, C. M., Juan, C. C., Chang, C. H., Tsai, C. W., & Yeh, J. W. (2015). Effect of Al addition on mechanical properties and microstructure of refractory Al_xHfNbTaTiZr alloys. *Journal of Alloys and Compounds*, 624, pp.100–107.